# SILK FILM BIOMATERIALS FOR OCULAR SURFACE REPAIR

A Dissertation

Presented to the Faculty of the Graduate School of Cornell University

In Partial Fulfillment of the Requirements for the Degree of

Doctor of Philosophy

by

BRIAN DAVID LAWRENCE

AUGUST 2012

SILK FILM BIOMATERIALS FOR OCULAR SURFACE REPAIR

Brian David Lawrence, Ph.D.

Cornell University 2012

## ABSTRACT

Current biomaterial approaches for repairing the cornea's ocular surface upon injury are partially effective due to inherent material limitations. As a result there is a need to expand the biomaterial options available for use in the eye, which in turn will help to expand new clinical innovations and technology development. The studies illustrated here are a collection of work to further characterize silk film biomaterials for use on the ocular surface. Silk films were produced from regenerated fibroin protein solution derived from the *Bombyx mori* silkworm cocoon. Methods of silk film processing and production were developed to produce consistent biomaterials for *in vitro* and *in vivo* evaluation. A wide range of experiments was undertaken that spanned from *in vitro* silk film material characterization to *in vivo* evaluation. It was found that a variety of silk film properties could be controlled through a water-annealing process. Silk films were then generated that could be use *in vitro* to produce stratified corneal epithelial cell sheets comparable to tissue grown on the clinical standard substrate of amniotic membrane. This understanding was translated to produce a silk film design that enhanced corneal healing *in vivo* on a rabbit injury model. Further work produced silk

films with varying surface topographies that were used as a simplified analog to the corneal basement membrane surface *in vitro*. These studies demonstrated that silk film surface topography is capable of directing corneal epithelial cell attachment, growth, and migration response. Most notably epithelial tissue development was controllably directed by the presence of the silk surface topography through increasing cell sheet migration efficiency at the individual cellular level. Taken together, the presented findings represent a comprehensive characterization of silk film biomaterials for use in ocular surface reconstruction, and indicate their utility as a potential material choice in the development of innovative procedures and technologies for corneal repair.

## BIOGRAPHICAL SKETCH

Brian D. Lawrence was born in Cleveland, OH in 1981. He received a Bachelors of Science in Bioengineering from the University of Toledo (Toledo, OH) in 2004. He then completed a Masters of Science in Biomedical Engineering from Tufts University (Medford, MA) in 2008. He then joined Cornell University's Doctorate of Philosophy program in Biomedical Engineering the same year.

# DEDICATION

I dedicate this dissertation to the memory of my grandparents Fran and Joseph Domitz who taught me the value of hard work, patience, and persistence in attaining a life of dignity, respect, and goodness.

ACKNOWLEDGMENTS

Science is a team effort, and the work presented here is no different. I would like to take the opportunity to thank a number of my colleagues who without their help this dissertation in its entirety would not be possible. First and foremost, I would to thank my advisor Dr. Mark Rosenblatt for his constant guidance, enthusiasm, and progressive vision for this work. Dr. Rosenblatt provided an environment where my scientific passions could thrive, and offered much conceptual assistance in formulating much of the work. He has proven time and time again to be an excellent mentor, and he will continue to be a colleague and dear friend of mine throughout my life.

I would like to thank Dr. Zhi Pan, while during her post-doctorate training in the lab she was instrumental in developing a number of the assays and techniques used to complete the work described. Specifically, she was instrumental in the development of the silk film culture system (Chapter 3), and produced the majority of the raw data from the HCLE cell sheet migration studies (Chapter 7). In addition, she taught me how to do western blotting and was responsible for selecting the majority of anti-bodies used in this work. She is a highly resourceful and intelligent biomaterial scientist who's endless support I will always be indebted to.

I would also like to thank Dr. Jingbo Liu who has played a critical role in assisting with the amniotic membrane and *in vivo* rabbit studies. Dr. Liu performed a majority of the *in vitro* cell sheet culture and biochemical work on

the silk film and amniotic membrane substrates (Chapter 4). In addition, he performed rabbit surgeries, surgical follow-ups, and provided much input on the development of the silk films used *in vivo* (Chapter 5). He is truly a great scientist, an incredibly skilled surgeon, and a great friend.

Also, I would like to thank the members of the Margaret M. Dyson Vision Research Institute at the Weill Cornell Medical College for their constant support and guidance. Specifically, thanks to Aihong (Ellen) Liu for preparing and maintain the laboratory's cell culture capabilities, and for ordering and managing many of the lab supplies I used. Thanks to Mike Weber for his pivotal role in the design and implementation of the silk film culture system, and for his efforts in developing various protein assays in the lab. Thank you to Jessica Schmidt who performed significant data analysis for the *in vivo* rabbit studies, and also provided much support in silk production. Thanks especially to Dr. Ryan Schreiner, Gwen Szabo, Dr. Rachel Sartaj, Dr. John Pena, and Dr. Victor Guaiquil for their scientific guidance and technical expertise on a number of conceptual issues.

I want to thank my committee members, Dr. Robin Davisson, Dr. David Putnam, and Dr. Peter Doerschuck, for their continued support and guidance throughout the course of my PhD. I would also like to thank my previous mentor Dr. David Kaplan from Tufts University for introducing me to the wonders of silk. I want to specifically thank him for his editorial help on Chapters 2, 3, and 6, and for always being an extremely supportive colleague

and friend. Thanks to Belinda Floyd, Dr. Cynthia Reinhart-King, Dr. Rob Illic, and Gary Bordonaro from Cornell University's Ithaca campus for their technical input and support. Thanks to Dr. Jonathan Kluge, Dr. Charles Kim, Thomas Steffie, Ben Rollins, Dr. Denise Barbut, and Dr. Brian Levy for their helpful suggestions and inputs towards the work. I would like to thank the funding sources for this work, specifically the National Institutes of Health (K08EY015829, R21EY019561, and R24EY015656 awards), the Research to Prevent Blindness Foundation, the Tri-Institutional Stem Cell Initiative, and the Tissue Engineering Resource Center at Tufts University (NIH P41).

I would like to thank all of my friends and family who have supported me through the multitude of trials and tribulations of the PhD process, and for your endless belief in me to be a success. I want to especially thank my parents, Brian and Susan Lawrence, for making it possible for me to pursue my educational goals and who have always supported me in everything I do. I would also like to thank my sisters, Kimberly, Samantha, and Meghan, for always being there for me. Finally, I want to especially thank the love of my life, Elise Li, whose abundant help and support has meant the world to me.

Thank you all!

TABLE OF CONTENTS

LIST OF FIGURES

**Chapter 1:**



**Chapter 2:**



**Chapter 3:**

**Chapter 4:**



**Chapter 5:**

**Chapter 6:**

**Chapter 7:**

LIST OF TABLES

# LIST OF ABBREVIATIONS AND SYMBOLS

AM – amniotic membrane

AEC – anti-E-cadherin

BPE – bovine pituitary extract

BSA – bovine serum albumin

C – linear curve length distance

CMLE - Classic Maximum Likelihood Estimation

$dH_2O$ – deionized water

Dk – Oxygen permeability

DMEM – Dulbecco's modified eagles medium

ECM – extracellular matrix

EDTA – ethylenediaminetetraacetic

EGF – Epidermal growth factor

FA – Focal adhesion

FBS – Fetal bovine serum

FTIR – Fourier infrared spectroscopy

H&E - Hemotoxylin and eosin

HCEC – human corneal epithelial cell

HCLE – Human corneal limbal-epithelialium

HMDS – hexamethyldisiloxane

IR – infrared

K-SFM – Keratinocyte-serum free medium

L – total curve length

MeOH - methanol

MIP – maximum intensity projection

MMC – Mitomycin-C

MTT – 3-(4,5 – Dimethiazol-2-yl)-2,5-diphenyltetrazolium bromide

MWCO – molecular weight cut off

$O_2GTR$ – oxygen transmissibility

OCT – Optical coherence tomography

PBS – Phosphate buffered saline

PDMS - polydimethylsiloxane

PGLA – poly glycolic acid

PSF – penicillin-streptomycin-fungizone

PSI – pounds per square inch

PVDF – polyvinylidene

RCEC – rabbit corneal epithelial cell

RCF – relative centrifugal force

RH – Relative humidity

RMS – root mean square

SD – standard deviation

SEM – scanning electron microscopy

SF – silk fibroin MMC – Mitomycin-C

TCP – tissue culture plastic

WA – water-annealed

wt./vol.%- weight to volume percent

$\eta$ – cell sheet migration efficiency

$\tau$ – tortuosity value

$\parallel$ - parallel direction

$\perp$ - perpendicular

CHAPTER 1

# Introduction

## 1. Silk as a Biomaterial

Silk is a 380M-year old material that has evolved as the insect's catchall for external structure (1). Similar to how humans use concrete, metals, and plastics to build the world around us, arthropods have employed nearly 40,000 different silk proteins to produce varying structures such as webbing, nests, cocoons, and underwater air sacks (2). Historically, humans have harnessed the fibers produced by the domesticated *Bombyx mori* silkworm for their own uses in textile applications due to the material's extraordinary mechanical and visually appeasing properties (3).

It has been shown that *Bombyx mori* silk worm cocoon structural protein, called fibroin, can be solubilized into an aqueous solution and reformed into a number of different geometrical forms such as films, tubes, sponges, hydrogels, electrospun fibers, microspheres, and solid blocks [Figure 1] (4). Over the last two decades numerous investigators have been devoted to further understanding the potential of regenerated silk fibroin solution for use in tissue engineering and regenerative medicine applications, which is primarily due to the material's high level of biocompatibility and controllable material properties (5-8).

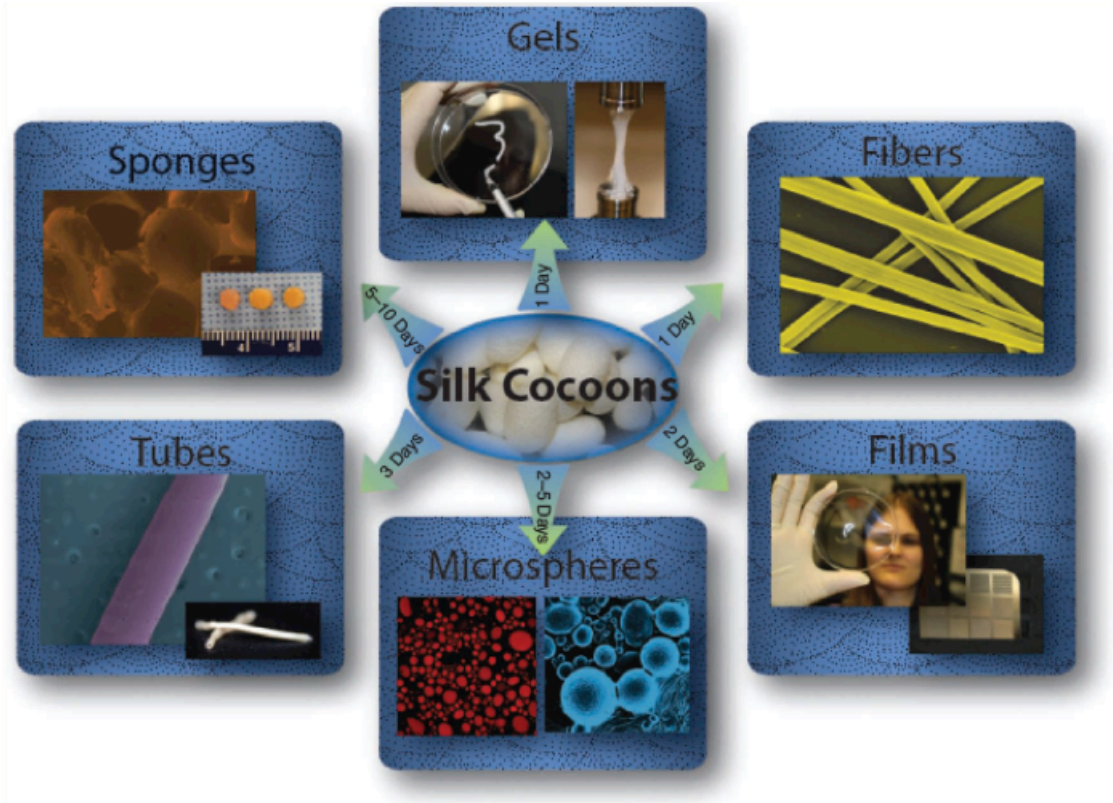


**Figure 1.** *Bombyx mori* silkworm cocoons can be solubilized into aqueous solution an regenerated into number of structural forms such as gels, fibers, films, microspheres, tubes and sponges (4).

Recent work has shown that constructs formed from silk solution are biocompatible in vivo, and have proven to be both non-inflammatory and non-immunogenic upon implantation (9-14). Current animal models are underway to assess the use of silk solution in the creation of scaffolds for bone, ligament, and nervous tissue (14-16). In addition, a number of scaffolds are being developed as in vitro tissue analogs for corneal, intervertebral disk, cardiac, breast, skin, and articular cartilage (13,17-22). As with traditional tissue engineering approaches, the silk scaffolds are typically seeded in vitro with a

specific cell type, and culture growth and tissue production occurs over time (23). It has been shown that the silk fibroin protein can be degraded through a number of naturally occurring proteolytic enzymes (24-27). The hydrolyzed silk protein is believed to be cleared from the tissue through cellular phagocytic pathways (28). Silk fibroin protein is primarily composed of glycine and alanine amino acids that can be reused for new protein synthesis post degradation. As a result, silk degradation products do not collect in the local environment to cause an induced inflammatory response, which is commonly associated with other synthetic biomaterials like poly (lactic-co-glycolic acid) (PLGA) derivatives (29). The silk fibroin's degradation rate and byproduct formation is directly related to the protein's secondary structure content (30-33). By increasing or decreasing the presence of these structures, the silk degradation rate can be adjusted from minutes to years (34,35).

## 2. Modulation of Silk Biomaterial Properties

The ability to control silk material properties offers a number of advantages over other polymer systems. The formation of silk structures begins with fibroin proteins aggregating into protein globules in solution [Figure 2A-C] (36-38). The fibroin globules then aggregate to form larger bulk macrostructures that can be modified through a variety of energy inputs [Figure 2D] (37). The silk structure material properties can then controlled through inducing protein secondary structures formations such as α-helices, β-sheets, and β-turns

through a variety of post-processing techniques (30-33).

The formation and organization of these structures modulates total hydrogen and hydrostatic bonding within the material's bulk structure, which affect the macro material properties. A variety of silk processing methods have been developed to produce the multitude of structures previously mentioned, and range from the use of physical factors such mechanical stress and heat to the use of chemicals from water to organic solvents in order to induce secondary structure formation and control (14,39-42). As a result, silk protein properties such as degradation rate, hydrophobicity/hydrophilicity, transparency, mechanical strength, porosity, oxygen permeability, and thermal stability can be altered (23,42-46). In this regard, silk proteins can be considered an engineering class of biopolymers in which the material properties can be defined for a given application.

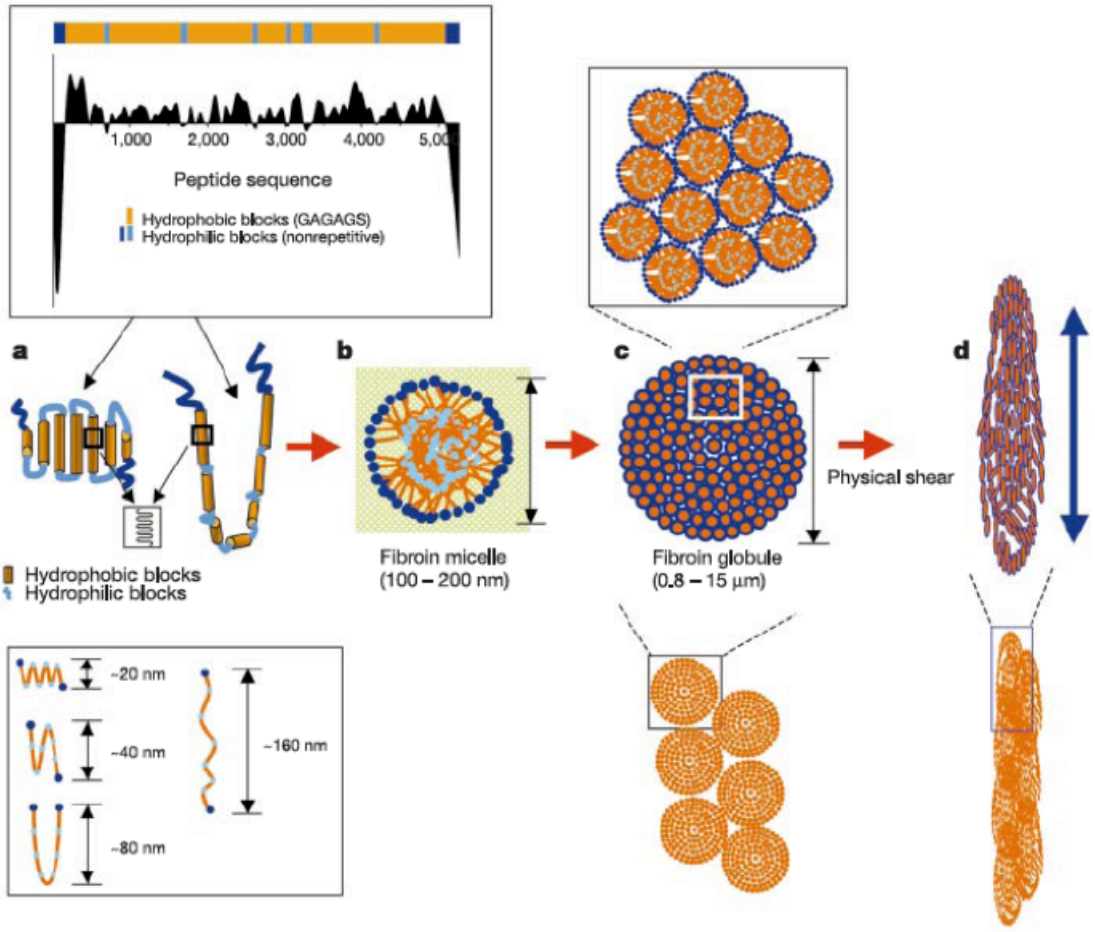


**Figure 2.** Model of silk fibroin chain folding, micelle formation, globule formation, and shear processing of silk proteins. (A) Hydrophobicity pattern of silk fibroin primary sequence with possible chain folding intra- and inter-molecular schemes. (B) Micelle assembly of silk fibroin in water, based on hydrophilic–hydrophobic co-polymer structure leaving internal smaller hydrophilic domains to promote solubility in water, with larger-chain terminal hydrophilic blocks in contact with the surrounding aqueous solution. (C) 'Globule' formation driven by increased fibroin concentration and lower water content, further hydrophobic interactions, and at the final stages by the presence of sericin. (D) Elongation and alignment of globules and interactions among globules promoted by energy input. One example is physical shear which leads to fibril structure formation for example (37).

## 3. Silk Film Biomaterials

The use of silk films have recently been under active investigation for use in a wide variety of biomedical applications due to their inherent biomaterial properties and straightforward processing regimes (21,25,47,48). Control of silk film protein secondary structure formation is accomplished partly through the control of water content within the material (49-52). Water acts as a plasticizer allowing for silk protein chain movement within the film bulk structure (51). The rate and extent of chain movement can be readily controlled through a water-annealing (WA) process in which the dried silk films are exposed to a given concentration of water vapor at a specified temperature and period of time (32,40). As a result this processing allows for the highly controlled induction of the random coiled silk protein secondary structure into α-helices, β-sheets, and β-turns (32).

The induction of silk film protein β-sheet secondary structure is directly proportional to a decrease in degradation rate and improved mechanical properties (38,53). Additionally, when WA at room temperature the random coil content is highly conserved and produces water insoluble films that are transparent to visible light (40). Their transparent, biocompatible, and controllable material properties have recently been under investigation for use in ocular surface reconstruction for repairing the inured cornea (22,54). In the current dissertation material processing is utilized to produce insoluble and soluble silk films that are utilized for in vitro and in vivo studies respectively.

## 4. The Cornea and Ocular Surface Reconstruction

The cornea is the transparent window to the eye that enables light to focus on the retina [Figure 3A], and is composed of three tissue layers: the epithelium, stroma, and endothelium (55,56). The tissue's architecture consists of a highly organized layering of stacked lamellae layers primarily composed of cells and extracellular matrix (ECM), in which the three tissue layers are separated by two basement membrane structures separating the epithelium and endothelium from the stromal tissue [Figure 3B] (55,57).

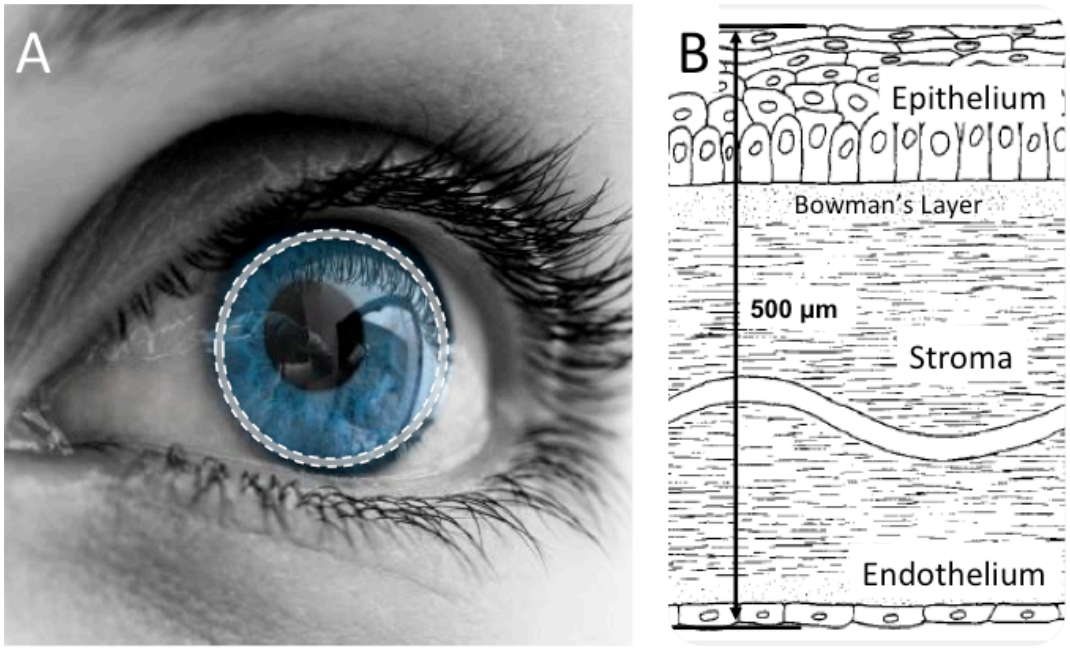


**Figure 3.** (A) The transparent human corneal tissue indicated to be within the circled region of the eye. (B) Schematic representation of a cornea cross-section where the cornea is composed of an epithelium, stroma, and endothelial tissue layer. The tissue layering is a lamellar layering of tissue structures (stroma not to scale), interspersed by two basement membranes separating the anterior epithelium and posterior endothelium from the stroma (55).

Trauma or disease affecting the front of the eye injures the corneal epithelium, and if severe enough can cause blindness due to tissue scarring (58,59). In the United States ocular surface trauma and disease accounts for over 2.5-million cases annually, with over 50-million cases occurring worldwide (58,60). Current treatments for corneal damage to the front of the eye is termed ocular surface reconstruction, and may involve any number of procedures focused on restoring tissue transparency and vision (60). Corneal scarring is largely caused by the loss of progenitor limbal stem cells located in the peripheral region of the corneal tissue (61). When limbal stem cells are lost due to injury or disease the corneal epithelium has difficulty recovering the damaged surface, and as a result the more epidermal and non-transparent sclera or conjunctiva tissue will migrate over the cornea to heal the site of affliction (62,63). This results in loss of corneal transparency and a proportional loss of vision.

A variety of approaches have been utilized to address ocular surface repair (64-66). This began with the use of biocompatible synthetic polymers and hydrogel contact lenses in the 1940's to cover corneal injury sites (67). Although contact lens technology has improved over the decades, these devices only provide a protective covering and are not considered regenerative or integrate with the corneal tissue (68). For this reason these devices will not be considered as comparable devices to silk and will not be detailed here.

A more regenerative approach has been the use of amniotic membrane in ocular surface reconstruction, and is regularly utilized in the clinical setting (69,70). Amnion membrane is a donated tissue derived from the placenta of a birthing woman. The amnion material is a fibrous elastic material that is thought to contain many ECM and anti-inflammatory factors, which are thought to help enhance healing after being applied over a damaged corneal surface (71). However, there is still debate over the mechanism of how amnion may promote healing, and it is not effective for all ocular surface reconstruction procedures (72).

Of particular interest is in amnion's use as a stem cell carrier for transporting limbal stem cells to ocular surfaces that have reduced healing do to loss of native cell populations (73,74). It has been found that explanted autologous limbal stem cell populations may be cultured to confluency upon amniotic membrane and then transplanted to an injured eye leading to improved healing and vision for the patient (73,75). However, clinical results can be highly variable, and there are additional logistical issues with using amnion due to tissue inaccessibility, need for refrigerated storage, and cost which relegate its use to the most severe ocular surface reconstruction procedures (69,70,74). In addition to amnion, fibrin carriers have also been developed to transport cultivated limbal stem cell populations onto the damaged corneal surface (65). Studies have to date been limited to in vivo rabbit models which success, and significant clinical use has yet to be

reported (76,77). However, there are numerable hurdles to overcome with fibrin carriers due to their potential for disease transmission, opaque nature, material consistency issues, and the need to develop consistent methods of processing (60). As a result there is a need to develop improved biomaterial options for use in ocular surface repair.

The inherent transparency, biocompatibility, and tunable material properties possessed by silk film biomaterials are currently being leveraged for use in repairing the ocular surface (22,54). Recent findings have shown that silk film surfaces allow for the successful attachment and culture of both stromal and epithelia corneal cell types (21,22). Silk films have been successfully produced to recapitulate the formation of the lamellae corneal stroma architecture through stacking porous 2-μm films into three-dimensional in vitro tissue constructs (21). Subsequent research has shown that stratified epithelial layers could be formed on silk film surfaces comparable to that of amniotic membrane, and thus demonstrated potential a potential material for use in ocular surface reconstruction (22). However, silk films have the added benefits of reducing the potential of disease transmission from a donor, high level of material accessibility, reduced cost, and room temperature storage. The work investigated in this dissertation builds off this knowledge to utilize the tunable properties of silk films to construct materials capable for use in ocular surface reconstruction procedures.

## 5. Corneal Basement Membrane Surface Topography

Surface topography has been found to play a critical role in regulating many cell functions such as adhesion strength, migration, proliferation, differentiation, and apoptosis (78-82). The influence that a given surface topography has on cell attachment, alignment, and migration is termed contact guidance (83). It has been shown that topographic features can direct these functions through contact guidance by enhancing surface interactions with cellular binding proteins such as integrins and focal adhesion complexes (78,81,84-86). Surface topography plays a crucial physiological role in tissue basement membranes where nano- and micro-features aid in regulating cell attachment and migration, which has important roles in response to injury, differentiation, and cancer formation (24,87-89).

The cornea's Bowman's Layer rests between the epithelium and stroma tissues, and has been shown to be composed of nano- to micro-topographic features (87). The presence of basement membrane surface topography is implicated in a number of important cellular functions for maintaining vision including enhancement of cell attachment, migration, and proliferation (80,87,90,91). In addition, surface topography has been shown to direct cell migration and new basement membrane protein production of ECM (92-94). As a result, studies are underway to characterize how the use of topography may be used to enhanced corneal healing or produce improved tissue engineered corneal constructs (79,80,90,93,95-97).

The production of silk films with defined surface topography are currently under investigation for their use in studying cell-to-surface interactions(21,39,98,99). Recent findings have shown that silk film surface topography can be highly controlled at the nanoscale and customized to produce a variety of geometries and architectures [Figure 4] (25,100,101). Patterned silk films are currently being studied for their use in developing biocompatible optical devices, electronics, and as previously mentioned for substrates to guide tissue growth (21,25,35,47,98,102). It has been demonstrated that traditional photolithography and soft-lithography methods utilized in the electronic fabrication industry can be translated for producing silk topographies as well (25,103,104). Patterned silk film surfaces are produced on silicon wafer surfaces, which are then used to form silicone rubber negative imprinted casting molds [Figure 4A]. The regenerated silk solution is then cast upon poly dimethylsiloxane (PDMS, i.e. silicone rubber) molds to produce silk films with defined surface topography matching the original silicon wafer dimensions [Figure 4B-C] (4,25,48). Silk fibroin is capable of patterning surface features on the nanometer scale at a high level of fidelity for replicating a desired surface feature [Figure 4E-F]. Silk films with patterned surface topography have been shown to align corneal stromal cells in vitro [Figure 4D, G] (21). This knowledge is employed in this dissertation to produce silk films that guide corneal epithelial cell attachment and migration.

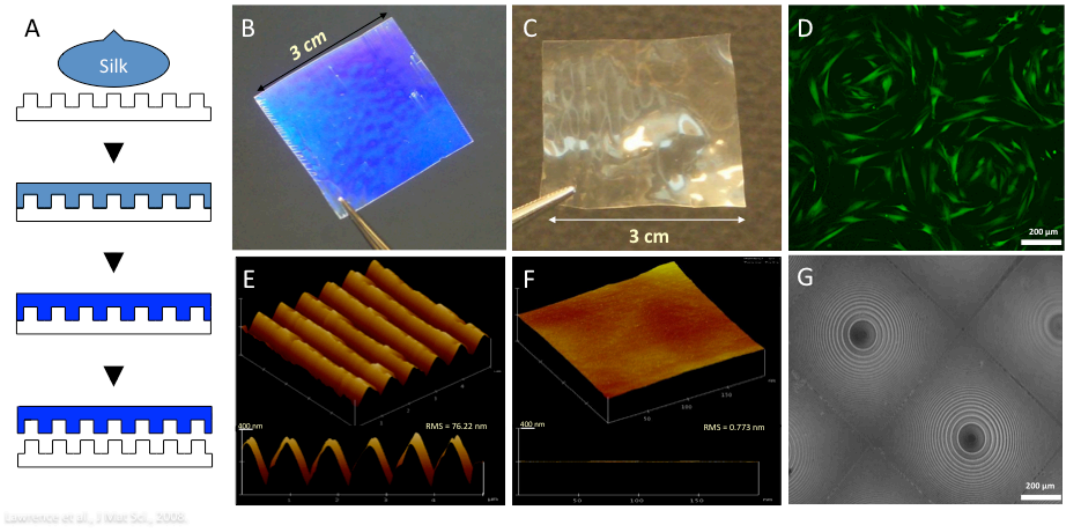


**Figure 4.** (A) Nano- and micro-patterned silk films surfaces are produced by casting silk solution onto a molding surface (i.e. PDMS), and then the silk film is removed from the casting surface after drying and processing. Silk films can be produced with (B) surface topography or (C) flat surfaces, as respectively (E-F) visualized through atomic force microscopy imaging respectively (26). (D) In vitro, circular corneal stromal cell alignment was induced by utilizing (G) patterned silk films surfaces with concentric ring topographies (21).

CHAPTER 2

# Effect of Hydration on Silk Film Material Properties

## 1. Summary

Effects of hydration on silk fibroin film material properties were investigated for water-annealed and methanol (MeOH) treated samples. After hydration, thickness increased 60% for MeOH immersed films, while water-annealed samples remained constant. TGA determined MeOH immersed films had an 80% mass loss due to water, while water-annealed had a 40% mass loss. $O_2$ permeability was greater in MeOH immersed films with Dk values of 10 ($10^{-11}$·m$LO_2$·cm) /(cm·s·mmHg), while water-annealed films had Dk values of 2 ($10^{-11}$·m$LO_2$·cm) /(cm·s·mmHg). All films showed a decrease in Young's modulus and increased plastic deformation by two orders of magnitude when submerged in saline solution. FTIR revealed water-annealed films increased in β-sheet content with increasing water vapor, while MeOH immersed films did not change.

## 2. Introduction

Webs and cocoons are examples of structures formed from silk proteins, a versatile family of fibrous proteins (1). Silk fibers have been used by humans for the production of textiles for thousands of years. More recently, silk proteins have been found to offer a versatile range of biomaterial properties

that make it desirable for applications in regenerative medicine and tissue engineering (6). The silk protein fibroin, the primary structural component in *Bombyx mori* cocoons, generates a minimal immune and inflammatory response when implanted within the body, and is degraded by naturally occurring proteolytic enzymes (7,9,34,105). The rate of degradation is directly related to the content of secondary β-sheet crystalline structure present within the bulk material (34,44,106). The amount of β-sheet can be modified in silk-based biomaterial structures produced from regenerated silk fibroin through the use of various processing methods (7,34,40,44,106). Recent efforts have resulted in the formation of films, sponges and hydrogels from regenerated silkworm fibroin (1,7). Further efforts are underway to expand the use of fibroin based devices as drug delivery vehicles (6,107), optical sensors (7,9,25,34,47,105), and microfluidic chambers (34,44,106,108,109).

With the increasing use of silk fibroin across fields it is important to understand how water affects the bulk material properties of this structural protein. Silk fibroin posses both hydrophobic and hydrophilic regions with a block copolymer design (7,34,37,40,44,106). Although the majority of the molecular structure is composed of hydrophobic amino acid regions, the presence of hydrophilic chain ends, as well as intervening hydrophilic regions, allows water to interact with the fibroin protein structure. As a result, water molecules produces a plasticizing affect to alter molecular interactions, potentially impacting the mechanical properties of these materials (43,49),

depending on the thickness, crystallinity and processing history. Only a few studies have focused on how hydration impacts silk material properties since the native fibers are inherently very stable to hydration (42,49). Therefore, the current study focused on elucidating the effects of water on bulk material properties of silk fibroin films that were processed using two previously described treatments, methanol (MeOH) solvent immersion (110) and water-annealing (40). This post-casting of silk solution for film formation processing is required to generate water insoluble films that remain stable when submerged in water, and offering control of secondary structure content.

Previous work has shown that silk films treated with MeOH exhibit almost a 3-fold increase in β-sheet content when compared to water-annealed silk films (26). Therefore, it is important to understand how silk film material properties change with respect to this change in β-sheet content. For example, this type of information is important for the design of a silk-based devices destined for *in vivo* applications. By better understanding how water influences the properties of silk materials, processing methods can be tailored for selective functions. Furthermore, the organization of protein secondary structure is important for understanding how the presence of solvents, such as water or MeOH, affect film material properties. Therefore, it is important to understand how the content and organization of fibroin secondary structure contributes to changes in material properties (3).

Recent studies have focused on the use of water-annealed silk films for

optical devices due to their transparent nature and surface patterning capabilities (25,26,47). These attributes contribute to the versatility of silk biomaterials, as the combination of optical transparency, biodegradability, and superior mechanical strength lend these water-annealed silk films as a suitable material for vision-related medical devices (21). Specifically, corneal tissue engineering and regeneration provide suitable targets for these silk biomaterials (54). However, it is important to better understand how the physical properties of these types of silk films are altered within hydrated environments. Therefore, the present study was focused on the characterization of both water-annealed and MeOH submersion treatments in terms of their impact on silk film material swelling, mechanical properties, thermal stability, and oxygen permeability.

## 3. Materials and Methods

### 3.1. Preparation of Silk Fibroin Solution

As described previously (25,45) and illustrated in Figure 1, *B. mori* silk cocoons (Institute of Sericulture, Tsukuba, Japan) were cut into fourths and boiled for 45 minutes in 0.02M $Na_2CO_3$ (Sigma-Aldrich) to extract the glue-like sericin proteins from the structural fibroin proteins. The fibroin extract was then rinsed three times in Milli-Q water, dissolved in 9.3M LiBr solution at room-temperature, and set covered within a 60°C oven for 4 hours. The solution was then dialyzed (MWCO 3,500) in water for 48 hours with 6 water changes at 1,

4, 8, 12, 12 and 12 hour intervals. The dialyzed silk solution was then centrifuged at 13,000 g, and the supernatant was collected and stored at 4°C. The final concentration of aqueous silk solution was 8 wt/vol.% as determined by gravimetric analysis.

### 3.2. Preparation of PDMS Casting Substrates

Flat PDMS substrates of 0.75 mm in thickness, were prepared by casting 38 mL of a 9:1 mixture of silicone potting solution to catalyst (GE Plastics, Inc.) upon 500 $cm^2$ square petri dishes (Corning Inc., Corning, NY). The solution was then degassed for 2 hours and cured at 60˚C for 12 hours. Post curing PDMS circular shapes were punched out with 11 and 30 mm diameter geometries. In addition, PDMS dog-bone geometries were also punched out using the ASTM-D-638-4 standard size sharp edge cutting die, which includes a 3.18 x 9.53 mm neck region for testing. The PDMS substrates were then prepared for silk film casting by washing once with 70% ethanol solution and rinsing three times with $dH_sO$. PDMS surfaces were used for multiple silk film castings. Between film casting silk residuals were removed using a 9.3M LiBr soaking prior to the washing and rinsing protocol.

### 3.3. Preparation of Silk Films

Three different silk film sample sizes were produced from casting 70 and 400 $\mu$L of 8% silk solution onto 11 and 30 mm diameter PDMS rounds,

respectively, and casting 400 $\mu$L of 8% silk solution onto dog-bone shaped substrates. The volumes for the PDMS round geometries and dog-bone shapes were chosen to optimize the overall casting time and thickness uniformity based on prior casting studies (25,26). The films were then covered with a lid that allowed for atmospheric venting. The films were then left to dry overnight at ambient conditions. Once dried, water-annealing processing was performed on one set of silk film samples by placing the dishes on a shelf in a valved container partially filled with water. Next, a 24 mmHg vacuum was pulled within the container, and once vacuum was reached the valve was placed in the closed position. This produces a saturated water vapor environment that induces β-sheet secondary structure formation within the silk film (40). The films were left within the water vapor environment for a five-hour period and then placed into a dH2O bath to await experimentation. Separate sets of silk films were processed using the MeOH solvent immersion, in which the silk films were submerged in 50:50 MeOH to water solution for a minimum of 20 minutes to induce β-sheet formation (111). Following treatment, the silk film samples were then placed into a dH2O bath to await experimentation. All samples were used for experimentation within a 24-hour period after both casting and processing.

### 3.4. Measurement of Silk Film Thickness

Hydrated and dehydrated dog-bone shaped silk film thicknesses were

assessed using 2-photon confocal microscopy. Hydrated samples were incubated for 24 hours within $dH_2O$ at ambient conditions prior to imaging. TPEF/SHG micrographs were acquired for both hydrated and dehydrated silk film samples using a previously described protocol on a Leica DMIRE2 microscope with a TCS SP2 scanner (Wetzlar, Germany) (112). Images were acquired using a 10x (NA 0.3) dry objective. The excitation light source was a Mai Tai tunable (710-920 nm) titanium sapphire laser emitting 100 fs pulses at 80 MHz (Spectra Physics, Mountain View CA). Samples were placed on glass cover slips (Fischer Scientific, Inc.) and excited at 800 nm. Film thickness was assessed at the center position of the sample neck region. Fluorescence emission spectra were detected from 380 to 700 nm in 100 steps with a 20-nm detector bandwidth. TPEF/SHG images were acquired in the forward direction through a bandpass filter centered at 400 nm (Chroma hq400/20m-2p). Analysis was performed with the Leica Confocal (Wetzlar, Germany) and ImageJ software (NIH, Bethesda, MD).

Sample cross-sectional thickness images were obtained using the "Section" function within the Leica Confocal Software. These images were then exported to ImageJ for analysis. Film thickness (δ) was assessed by measuring the z-y or z-x planes of each image that was generated from the collected TPEF/SHG signal z-stack profile. Film thickness was measured by assessing the cross-sectional region of each z-stack image using the "Plot Profile" function within the Image-J software package. The "Plot Profile"

function outputs the average signal intensity for each pixel line versus the distance along the selected region of the image. Therefore, silk film thickness can be determined by the position of TPEF/SHG signal intensity distribution at a given threshold level, which can be validated against other imaging modalities, such as scanning electron microscopy (SEM), as described below. The calculated threshold for signal intensity that indicates silk film presence was validated by comparing against a previously described SEM imaging methodology for assessing the sample cross-sectional area (25,26). Dog-bone film samples from each processing condition were randomly selected from each sample population and prepared for SEM imaging. Samples were prepared for SEM by flash freezing in liquid nitrogen and cracking the film with a razor blade at the center of the dog-bone neck region. The samples were then adhered to aluminum platforms using conductive tape (Electron Microscopy Sciences, Hatfield, PA), and then sputter coated with 40 nm of gold using a Polaron SC502 Sputter Coater (Fisons,VG Microtech, East Sussex, England). Silk film cross-sectional thickness of each image was analyzed using ImageJ software (NIH, Bethesda, MD). Film thickness measured by SEM was then compared to the collected TPEF/SHG signal distribution. Silk film sample thickness was found to be most similar between both imaging modalities above 80% of the maximum TPEF/SHG signal intensity for each compiled sample z-stack. Silk film thickness swelling ratios (Q) were then calculated using the expression:

$$Q = \frac{\delta_H}{\delta_D} \qquad (1)$$

where Q is the silk film thickness swelling ratio, $\delta_H$ is the hydrated film thickness, and $\delta_D$ is the dehydrated film thickness. Sample thickness measurements and Q values were statistically assessed with the Student t-test for means in both the validation study and comparing differences between hydrated and dehydrated film thicknesses.

### 3.5. Uniaxial Tensile Testing of Hydrated Silk Films

Tensile tests were performed on an Instron 3366 testing frame equipped with a 100N capacity load cell and Biopuls™ pneumatic clamps. Dog-bone shaped silk film samples were hydrated in 0.1M phosphate buffered saline (PBS) for 30 minutes to equilibrate prior to testing. Test samples were submerged into the Biopuls™ temperature-controlled testing container filled with PBS solution (37±0.3°C) for 5 minutes prior to and for the duration of testing. A displacement control mode was used, with a crosshead displacement rate of 10 mm·min$^{-1}$. The measured width of the gauge region of the PDMS slat was multiplied by the specimen thickness (measured by two-photon confocal microscopy) in order to convert load data to tensile stress values. The corresponding strain was measured using an Instron Video Extensometer that tracked the position of 2 painted dots placed 1 cm apart. The initial “linear elastic modulus”, yield stress, elongation to failure, and ultimate tensile strength were calculated from stress/strain plots. The initial “linear elastic

modulus" was calculated by using a least-squares' (LS) fitting between 0.05N load and 5% strain past this initial load point. The yield strength was determined by offsetting the LS line by 2% strain and finding the data intercept. Ultimate tensile strength (UTS) was determined as the highest stress value attained during the test. The elongation to failure was determined as the last data point before a >10% decrease in load (failure strain minus the strain corresponding to 0.05 N load noted earlier). Sample sets were statistically analyzed by using a Student t-test analysis of means.

### 3.6. Thermal Gravimetric Analysis of Silk Film Water Content

The water content in both hydrated and dehydrated silk films were estimated using thermal gravimetric analysis (TGA). TGA has been used to characterize water content within silk fibroin films (42,43). TGA measurements were performed using a TA 500Q system (TA Instruments, New Castle, DE). Prior to loading, 11-mm round silk film samples were either hydrated in dH2O for 24-hours at ambient conditions, or stored in the open ambient environment for 24-hours. Hydrated samples were wiped along the sides of their plastic storage vessels to remove non-absorbed surface water, and immediately loaded into the enclosed TGA oven. All samples were heated to 600˚C at 10˚C/min under an inert nitrogen atmosphere with a flow rate of 40 mL/min. Water mass loss was assessed by observing the percent of initial weight located at the plateau region of the TGA profiles. Thermal stability of the silk

film samples was assessed through 1st derivative peak location from the collected TGA mass loss profiles for both hydrated and dehydrated samples of each processing condition. Such analysis provides insight into the affects of water absorption on the thermal stability of silk films, and may provide insight into how the presence of secondary structures, such as β-sheet content, affect water absorption. Specifically, the position of the 1st derivative(s) of a TGA profile assesses the change in mass loss during the heating cycle due to material phase changes at a specific temperature, such as water evaporation and material degradation thresholds. Thus, changes in β-sheet content may affect the temperatures at which these phase transitions take place (31). Data were normalized to initial mass values for each sample. Statistical analysis between groups was assessed using Student t-tests.

### 3.7. $O_2$ Permeability

Oxygen permeation studies were conducted using the Illinois 8001 Oxygen Permeation Analyzer (Illinois Instruments, Johnsburg, Illinois; ASTM 3985-05). In the first study, circular 11 mm diameter silk films were saturated with $dH_2O$ and evaluated at 37°C and 80% relative humidity (RH) over 15 minute test intervals for a total of 135 minutes. Dry samples were then tested at 37°C and 50% RH using the same time intervals. Oxygen gas transmissibility rates ($O_2$GTR) were recorded. Sample thickness measurements were recorded for each silk film employing the Ono Sokki EG-225F Digital Indicator (AA821

Radius Point; 25g force). Oxygen permeability ($PO_2$) rates were calculated for each silk model in accordance with ASTM 3985-05 as follows:

$$PO_2 = \frac{O^2GTR}{p} \qquad (2)$$

where $O^2GTR$ is the oxygen transmissibility rate ($mLO_2/(cm^2 \cdot day)$), and *p* is the partial pressure of oxygen and is the mol fraction of oxygen multiplied by 1 atm of pressure. These conditions where assumed to be taken as 1 $cm^3$(STP) is 44.62 µmol, 1 atm is 759.81 mmHg, and one day is $86.4 \cdot 10^6$ s.

The acquired $O_2GTR$ values were then converted to thickness dependent oxygen permeability coefficients (Dk) to provide normalized measurements to enable comparison of oxygen permeability across different treatment conditions. The unit of permeance is then given as $mLO_2$ $/(cm^2 \cdot s \cdot mmHg)$. Oxygen permeability coefficients (Dk) for each sample were calculated by:

$$Dk = PO_2 \cdot t \qquad (3)$$

where t is thickness of the homogenous silk material in cm. The unit of Dk is taken to be $(mLO_2 \cdot cm)/(cm \cdot s \cdot mmHg)$.

### 3.8. FTIR Spectroscopy

Silk film secondary structural analysis was measured using an FTIR spectrometer (Vertex80V, Bruker Optics, Inc., Germany). Spectral scans were obtained using dried samples from each processing condition. For each sample a measurement of 66 scans was collected at a resolution of 4 $cm^{-1}$,

which was acquired over a wavenumber range of 400–4000 $cm^{-1}$. Spectral manipulations were performed with OPUS (version 6.0 software, Bruker Optics, Inc.). Quantification of silk secondary structure was based on analyzing the amide I region (1600-1700 $cm^{-1}$) (113). Background absorption due to water was subtracted from the sample spectra to obtain a flat recording in the range of 1750-2000 $cm^{-1}$ (114). The amide I region (1580-1710 $cm^{-1}$) was selected from the entire spectrum, and a linear baseline was applied to the spectrum.

## 4. Results and Discussion

### 4.1. Silk Film Thickness Analysis

When MeOH processed or water-annealed silk films are incubated within a water bath for an extended period of time (> 2 hrs) the films are notably larger in size, which is most likely due to water absorption creating changes in the protein secondary structure. The larger macroscopic geometrical changes in width and height are straightforward to measure with a caliper device; however the micron sized thickness measurements prove more difficult to quantify. Previous studies have evaluated silk film cross-sectional thickness using scanning electron microscopy (SEM) (25,40). However, under SEM imaging conditions samples are dry and under high vacuum. Therefore, a representative cross-sectional thickness cannot be achieved for a silk film in the hydrated state, which would be more applicable to physiological

conditions. 2-Photon Excited Fluorescence and Second Harmonic Generation (TPEF/SHG) has been used to monitor silk film material features under hydrated conditions (112,115). In addition, because this imaging method is non-invasive it allows for the same samples to be used for subsequent testing, unlike the case with SEM. Therefore, TPEF/SHG confocal imaging was used to measure the thickness of the dog-bone silk film samples. Z-stack images were generated from the collected TPEF/SHG signal [Figure 1A], and used to assess the cross-sectional region of both hydrated and dehydrated film samples produced using water-annealing or MeOH treatments. The thickness measurements were used to calculate silk film thickness swelling ratios (Q), and later used to assess mechanical properties.

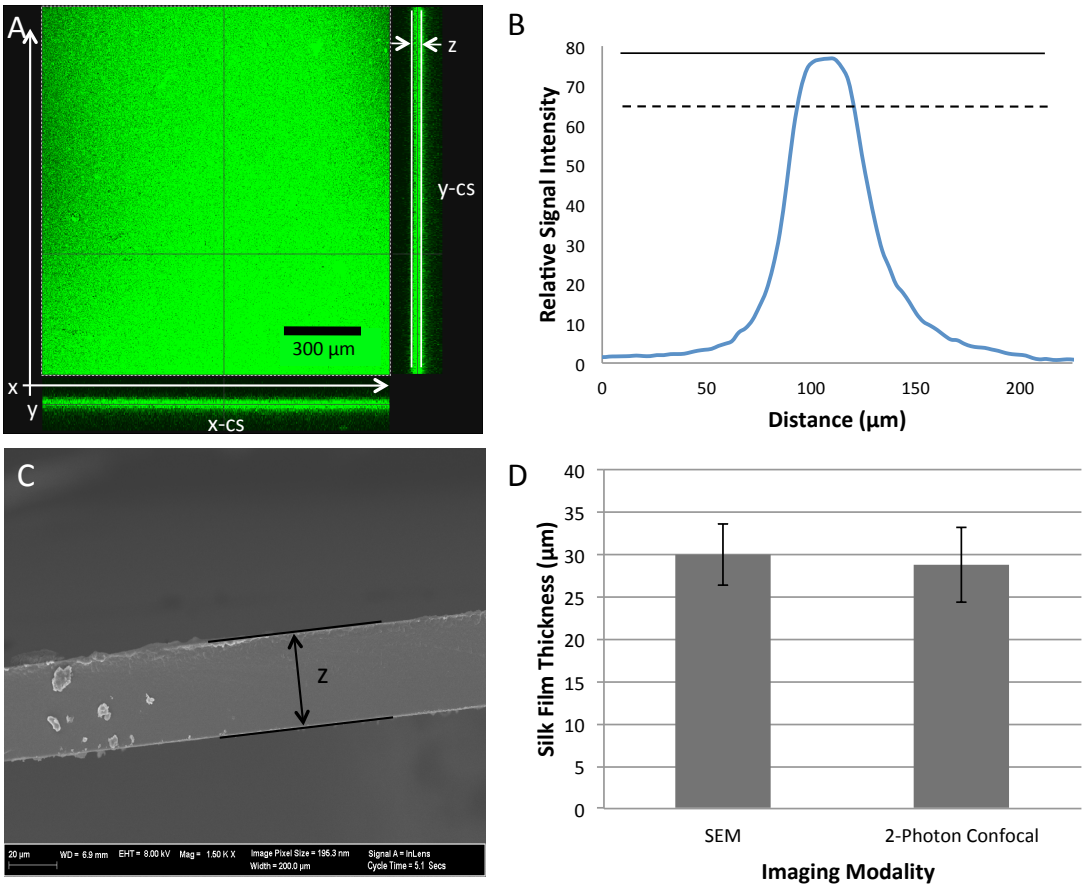


**Figure 1.** (A) Representative z-stack images of both end face and cross-sectional views generated from the collected TPEF/SHG signal using 2-photon confocal microscopy. Both x-z (x-cs) and y-z (y-cs) cross sectional images are shown at the bottom and right of the end face view, respectively. (B) Representative signal distribution obtained from z-stack images that illustrate the maximal intensity (solid line) and the signal cutoff at 80% maximal signal (dashed line) (C) Representative SEM image of silk film sample cross-section. (D) Results from validation study showing similar film thickness values achieved from both imaging modalities for randomly selected samples from both treatment conditions (n = 4, error bars = SD).

The center of the neck region for each sample was used for imaging. Film thickness was determined by measuring the distance between the 80% initial maximum positions from collected TPEF/SHG signal distribution curves generated from 2-photon confocal microscopy z-stack images [Figure 1B]. This signal threshold was validated by comparing the TPEF/SHG signal distribution distances to SEM cross-sectional measurements for randomly selected dog-bone silk film samples from both MeOH immersion and water-annealed treatments [Figure 1C]. Randomly selected dehydrated sample thicknesses from both processing conditions were obtained from both imaging modalities. The results of this experiment indicate that TPEF/SHG analysis provides the same thickness measurements as standard SEM analysis for dry sample thicknesses, providing validation for the use of the 2-photon excited imaging modality for film thickness measurement [Figure 1D]. The results also suggest that the hydration level in the films is low under dehydrated conditions at ambient conditions, as otherwise, significant artifacts would be anticipated during SEM analysis, which was not the case.

Silk film thickness measurements and swelling ratios (Q) were collected for both hydrated and dehydrated states using the TPEF/SHG signal distribution [Table 1]. Silk films treated by MeOH immersion showed a statistical increase in thickness in the hydrated state when compared to the dehydrated state [Figure 2A]. However, water-annealed silk films did not show significant differences in thickness between hydrated and dehydrated states.

**Table 1.** Silk film sample thickness ($\delta_H$, $\delta_D$) and swelling ratios (Q) obtained from 2-photon confocal imaging for both hydrated and dehydrated processing conditions.

| Sample | Water-annealed | | | MeOH Immersion | | |
|---|---|---|---|---|---|---|
| | $\delta_H$ | $\delta_D$ | Q | $\delta_H$ | $\delta_D$ | Q |
| 1 | 31.0 | 31.0 | 1.0 | 48.0 | 31.0 | 1.5 |
| 2 | 36.0 | 35.0 | 1.0 | 37.0 | 24.0 | 1..5 |
| 3 | 32.5 | 30.0 | 1.1 | 52.0 | 32.0 | 1.6 |
| **Avg** | **33.2** | **32.0** | **1.0** | **45.7** | **29.0** | **1.6** |
| **St Dev** | **2.6** | **2.6** | **0.1** | **7.8** | **4.4** | **0.1** |

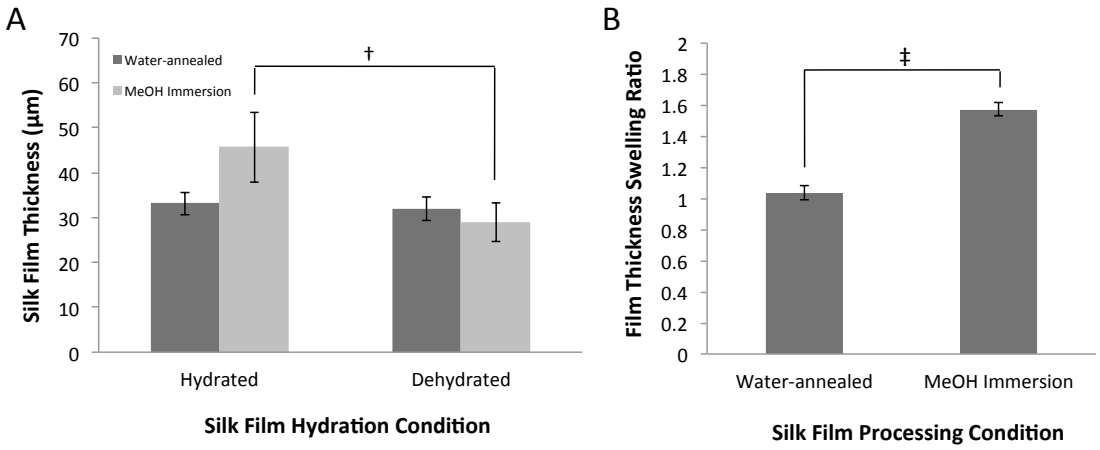


**Figure 2.** (A) Silk film thicknesses for dog-bone film geometries measured from 2-photon confocal microscopy for both hydrated and dehydrated conditions. Hydrated MeOH immersion treated films had a statistically significant increase in thickness when compared to their dehydrated state († indicates $p < 0.05$, $n = 3$, error bars = SD). Water annealed films showed no significant change in thickness between hydrated and dehydrated states. (B) The silk film thickness swelling ratio for MeOH immersion treated films was significantly greater then water-annealed film samples (‡ indicates $p < 0.001$, $n = 3$, error bars = SD).

These results indicate that there is a difference in silk film swelling due to the hydration state and treatment conditions. A statistically significant increase in Q for MeOH immersed silk film samples was found when compared to water-annealed samples [Figure 2B]. These results demonstrate that silk film samples treated by MeOH immersion have a nearly 60% increase in film thickness when placed in a hydrated environment. Previously, it has been demonstrated that water-annealed film samples had a nearly 3 fold decrease in β-sheet content when compared to MeOH treated films (26). Therefore, increasing β-sheet content by MeOH immersion is directly related to increased silk film thickness after hydration. These results suggest greater water absorption is occurring in the MeOH immersed films when compared to the water-annealed samples. Thus, these results infer that β-sheet content and secondary structure organization play a significant role in silk film water absorption properties.

### 4.2. Silk Film Mechanical Properties

Silk films with dog-bone geometries were submerged in 0.1M PBS solution and heated to 37˚C before testing to better represent physiological conditions during uniaxial mechanical testing. All samples were then pulled to failure at a 10 mm/min cross-head rate. Failure was absolute for every sample and was confined to the neck region of the dog-bone geometry. Representative stress-strain curves for both water-annealed and MeOH immersed films are shown in

Figure 3. The two processing conditions exhibited similar force vs. axial strain profiles, which is indicative that both materials possess similar mechanical properties when tested in the hydrated testing state. This result is somewhat unexpected as it has been previously demonstrated that MeOH immersed silk films have greater β-sheet content than water-annealed films, and this increased β-sheet content has been thought to result in enhanced stiffness in the dry testing states (26,40). However, hydrated films exhibit over an order magnitude decrease in tensile strength when compared to dehydrated samples for both processing conditions (40). Therefore, this result indicates that the presence of water had a significant effect on silk film mechanical properties regardless of β-sheet content.

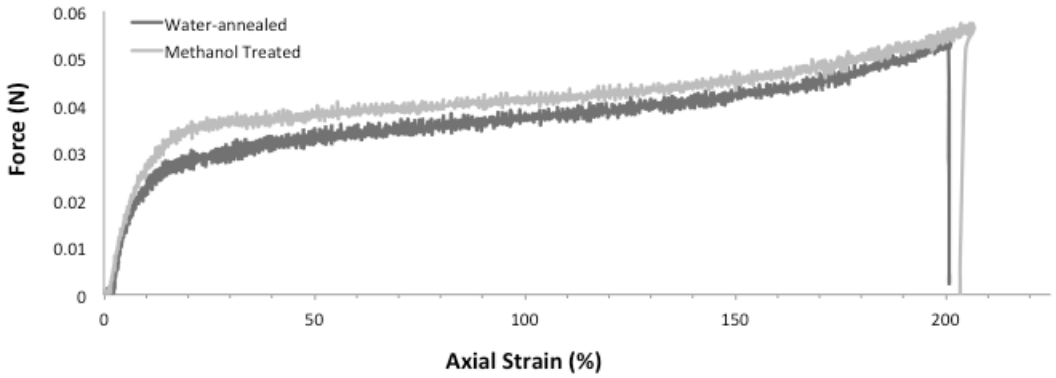


**Figure 3.** Representative stress versus strain curves for water-annealed (light grey) and MeOH (dark grey) treated silk films. Young's modulus, ultimate tensile strength, and elongation until failure length are slightly reduced for water-annealed silk film measurements.

Both processing conditions resulted in similar elongation to failure values [Table 2], in which both sets of samples failed at around 140% strain. This was approximately two orders of magnitude increase in elongation to failure when compared to dehydrated samples from both processing conditions. These results indicate that the silk films exhibit an increase in plastic deformation within a hydrated environment when compared to their dry states. However, it is uncertain if there is an increase in elastic deformation for the hydrated state. These results further support the notion that water acts as a plasticizer between the fibroin proteins forming the silk film (43).

**Table 2.** Silk film mechanical properties for different processing conditions.

| **Water-annealed Samples** | | | | | | |
|---|---|---|---|---|---|---|
| **Sample** | **Film Thickness (um)** | **Cross-Sect Area ($mm^2$)** | **Young's Modulus (MPa)** | **Yield Strength (MPa)** | **Ultimate Tensile Strength (MPa)** | **Elongation to Failure (%)** |
| 1 | 36 | 0.11 | 23.02 | 1.93 | 3.48 | 131 |
| 2 | 35 | 0.11 | 23.48 | 2.10 | 4.69 | 197 |
| 3 | 37 | 0.12 | 20.32 | 2.08 | 3.26 | 138 |
| 4 | 31 | 0.10 | 21.05 | 1.91 | 3.01 | 80 |
| **Avg** | **35** | **0.11** | **21.97** | **2.00** | **3.61** | **136** |
| **St Dev** | **3** | **0.01** | **1.52** | **0.10** | **0.75** | **48** |
| **MeOH Immersed Samples** | | | | | | |
| **Sample** | **Film Thickness (um)** | **Cross-Sect Area ($mm^2$)** | **Young's Modulus (MPa)** | **Yield Strength (MPa)** | **Ultimate Tensile Strength (MPa)** | **Elongation to Failure (%)** |
| 1 | 63 | 0.20 | 21.89 | 1.77 | 3.74 | 159 |
| 2 | 48 | 0.15 | 9.24 | 2.53 | 3.19 | 135 |
| 3 | 41 | 0.13 | 25.51 | 2.17 | 3.72 | 97 |
| 4 | 41 | 0.13 | 18.15 | 2.64 | 5.42 | 204 |
| **Avg** | **48** | **0.15** | **18.70** | **2.28** | **4.02** | **149** |
| **St Dev** | **10** | **0.03** | **6.98** | **0.40** | **0.97** | **45** |

A significant increase ($p < 0.05$, $n = 4$) in average silk film cross-sectional area was found for MeOH immersed samples when compared to water-annealed samples. These results infer that silk film material failure is primarily a function of fibroin chain breaks after extended plastic deformation, and material failure appears to be less a function of water absorption. A three-fold increase in the standard deviation was found for MeOH immersed samples when compared to water-annealed samples. This increase in standard deviation is likely due to greater silk film thickness non-uniformity caused by increased water-absorption, which most likely correspond to the overall degree of molecular organization within and between the amorphous and crystalline domains of the film. More specifically, the increased β-sheet content within MeOH treated films as compared to water-annealed films appears to be an indicator for the degree of film thickness swelling. Thus, in the dry testing state the presence of greater β-sheet content corresponds with enhanced silk film stiffness, while in the hydrated testing state increased β-sheet content corresponds with increased water absorption, which has a greater affect on increasing material ductility as opposed to promoting enhanced material strength.

### 4.3. Water Absorption and Thermal Stability Determined by TGA

The differences observed in silk film thickness between the water-annealed and MeOH immersed samples show that greater water absorption occurred in

the MeOH immersed samples. Thermal gravimetric analysis (TGA) was performed on both hydrated and dehydrated silk film samples to determine how much water absorption occurred and the affect on material properties [Figure 4AB]. TGA profiles for dehydrated samples did not significantly differ between the two processing conditions, and mass loss due to water was not found to be statistically different [Table 3]. However, a difference in TGA profiles was noted between the two processing groups for the hydrated samples. Hydrated water-annealed films exhibited a statistically significant increase ($p<0.005$, $n=3$) in mass loss of water when compared to the hydrated methanol treated films. These results indicate that MeOH immersed films absorb more water comparatively to water-annealed films in the hydrated state. These results correspond with the above silk film thickness measurements indicating an increase in thickness for hydrated MeOH films when compared to their dehydrated state.

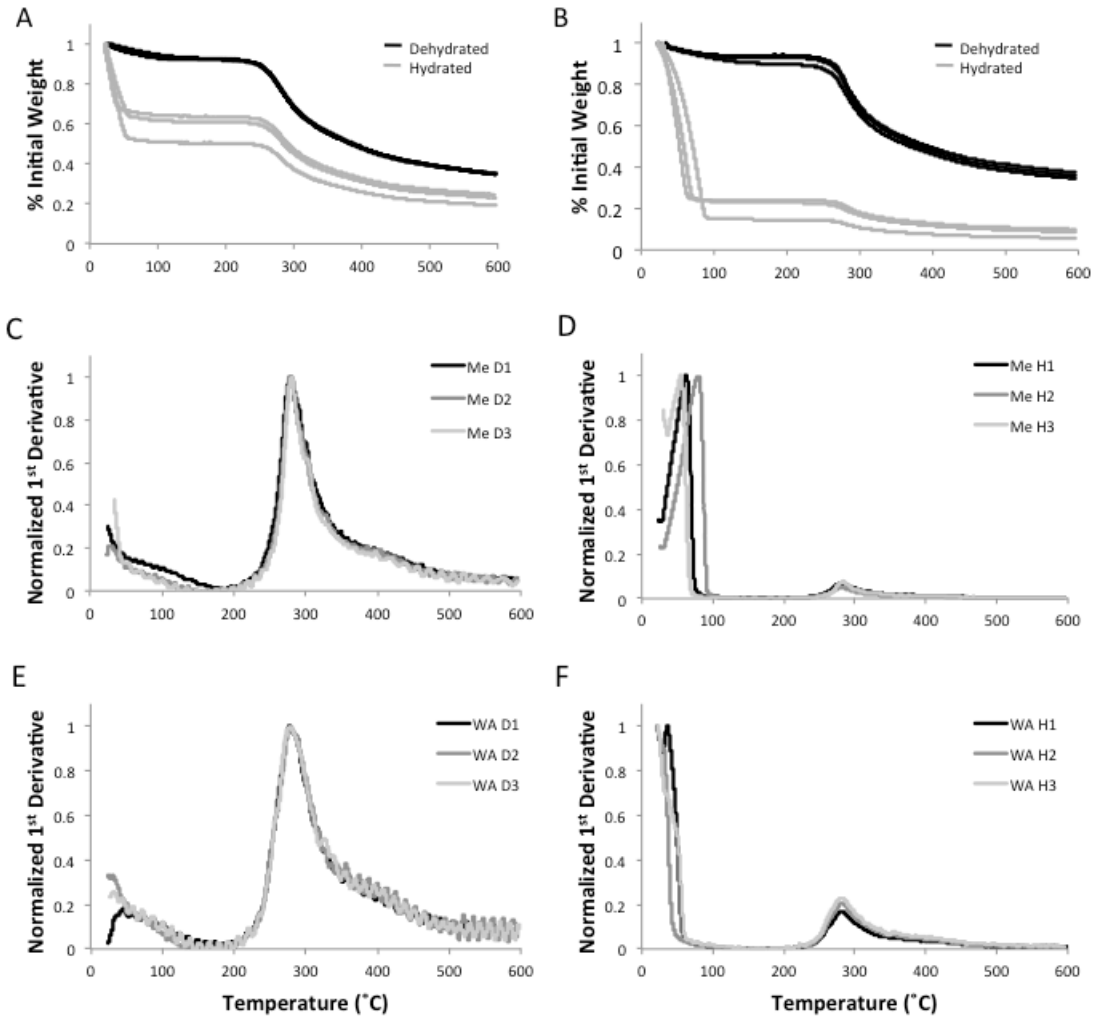


**Figure 4.** TGA mass loss profiles with respect to increasing temperature for hydrated (H1-3) and dehydrated (D1-3) silk fibroin films processed for (A) water-annealed and (B) MeOH immersed treatment methods. Normalized TGA 1st derivative profiles for (C, D) methanol treated (Me) and (E, F) water-annealed (WA) films in the hydrated (H) and dehydrated (D) state, respectively. Primary peaks were found for hydrated samples that correspond to water loss due to evaporation in addition to the secondary peaks indicating material degradation.

**Table 3.** Water mass loss (%) for hydrated and dehydrated silk film samples for different processing conditions.

| Sample | Water-annealed | | MeOH Immersion | |
|---|---|---|---|---|
| | Hydrated | Dehydrated | Hydrated | Dehydrated |
| 1 | 49 | 7 | 77 | 10 |
| 2 | 36 | 8 | 85 | 7 |
| 3 | 39 | 8 | 76 | 6 |
| **Avg** | **41.3** | **7.7** | **79.3** | **7.7** |
| **St Dev** | **6.8** | **0.6** | **4.9** | **2.1** |

The results of TGA 1st derivative analysis are summarized in Table 4. The 1st derivative plotted profiles demonstrated significant differences in both plot profiles and peak location between the hydrated and dehydrated silk film samples [Figure 4C-F]. For dehydrated silk film samples there was a statistically significant ($p<0.01$, $n=3$) shift to a higher material degradation temperature for methanol treated samples when compare to water-annealed films [Figure 4C-D]. This observation has been previously shown in the literature and has been suggested to be related to greater β-sheet secondary structure formation within the film bulk material of MeOH treated films (31,43). In contrast, the location of the 1st derivative position corresponding to the material degradation phase shift, the second small peak, did not change between hydrated samples of different processing conditions [Figure 4D,F]. In addition, hydrated samples exhibited a large 1st peak, which likely corresponding to water loss due to evaporation. This first peak was shifted to a higher temperature for methanol treated samples and did not appear for two

of the three water-annealed samples. This indicated that more energy was required to evaporate absorbed water from the MeOH immersed silk films when compared to water-annealed samples. Additionally, the larger size of the first peak for MeOH immersed samples indicated a greater phase shift when compared to water-annealed samples, which corresponds to a greater release of absorbed water.

**Table 4.** The 1st derivative peak positions calculated from the TGA mass loss profiles of hydrated and dehydrated silk film samples from different processing conditions.

| Sample | Water-Annealed | | | MeOH Immersion | | |
|---|---|---|---|---|---|---|
| | Hydrated | | Dehydrated | Hydrated | | Dehydrated |
| | 1st Peak | 2nd Peak | | 1st Peak | 2nd Peak | |
| 1 | 24.1 | 276.0 | 276.0 | 76.0 | 276.5 | 280.0 |
| 2 | NA | 270.0 | 275.0 | 52.5 | 275.0 | 279.0 |
| 3 | NA | 271.6 | 274.8 | 52.8 | 270.0 | 278.0 |
| **Avg** | **24.1** | **272.5** | **275.3** | **60.4** | **273.8** | **279.0** |
| **St Dev** | **NA** | **3.1** | **0.6** | **13.5** | **3.4** | **1.0** |

### 4.4. Silk Film $O_2$ Permeability and FTIR Analysis

Adequate oxygen diffusion throughout a scaffold construct is a requirement for the maintenance of living cells, especially in relation to a 3D environment. In addition, oxygen permeability can provide useful insight into silk protein secondary structure organization post processing. Therefore, the impact of β-sheet crystalline content on both oxygen permeability (Dk) and secondary

structure organization within the films was assessed. The values for silk film thickness, $O_2$GTR, Dk, and time to steady state permeability for various conditions are listed in Table 5.

**Table 5.** Silk film thickness and oxygen permeability properties for multiple processing and RH conditions.

| Testing Condition | FilmThickness (µm) | $O_2$GTR (mL $O_2$/$m^2$·d) | | Dk [$10^{-11}$(mL $O_2$·cm)/(s·$cm^2$·mmHg)] | | Time to Steady State (min) |
|---|---|---|---|---|---|---|
| | | 15 (min) | 135 (min) | 15 (min) | 135 (min) | |
| Water-annealed @ 80% RH | 29.6 ± 6.3 | 4,143 ± 1,953 | 4,245 ± 1,989 | 1.75 ± 0.43 | 1.80 ± 0.41 | 65 ± 8.66 |
| MeOH treated @ 80% RH | 95.7 ± 2.4 | 2,971 ± 91 | 3,701 ± 61 | 4.07 ± 1.50 | 5.07 ± 1.44 | > 135 |
| Water-annealed @ 50% RH | 40.5 ± 9.7 | 375.0 ± 54.7 | 54.7 ± 25.7 | 0.21 ± 0.05 | 0 | 50 ± 8.66 |
| MeOH treated@ 50% RH | 89.1 ± 1.4 | 1,655 ± 704 | 185 ± 104 | 2.25 ± 0.98 | 0.25 ± 0.14 | > 135 |

RH – relative humidity; $O_2$GTR – oxygen transmissibility; Dk – oxygen permeability coefficient (n=3, error=SD)

Dk was plotted versus time for both RH conditions for each silk film treatment method [Figure 5]. Dk increased over time for both silk film processing conditions at 80% RH, while samples tested in 50% RH conditions exhibited a decrease in Dk over time. MeOH treated silk films exhibited increased oxygen permeability over time for both RH conditions when compared to water-annealed samples. Furthermore, MeOH treated samples exhibited a persistent change in Dk values over time for both RH conditions over the entire 135 minute testing period. These results indicate that the MeOH treated films go through a greater change in secondary structure. However, water-annealed samples reached rapid stabilization for both RH conditions, at 50 and 65 minutes on average for both 50% and 80% RH

conditions, respectively. These results indicate that water-annealed silk film secondary structure reaches stabilization at a more rapid rate. Furthermore, the extended length of Dk stabilization exhibited by MeOH treated silk films corresponds to their greater water absorption properties. As a result the MeOH treated films have greater Dk instability profiles when compared to water-annealed samples due to their increased hydrated state which impacts the silk film secondary structure and ultimately the oxygen permeability rates through this structure.

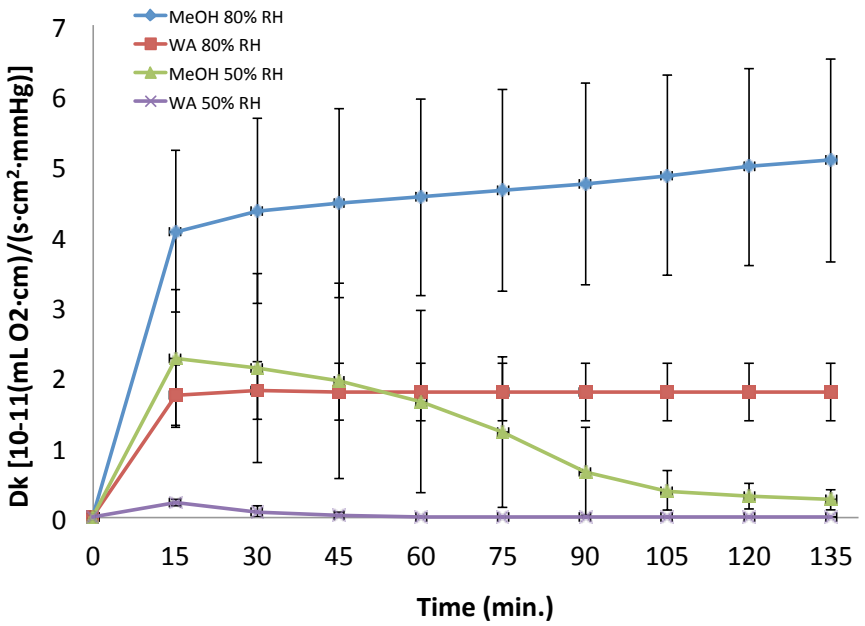


**Figure 5.** Oxygen permeability (Dk) profiles versus time for both MeOH treated and water-annealed (WA) silk film samples at 50% and 80% relative humidity (RH) conditions (n = 3, error bars = SD).

Dk values for all samples were found to increase over the first 15 minutes of experimentation, while after 135 minutes the Dk values decreased for both treatment methods at 50% RH conditions [Table 5]. Additionally, a significant difference ($p < 0.05$, $n = 3$) was shown between water-annealed and MeOH treated films at 80% RH for both time points, indicating that the selected film processing method changes the oxygen permeability properties for silk films in hydrated conditions. Similar results were shown for films run at 50% RH conditions in which MeOH treated films showed a significantly higher Dk value for both time points. The above results infer that MeOH treatment is producing a difference in protein secondary structure within the silk film bulk region that is more permeable to oxygen than the structure formed through water-anneal processing.

These results compared favorably with previously published data for MeOH treated silk films in the hydrated state (110,111). However, no previous $O_2$ permeability studies have been undertaken for water-annealed silk films. It has been previously shown that water-annealed silk film secondary structure is more amorphous when compared to MeOH treated films (26). The difference in permeability rates between the more crystalline MeOH films and the more amorphous water-annealed films may be attributed to the packing structure of the fibroin protein chains. Amorphous chain movement will be more inhibited when in close proximity to crystalline regions within the bulk polymer structure (111). Previously it has been suggested that water-annealed films exhibit a

tighter packing structure within the bulk region then MeOH treated films. This is thought to be due to the relatively slow rate of secondary structure formation during the water-annealing process (< 4 hours) as compared to MeOH treated films in which the β-sheet structure is formed at a relatively rapid rate (< 20 minutes) (26,30,40). The rapid β-sheet structure induced through MeOH treatment may produce a more disorganized structure between the crystalline and amorphous regions, which enables greater water absorption and increased chain movement within the bulk structure, and thus greater oxygen permeability. As a result there is an increase in Dk for MeOH treated films when compared to water-annealed samples.

Further FTIR analysis of silk film secondary structure pre- and post-testing for $O_2$ permeability provides further evidence that water-annealed films exhibit a tighter packing order when compared to MeOH treated films. After exposure to different humidity conditions (50% and 80% RH) during $O_2$ permeability testing, water-annealed films were found to have increasing amounts of β-sheet content as the amount of water vapor flowing through the sample increased [Figure 6]. A distinct shift of the random coil peak of 1645 $cm^{-1}$ to the distinctive β-sheet peak located around 1620 $cm^{-1}$ can be observed. In addition, a slight increasing β-sheet peak can also be seen around 1700 $cm^{-1}$ in the FTIR spectra (25,26,31).

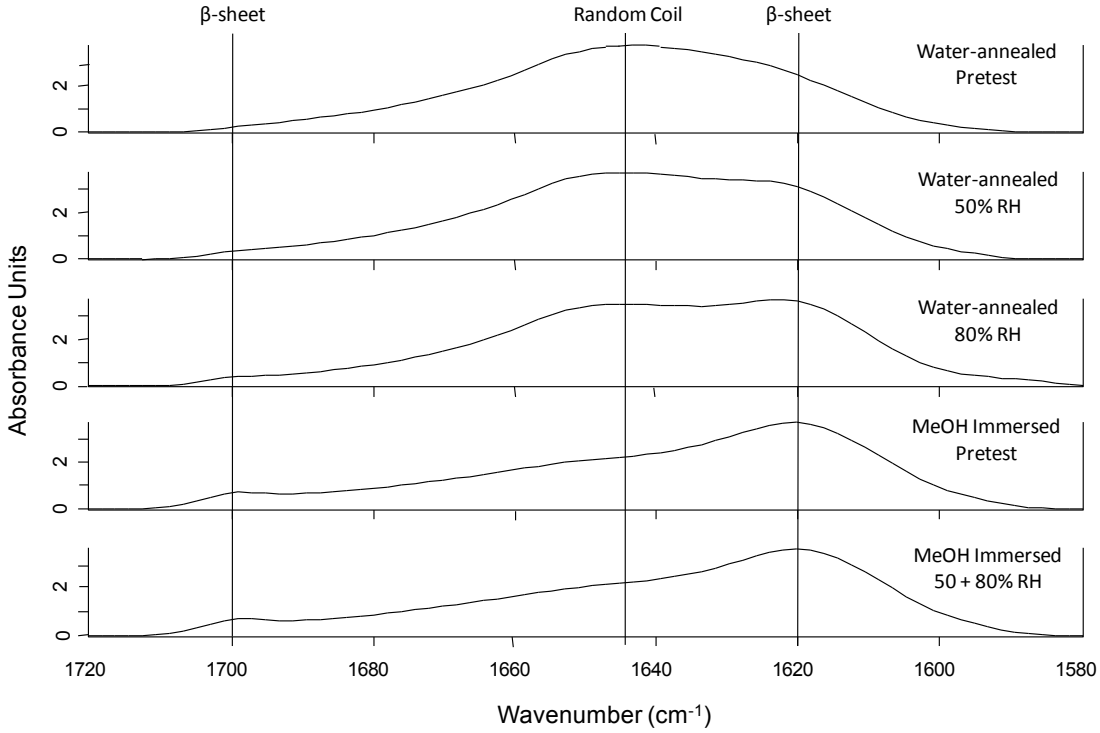


**Figure 6.** FTIR spectrum of silk film samples before and after exposure to varying amounts of water-vapor. Distinct spectral signatures for both random coil and β-sheet structures are shown, and sample type is given at right.

However, MeOH treated samples for both pretested and tested samples indicated no change in peak signatures, thus indicating that the β-sheet crystalline structure is fully set before water vapor exposure [Figure 6]. These results indicate that the water-annealed bulk protein chains are continuing to undergo structural rearrangement upon exposure to varying amounts of water-vapor which then settles over time. These results correspond with the above $O_2$ permeability results in which the water-annealed films form a tighter barrier to $O_2$ when compared to MeOH treated samples. This is likely due to the water-anneal film's bulk secondary structure

rearranging to a more densely packed β-sheet crystalline conformation, as opposed to a more randomly ordered β-sheet crystalline matrix formed for MeOH treated films [Figure 7].

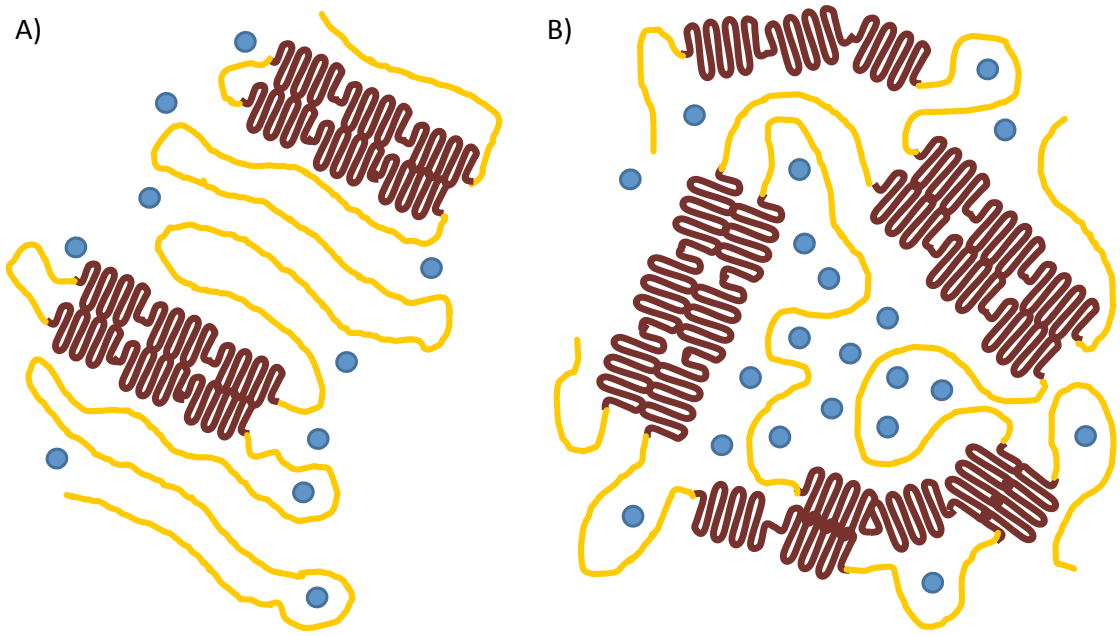


**Figure 7.** Schematic representation of silk film secondary structure organization for amorphous (yellow), β-sheet crystalline regions (brown), and water molecules (blue) for both water-annealed (a) and MeOH immersed processing methods. Water-annealing produces less crystalline content but increased ordering of overall secondary structure, while the MeOH treatment produces greater β-sheet content with a highly disordered packing structure. As a result channel-like regions are produced in the amorphous spacing within the MeOH treated films that increases water absorption and oxygen permeability when compared to water-annealed films.

## 5. Conclusion

This study demonstrates that silk film hydration influences material property outcomes dependent on the choice of processing technique employed. The organization of silk film secondary structure of both amorphous and crystalline regions greatly influences water absorption, and hence dictates material properties such as swelling ratio, mechanical strength, and oxygen permeability. It was determined that MeOH treated films exhibited a less ordered secondary structure arrangement when compared to water-annealed films. As a result, the less ordered MeOH treated films possessed a greater capacity to absorb water and reach higher rates of oxygen permeability. Although one of the most intriguing aspects of silk is the potential to dial-in crystalline content similar to an engineering polymer, this control has to be managed through controlled water content in order to generate materials with consistent material properties. Further work will have to be undertaken to understand how controlled hydration input can be used to produce desired material properties. In summary, the breadth of silk utility is directly related to its varying secondary structures, which in turn are largely dictated by hydration.

CHAPTER 3

# Silk Film Culture System for *In Vitro* Analysis and Biomaterial Design

## 1. Summary

A silk film in vitro culture system was developed that can be consistently scaled-up for a variety of experimental setups. Of immediate interest is the use of the silk film's inherent ability to be surface patterned to enable the evaluation of cell response to the presence biomaterial surface topography. Silk films with parallel lined features were produced with high fidelity, sterilized, and successfully seeded with a human corneal limbal-epithelial cell line. The transparency and handleability of the silk film post seeding allowed for a number of in vitro biochemical and imaging analysis to be performed, including proliferation assays, time-lapse imaging, and scanning electron microscopy (SEM). Cell response was significantly affected by the presence of the topography through noticeable cell alignment and migration parallel to the feature edge. The adaptability of the culture system will allow for further exploration of cell response to silk film biomaterials.

## 2. Introduction

Silk films are promising protein-based biomaterials that can be fabricated with high fidelity and economically within a research laboratory environment (4,25). These materials are desirable because they possess highly controllable

dimensional and material characteristics, are biocompatible and promote cell adhesion, can be modified through topographic patterning or by chemically altering the surface, and can be used as a depot for biologically active molecules for drug delivery related applications (6,9,25,107,116,117) . In addition, silk films are relatively straightforward to custom design, can be designed to dissolve within minutes or degrade over years in vitro or in vivo, and are produce with the added benefit of being transparent in nature and therefore highly suitable for imaging applications (7,21,106,118,119). The culture system methodology presented here represents a scalable approach for rapid assessments of cell-silk film surface interactions. Of particular interest is the use of surface patterned silk films to study differences in cell proliferation and responses of cells for alignment (21,120) . The seeded cultures were cultured on both micro-patterned and flat silk film substrates, and then assessed through time-lapse phase-contrast imaging, scanning electron microscopy, and biochemical assessment of metabolic activity and nucleic acid content. In summary, the silk film in vitro culture system offers a customizable experimental setup suitable to the study of cell-surface interactions on a biomaterial substrate, which can then be optimized and then translated to in vivo models. Observations using the culture system presented here are currently being used to aid in applications ranging from basic cell interactions to medical device design, and thus are relevant to a broad range of biomedical fields.

## 3. Materials and Methods

### 3.1. Patterned Silicon Wafer Production

Silicon wafers possessing parallel line topographies were prepared using standard photolithographic and ion etching techniques. The features composing the various geometric surface topographies possessed dimensions measuring a 2-um width, 4-um pitch, and 1.5-um depth. Width and pitch measurements were chosen based on previous literature that demonstrated these dimensions produced a contact guidance effect upon corneal epithelium that modulated various cellular characteristics such as alignment and adhesion (40,80,104,121,122). The 1.5-um depth was chosen based on previously cited experiments that indicated this depth appears to have a negligible effect on contact guidance effects (25,123). A 21-die array in a [3:5:5:5:3] design was fabricated upon a 100-mm silicon wafer. Individual dies have a 10-mm diameter separated by 5-mm spacing. Feature dimensions were verified using scanning electron microscopy (SEM).

Photolithography mask patterns were designed using L-edit software (Tanner EDA, Inc.) and then imported into a DWL66 laser pattern generator and direct write machine (Heidelberg Instruments, Heidelberg, Germany) for production onto a photoresist coated glass substrate. The finished mask was then placed within an Autostep 200 DSW i-line wafer stepper (GCA, Inc.) for photolithographic patterning of photoresist coated 100-mm diameter silicon wafers. Wafers coated with 1-um thick layer of photoresist (Megaposit™

SPR™ 220-3.0, Dow Chemical, Inc.) were produced that possessed the 21-die wafer array. The wafers were then placed into a Unaxis 770 ion etching device (Plasma-Therm, LLC, St. Petersburg, FL) to produce 1.5-um depth etch. The above process was designed to provide repeated topographic features measuring 2-um in width, 4-um in pitch, and 1.5-um in depth over a circular surface area with a 1-cm diameter. Feature sizes were then imaged using an Ultra SEM (Zeiss, Inc.).

### 3.2. Silk Film Production and Cell Seeding Protocol

In order to better enable the reader to replicate the silk film production methodology the protocol is written below in a step-by-step format. In addition, a published video documenting the methodology can be found at the following website: http://www.jove.com/video/3646/silk-film-culture-system-for-in-vitro-analysis-and-biomaterial-design

#### 3.2.1. Fabrication of silicone rubber molds

1. Produce or purchase a desired topographic surface for casting. For this publication a standard 100-mm etched silicon wafer will be described (Figure 1).
2. Weigh out polydimethylsiloxane (PDMS) potting (component A) and catalyst (component B) solution in a 1:9 ratio (9-g potting and 1-g catalyst) as provided in the purchased kit.

3. Mix solutions thoroughly to initiate curing process.
4. Place silicon wafer surface within a casting dish.
5. Weigh out 4.5-g of PDMS solution onto silicon wafer
6. Spread PDMS solution as to cover a 100-mm diameter area of the wafer surface.
7. Tilt wafer to spread PDMS solution evenly.
8. Cover wafer with 100-mm diameter petri dish lid with hole in top to allow for venting.
9. Place casting setup into 60°C oven over night, making certain that curing is taking place on a flat surface.
10. Place cured PDMS/silicon wafer into 70% ethanol bath before removal.
11. Begin removing PDMS from wafer by using razor blade to lift edge (entire circumference) first.
12. Gently pull PDMS off using forceps within a 70% ethanol bath being careful not to tear silicone rubber casting.
13. Punch out individual PDMS molds using 14-mm hole punch. This diameter is designed to fit into a 24-well plate setup.

### 3.2.2. Production of silk solution

1. Bring 2-L of distilled water ($dH_2O$) to a boil within a glass beaker (25) .
2. Cut 5-g of *Bombyx mori* silkworm cocoons into thirds.

3. Dispose of extensively contaminated cocoons as indicated by excessive insect particulates coating the inner cocoon surface.
4. Measure 4.24-g of sodium carbonate.
5. Add sodium carbonate slowly to boiling $dH_2O$ volume to prevent boiling over of water, and allow complete dissolution before continuing.
6. Add cocoon pieces to boiling $dH_2O$ for 40-min., and use a Teflon coated stir bar to stir cocoons during boiling process.
7. After boiling, carefully drain $dH_2O$ into sink and ring out the silk extract by hand to remove excess water.
8. Wash silk extract three times for 20-min. each in 1-L of $dH_2O$ in plastic beaker, and use a stir bar to circulate volume within beaker.
9. After washing, ring out the silk extract by hand and place silk fiber extract inside a chemical hood to allow for drying for a 12-hr. period.
10. Next day, weigh the dried silk fibers, which is typically ~3.5-g: _____-g
11. Prepare 9.3-M LiBr solution for a 20% w/v solution of silk. Utilize following equations to calculate necessary weight and volumes:
    a. (Silk extract weight from step 10) x (4) = _____-mL of total 9.3 M LiBr solution
    b. [(807.705)x(LiBr volume from part 11.a)]/1000 = _____-g of LiBr to add to $dH_2O$

12. Add measured LiBr weight into a glass beaker of the following $dH_2O$ volume:
    a. (0.8) x (calculated volume from step 11.a) = _____-mL of $dH_2O$
13. Pour this solution into an appropriate sized graduated cylinder, and bring solution up to final volume as calculated in part 11.a.
14. Place the silk extract into beaker and pour LiBr solution over the silk fibers making sure the silk fibers are immersed within LiBr solution using a lab spatula.
15. Place the dissolved silk into 60°C oven for 4-hours:
    Start time: _____
    End time: _____
16. Using an appropriate sized syringe draw up 12-mL of the silk solution. Place an 18G needle on end of the syringe, and then inject the solution into a dialysis casette (3,500 MW coutoff, Slide-A-Lyzer, Thermo Scientific). After filling the cassette, draw the remaining air out of the cassette with the emptied syringe.
17. Place filled dialysis cassette within 1-L of $dH_2O$.
18. Change $dH_2O$ volume after 1 h, 4h, 8hr and then every 12 hours 3x for a total of 6 changes:
    a. Begin: _____
    b. 1hr: _____

c. 4hr: _____

d. 8 hr: _____

e. 12 hr: _____

f. 12 hr: _____

g. 12 hr: _____

h. End: _____

19. After dialysis, slowly collect the silk solution from cassettes with syringe. Place solution into 10,000-g rated centrifuge tubes.
20. Centrifuge the solution twice at 10,000-g at 4°C for 20-min each. After each centrifugation place supernatant into a new tube.
21. Store thr silk solution in 4°C refrigerator.
22. Pipette 2 samples of 0.5-mL silk solution into small weigh dish, and place weigh dishes inside a 60°C dry oven for 12 hours or until the silk solution dries.
23. Weigh the remaining solid silk film from both samples to measure silk protein concentration density of the solution:
    a. Weight of combined 2 silk film samples:_____-mg
    b. (Weight from 23.a) x (100) = _____% silk

### 3.2.3. Preparation of silk films and culture system setup

1. Prepare PDMS casting surfaces by cleaning with clear tape to remove dust.

2. Clean PDMS substrates by soaking in 70% EtOH and wash three times with $dH_2O$.
3. Place 14 mm PDMS molds onto holder plate, which is typically a 24-well plate lid.
4. To produce a 50-um thick film, spread 70-uls of 8% silk solution on PDMS molds using a liquid spreading tool that is typically a 1-mL syringe tip (26) .
5. Allow the silk films to dry uncovered on a clean bench running an air flow pressure of 150 Pa for a period of 90-min or until films are dry.
6. Once films are dry place entire set of films, including PDMS molds, into a water-annealing chamber for >4-hrs to produce a water insoluble film. This is typically an empty desiccator chamber with water in the bottom of the basin pulled at a 25 kPa vacuum (40) .
7. Remove silk films from water-annealing chamber and place onto a clean bench.
8. Prepare a 70% EtOH bath within a 35-mm Petri dish, and place control substrates (i.e. glass or plastic surfaces) and stainless steel rings within wells for at least 10-min to sterilize.
9. Remove silk films from PDMS molds using forceps, dip them into 70% EtOH, and place sample into 24-well plate prefilled with 1-mL of 70% EtOH making sure patterned side is facing up to allow for cell adhesion.

10. After placing each silk film sample into a corresponding well place stainless steel ring weights (11.65-mm inner diameter, 15.45-mm outer diameter, and 1.18-mm thickness) on top.
11. Allow samples with rings to incubate for 10 minutes to ensure sterility.
12. Remove EtOH and wash each sample 3x with 1-mL of PBS. Let each wash sit for 5-min to allow for complete diffusion.
13. Remove PBS using aspirating glass pipette, while making sure to remove majority of bubbles beneath silk film samples.
14. Prepare cell line for seeding. As an example, trypsinize human corneal-limbal epithelial (HCLE) cell line with 0.25% trypsin and ethylenediaminetetraacetic acid (EDTA) solution for 7-min. Deactivate trypsin using 1:1 volume of Dulbecco's modified Eagle medium (DMEM) passage media with 10% FBS added. Centrifuge trypsinized HCLE cells, add 8-mL of keratinocyte-serum free media (K-SFM) to cell pellet, gently agitate to disperse HCLEs, and generate cell count.
15. Sample 500-uL of HCLE suspension per well typically using a 10,000 cells/$cm^2$ density.
16. Place cultures within incubator at 37°C and 5% $CO_2$ and run desired experimental protocol.

### 3.3. Human Corneal Limbal-Epithelial Cell Culture

A human corneal limbal epithelial cell line (HCLE) was generously provided by

Dr. Ilene Gipson (Schepens Eye Research Institute, Harvard Medical School) and stored in liquid nitrogen. Prior to seeding on the SF or AM substrates, cells were thawed and cultured for 24 to 48-hours in keratinocyte-SFM medium (Gibco, Invitrogen Corporation, Grand Island, NY, USA) supplemented with 0.2ng/ml mouse epithelial growth factor (EGF, Invitrogen), 1% Penicillin-Streptomycin (P/S, VWR), bovine pituitary extract (BPE, Invitrogen) and 0.1% $CaCl_2.2H_2O$ (Invitrogen).

### 3.4. Scanning Electron Microscopy (SEM)

HCLE cultures grown on both silk films and glass surfaces were fixed in 400-µL of Karnovsky's fixative for 45-minutes at room temperature and washed in Phosphate-Buffered Saline (PBS, VWR) 3 times. After the samples were dehydrated in a graded series of ethanol (50, 80, 90 and 100%, VWR), for 7-minutes respectively. Samples were then further dried using hexamethyldisiloxane (HMDS, Sigma-Aldrich, Inc.) solvent to remove residual water saturation for 2-minutes and then allowed to dry for 2-hours in a desiccator[23]. After HDMS processing, samples were sputter coated with gold for 90-seconds leaving an approximate 2-nm coating on the samples. Films were then imaged using a Quanta 600 environmental chamber SEM (FEI, Inc., Hillsboro, OR).

### 3.5. Cell Proliferation Assays

HCLE cultures were collected for 3-(4,5 – Dimethiazol-2-yl)-2,5-diphenyltetrazolium bromide (MTT) assay at 2 and 8-days post seeding (n = 4) following manufacturer instructions. Briefly, 50-uL of MTT stock solution (5mg/mL, Invitrogen) was added to the cultures containing 500-uL of fresh medium and incubate at 37 °C for 4 hours in the dark. After the medium was aspirated, 200-uL of Dimethyl Sulfoxide (Sigma**)** was added and mixed thoroughly to release the formazan. 100-uL of the resultant solution was transferred into clear 96-well plates (VWR), and the absorbance was recorded at 540-nm using a Biomek plate reader (Beckman Coulter, Brea, CA, USA). Silk films without cells were set up as negative controls.

The CyQuant NF (Invitrogen, Inc., Eugene, OR) assay was utilized to assess cellular nucleic acid content as a measure of initial cellular adhesion and culture proliferation upon the various silk film substrates and glass coverslip controls. After 2 and 8-days of cell culture 500-uL of CyQuant NF solution was added to each sample (n = 4 for each surface) including a blank control that was incubated without the presence of cells and incubated for 2-hours at 37°C. Then 200-uL of post-incubation sample solution was collected into a 96-well plate. Sample fluorescence intensity was then measured using a SpectraMax M2 fluorimeter microplate reader (Molecular Devices, Inc., Sunnyvale, CA) with excitation wavelength at 485-nm and emission wavelength collected at 530-nm. Averaged blank control values were

subtracted from all sample readings.

### 3.6. Time-Lapse Phase-Contrast Imaging of HCLE Migration

Phase contrast images were taken using an Observer Z1 fluorescent microscope (Carl Zeiss, AG) with either a 10x (NA 0.45 air) objective lens utilizing a 1.6 Optivar optic (OV) as indicated. An AxioCam single channel camera and AxioVision software (Carl Zeiss, AG) were used to capture all images as indicated. After a 2-hour incubation to allow for cells attachment cell migration was monitored using a 24-well plate micro-incubator (PeCon, GmbH; M24 S1). Time-lapse phase contrast imaging was utilized to record a frame every 10-minutes over a 10-hour period.

## 4. Results

Surface topography and design was successfully translated into a photolithography process. This process was successfully utilized to produce an array of 1-cm diameter patterned silicon wafer topographies [Figure 1A]. Analysis of SEM images revealed that the feature dimensional design was produced successfully [Figure 1B-C]. The patterned silicon surfaces were then used to produce patterned PDMS surfaces with negative image replications. The PDMS surfaces were successfully patterned, and used to produced patterned silk film surfaces as previously described (25). SEM imaging revealed that flat [Figure 1D] and patterned [Figure 1E] silk film

surfaces were successfully produced. In addition, the silk film topographic dimension were successfully transferred from the PDMS molds [Figure 1F].

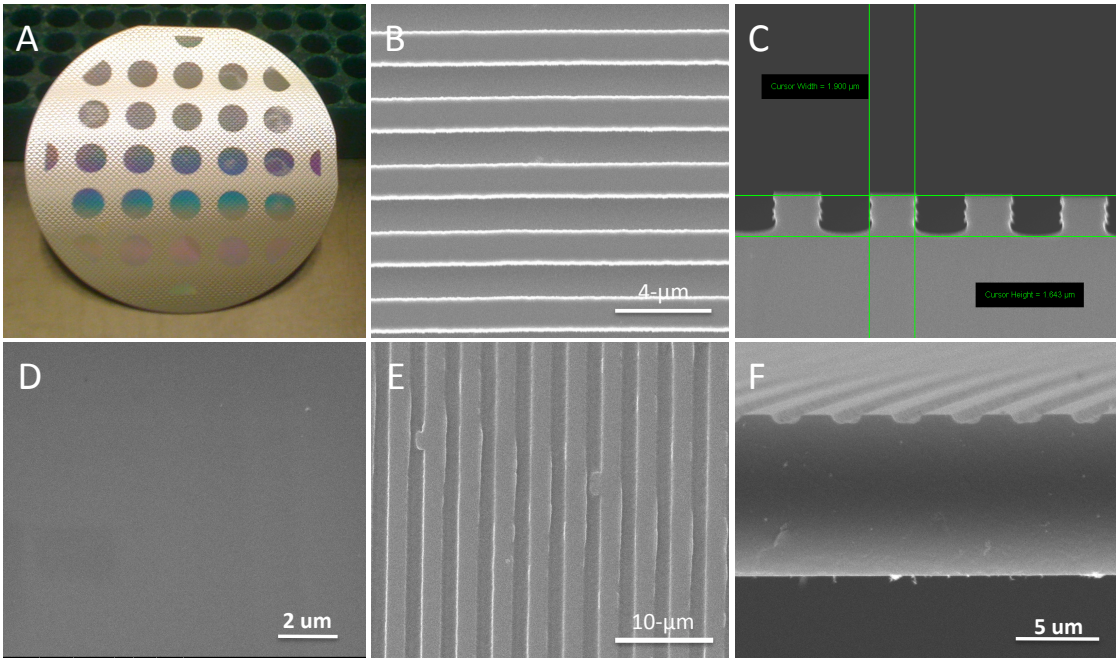


**Figure 1.** (A) An array of patterned line surface topographies was produced upon a 90-mm diameter silicon wafer using standard photolithographic and dry etching techniques. (B) SEM imaging revealed successful production of the anticipated silicon topography, with (C) desired etched feature depth. SEM images of both (D) Flat and (E-F) patterned silk films had the pattern successfully transferred to their surfaces.

HCLE cells successfully adhered to the silk film silk film surfaces and culture growth characteristics compared favorably to glass control surfaces [Figure 2]. SEM imaging revealed that silk films adhered successfully to both patterned and flat silk film surfaces at day 1 in culture, and cell morphologies

appeared similar to controls [Figure 2A-C]. Confluent cell layers began to form by 4-days in culture on all surfaces [Figure 2D-F], and continued to proliferate to form densely packed cell sheets with stratifying cells [Figure 2G-I]. Cell proliferation was assessed by metabolic activity and nucleic acid content assays indicated that cell growth was similar by 2-days in culture for all surfaces [Figure 2J-K]. By day 8 in culture glass controls were found to have higher increases in metabolic activity and nucleic acid content when compared to silk film surfaces. However, the presence of the topography did not appear to affect cell proliferation as readings were similar between flat and patterned silk surfaces.

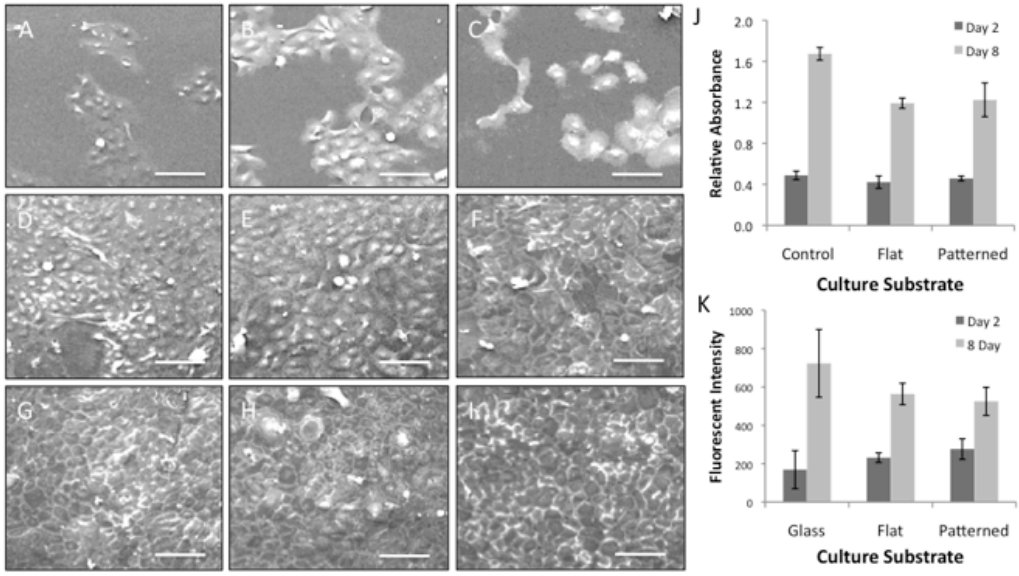


**Figure 2.** SEM images of HCLE cultures grown on (A, D, G) Patterned silk films, (B, E, H) flat silk films, and (C, F, I) glass surfaces at (A-C) 1, (D-F) 4, and (G-I) 8-days in culture (scale bars = 100 um). (J) Nucleic acid content and (K) metabolic activity was assessed upon the various surfaces demonstrating similar HCLE viability on both patterned and flat silk film substrates when compared to glass control surfaces over time (n = 4, error bars = SD).

SEM imaging was utilized to image cell-to-surface attachment of HCLEs growing on the flat and patterned silk surfaces. After 2-days in culture, cells tended to align in the parallel direction of the silk film topography and appeared to form attachments along the feature edge [Figure 3A]. This was not the case on flat silk surfaces where cells did not align and were less elongated in morphology [Figure 3B]. After 8-days in culture the cells grew to confluence and differences in cell alignment and morphology between patterned and flat where no longer significant [Figure 3C-D].

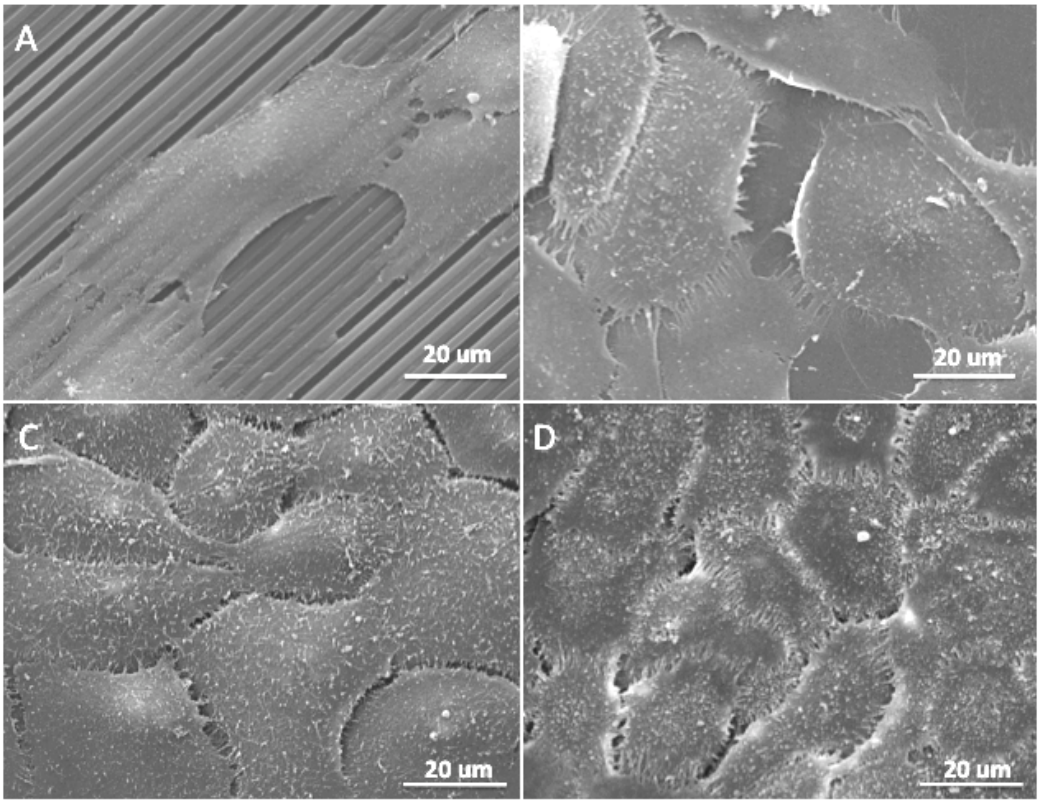


**Figure 3.** Scanning electron micrographs of HCLE cell line adhering to (A) patterned and (B) flat silk films at day 2 in culture. HCLE cultures continue to proliferate to confluence on (C) patterned and (D) flat surfaces by day 8 in culture.

HCLE migration upon both patterned and flat silk film surfaces were studied using time-lapse phase-contrast microscopy. Imaging revealed that cell migration was significantly altered by the presence of the surface topography. On patterned surface cells tended to migrate in the parallel direction along the topography edge over time [Figure 4A-C], while on flat silk films migration was in random direction [Figure 4D-F]. In addition, single cells tended to not move perpendicular to the silk film topography, which manifested in track-like guiding effect that the topography imposed on HCLE movement.

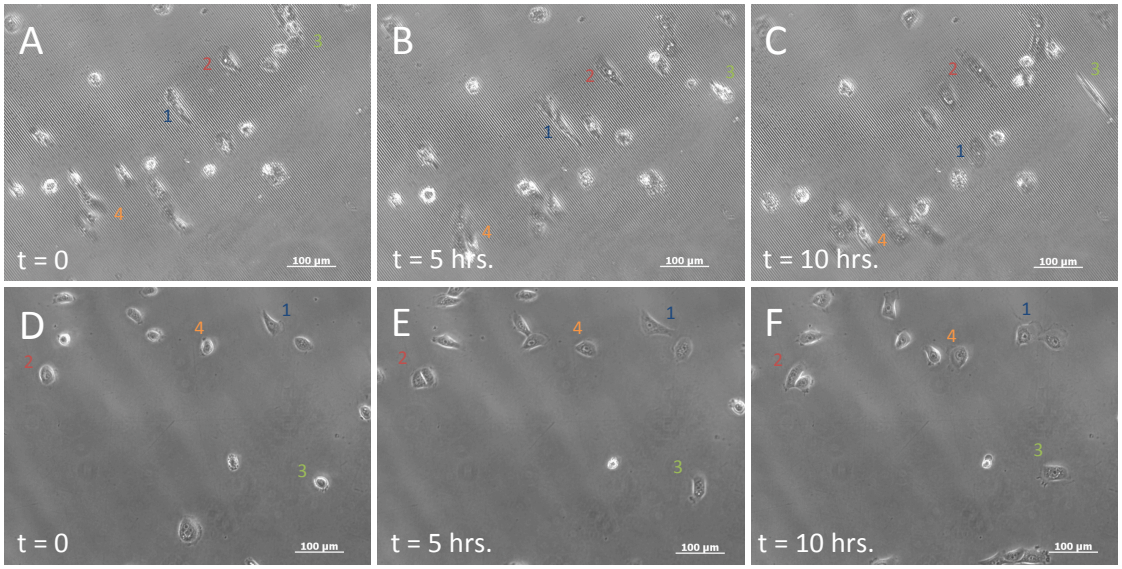


**Figure 4.** Time-lapse phase contrast imaging of HCLE cells migrating on (A-C) patterned and (D-F) flat silk film surfaces over time in culture. A total of 4-cell movements were highlighted on both surfaces. Cell movement on patterned surfaces demonstrated a track-like guiding effect which was not observed on flat silk surfaces.

## 5. Discussion

The use of regenerated silk films as a substrate for cell culture has gained in popularity over the past two decades due to extensive characterization of the material properties of this protein and increased understanding of its biomaterial utility (6,9) . The culture system described here represents a novel in vitro testing system for assessing cell surface interactions on patterned silk film biomaterial substrates (25) . The system allows for in depth analysis of cellular interactions over time that can be easily adopted for high-throughput data collection. This is largely enabled because silk films possess a number of tunable biomaterial properties that can be modified to directly affect cell function (7,9,21), including: control of surface micro/nano-surface topography (25); various surface chemistries through covalent modification or adsorption of biologically active molecules (119); robust mechanical properties (40,124); control of material hydrophilicity/hydrophobicity (124); bulk loading of biological compounds for release (9,107,125); and controlled dissolution/enzymatic degradation rates through control of the secondary structure (beta sheet content) (106,126,127). Silk film substrates are produced in the lab with high fidelity, consistency, and with relatively low cost. This enables reproducibility in both culture system setup and experimental outcomes. A summary of the silk film production method is shown in Figure 5.

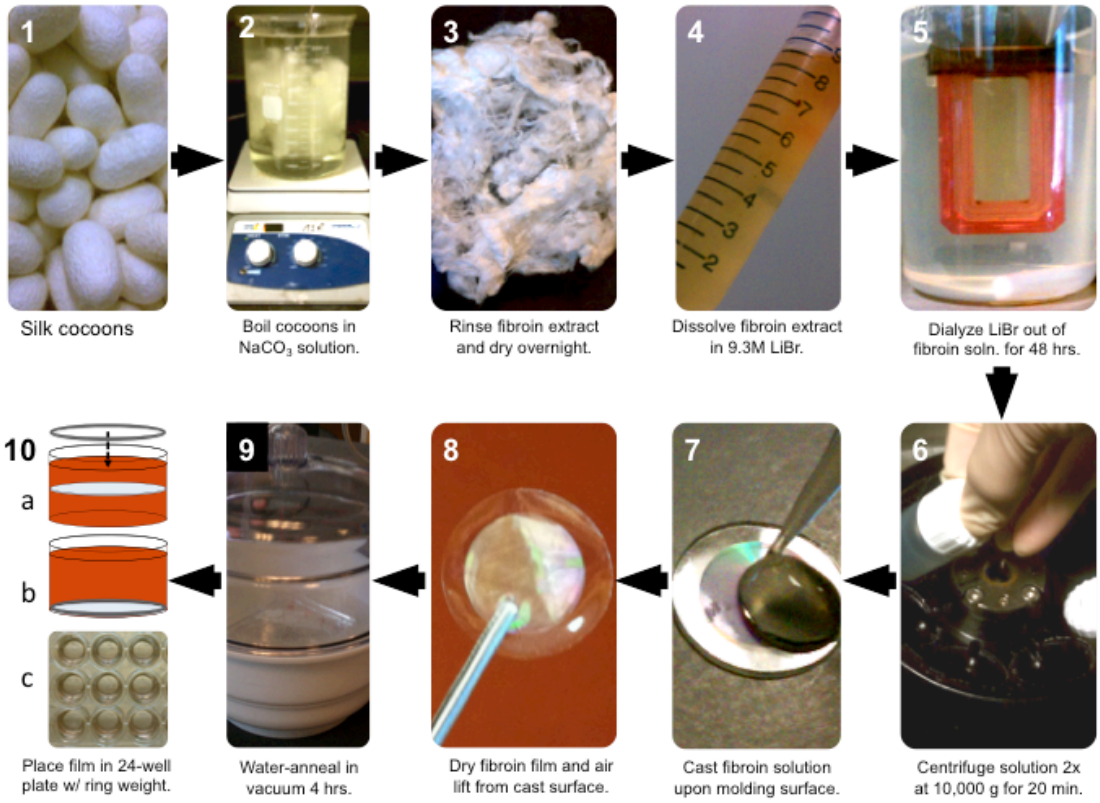


**Figure 5.** A visual flow chart summarizing the silk film production and culture system preparation protocol in 10-steps. (1-6) Silk cocoons are solubilized into solution, (7-8) the solution is cast onto patterned surfaces into films, (8) the films are processed to become insoluble, and (10) then the substrates can be seeded with cells.

The transparency of silk films is achieved through water-annealing the films for a period of time under vacuum in the presence of water vapor (25,40). This processing approach allows for the formation of β-sheet secondary structure, fostering the insolubility of the material in water while allowing minimal diffraction of light (40). This transparency of films is key in enabling

direct live-cell imaging that can be employed under a number of imaging modalities (i.e. wide-field and fluorescence) using any number of microscope systems (21,112). In addition to live-cell imaging, silk films can be easily removed from the culture system to allow for additional fixation and analysis. Thus, the large variety of direct experimental assessments that can be performed on this system are applicable to a wide variety of cell/tissue sources for many technical fields (6,7,9,21,54,119).

It has been demonstrated that water-anneal processing produces a stable silk film material within culture that has defined degradation rates pending the concentration of proteases in solution (26,32,40). As a result these materials may be used for extended periods of time for long-term cell culture, or remain implanted for months or years depending on the physiological location (9). In addition, recent work has shown that both the protein structure and material properties of water-annealed silk films are consistent from batch to batch allowing for reproducible culture results as shown through various mechanical and biophysical testing methods (40,124). In addition, the material's surface has shown great fidelity amongst film batches as indicated by SEM, atomic force micrscopy (AFM), and cell culture studies (25,47,128). Material stability and consistency is an important factor to how the cell will sense the culture substrate through the various mechanotransduction pathways, and ultimately produce a desired/undesired cellular response (85,129).

## 6. Conclusion

The silk film culture system allows for an adaptable and scalable approach to using these biomaterial substrates for a variety of experimental setups. Historical standards for culture substrates, such as tissue culture treated plastic or glass, provide adequate substrates for cell attachment. However, these materials are not amendable for further utility in vivo. It can be envisioned that a silk film biomaterial could be customized in vitro, and once experimental expectations have been achieved the customized film may be directly translated to an in vivo model. Such paired design between in vitro and in vivo experimentation offers a great advantage for using silk films in developing translational technologies. Further work will utilize this system to explore basic scientific understanding with the hope of translating this knowledge to the clinical setting.

CHAPTER 4

# Silk Fibroin as a Biomaterial Substrate for Corneal Epithelial Cell Sheet Generation In Vitro

## 1. Summary

Silk fibroin (SF) biomaterial was evaluated as a substrate for corneal epithelial cell proliferation, differentiation and stratification *in vitro* compared with denuded human amniotic membrane (AM). Primary human and rabbit corneal epithelial cells and immortalized human corneal limbal epithelial cells were cultured on the SF and denuded AM, respectively. The biological cell behavior including the morphology, proliferation, differentiation and stratification on the two substrates were compared and analyzed. Corneal epithelial cells can adhere and proliferate on the SF and denuded AM with a cobblestone appearance, abundant microvilli on the surface and wide connection with the adjacent cells. MTT assay showed that cell proliferation on denuded AM was statistically higher than that on SF at 24 and 72 hours post plating ($p = 0.001$ and 0.0005, respectively). Expression of ΔNp63a and Keratin 3/12 were detected in primary cells cultures on the two substrates with no statistical difference. When cultured at the air-liquid interface for 7 days, cells on SF could form a comparable stratified graft with a 2 to 3 cell layering which compared similarly to AM cultures. SF, a novel biomaterial, could support

corneal epithelial cells to proliferate, differentiate and stratify retaining the normal characteristic epithelium phenotype. Compared with AM, its unique features including the transparency, ease of handling and transfer, and inherent freedom from disease transmission make it a promising substrate for corneal wound repair and tissue engineering purposes.

## 2. Introduction

With the substantial advancement of regenerative medicine and tissue engineering techniques, stem cell therapy has been successfully practiced to treat refractory ocular surface disorders such as limbal stem cell deficiency (63,130). To establish a cell sheet for transplantation, a suitable substrate carrier is required to transfer the cells from laboratory benchtop to bedside. A series of biomaterial based substrates have been tested experimentally and/or clinically, such as human amniotic membrane (AM) (73,131,132) fibrin glue (76,77), temperature responsive polymers (133,134), and acellular porcine lamellar stroma (135,136). Among them, human AM is the clinical standard substrate for ocular surface repair owing to its biological properties that inhibit inflammation, tissue scarring and angiogenesis (71).

However, limitations regarding the use of AM exist. These include relatively poor mechanical strength, semi-transparent appearance, difficulty of handling, and the potential risk of disease transmission. To overcome these limitations, a novel biomaterial, silk fibroin (SF), the primary structural protein

of *Bombyx mori* silkworm cocoons, has been explored and tested with remarkable progress. Previous studies have shown that SF could generate minimal immune and inflammatory responses when implanted within the body, and the material can be fully degraded by naturally occurring proteolytic enzymes (34,137). We have previously shown that thin films cast from SF could support the adherence, proliferation, and production of native matrix when human and rabbit fibroblasts were cultured in both 2D and 3D conditions, suggesting that these SF constructs can act as scaffolding for corneal stroma engineering purposes (21). This study sought to evaluate the application of SF as a carrier for corneal epithelial cell sheet generation by comparing the cell morphology, proliferation, differentiation, and stratification on SF with that of cultures on denuded human AM.

## 3. Materials and methods

### 3.1. Preparation of *Bombyx Mori* Silk Fibroin (SF) Films

Thin SF films were produced as described with minor modifications (5,53,138,139). The *Bombyx mori* silk cocoons were purchased from Tajima Shoji Co. (Yokohama, Japan), cut into small pieces, weighed, and boiled for 1-hour in distilled water containing 0.85 g of $Na_2CO_3$ for each gram of cocoon material. After boiling, the supernatant was discarded and the resulting fibrous material underwent three 20-minute washes in $dH_2O$ and then dried in a chemical fume hood for 12-hours. The dried cocoon material was dissolved in

a concentrated solution of 9.3M LiBr solution for 4-hours at 60ºC. The silk solution was dialyzed against water for 48 hours with 6 total water changes using a dialysis cassette with a molecular weight cut-off of 3,500-Da (Slide-A-Lyzer, Pierce). Following dialysis, 70-µL of the resulting 80-mg/mL silk solution was used directly to prepare films of fibroin by evaporation from a flat polydimethyl siloxane (PDMS) surface measuring 14-mm in diameter at room temperature within a biological clean bench (25). To produce water insoluble films the fibroin samples were water-annealed within a vacuum chamber pulled to 10-PSI and filled with $dH_2O$ in the basin for 4-hours, and allowed to dry for greater than 1-hour (40). Silk films were then sterilized by heating the films at 160°C for 2-hours in glass petri dishes. The films were placed in the bottom of 24-well tissue culture plates (VWR, Radnor, PA, USA). A similarly sterilized stainless steel o-ring (Superior Washer, Inc., Hauppauge, NY) measuring 15.4-mm in outer diameter and 11.6-mm in inner diameter was placed on top of each film to stabilize the substrate and prevent film floating during culture. The film was hydrated in PBS overnight at 4°C and before use, PBS was aspirated.

### 3.2. Preparation of Denuded Human Amniotic Membrane (AM)

Cryopreserved human AM was obtained from the Institute of Ophthalmology “Conde de Valenciana” (Mexico City, Mexico) and stored in -80°C. Prior to use, the AM was thawed by placing in a 37°C water bath for 20-minutes. The

procedure for denuding AM was carried out as descried previously (140). Briefly, in a sterile cell culture hood, native AM epithelium was removed by washing three times in PBS to remove storage medium and serum, and then incubating the AM in a 125-ug/mL thermolysin (Sigma-Aldrich, St. Louis, MO, USA) solution at room temperature for 9-minutes. After treatment, the AM was washed in PBS 3 times for 15-minutes each on a shaker to get rid of the cellular debris. AM samples both before and after epithelial removal were fixed with 4% paraformaldehyde solution (PFA, Electron Microscopy Sciences, Hatfield, PA, USA) and subjected to immunofluorescent staining of primary anti-pan cytokeratin antibody (AE1/AE3, Abcam, Cambridge, MA, USA). Additional pieces of AM were incubated in Karnovsky's fixative and underwent serial dehydration for scanning electron microscopic examination. For use as a carrier for cell culture, denuded AM was transferred to 24-well plates with basement membrane side up using fine forceps. The firm attachment of AM to the plates was achieved by air-drying the AM in a cell culture hood for 30-minutes.

### 3.3. Preparation of Human and Rabbit Limbal Epithelial (HCLE) Cells

A human corneal limbal epithelial cell line (HCLE) was generously provided by Dr. Ilene Gipson (Schepens Eye Research Institute, Harvard Medical School) and stored in liquid nitrogen. Prior to seeding on the SF or AM substrates, cells were thawed and cultured for 24 to 48-hours in keratinocyte-SFM medium

(Gibco, Invitrogen Corporation, Grand Island, NY, USA) supplemented with 0.2ng/ml mouse epithelial growth factor (EGF, Invitrogen), 1% Penicillin-Streptomycin (PS, VWR), bovine pituitary extract (BPE, Invitrogen) and 0.1% $CaCl_2.2H_2O$ (Invitrogen, Inc.). For preparation of primary cultures, either human limbal rings obtained from a regional eye bank (the Eye Bank for Sight Restoration, Inc., New York, NY, USA) or rabbit limbal tissue harvested from New Zealand white rabbits (Charles River Laboratories International, Inc., Wilmington, MA, USA) in accordance with the ARVO Statement for the Use of Animals in Ophthalmic and Vision Research and with federal, state, and local regulations, were processed as described below.

After careful removal of the iris, residual conjunctiva, endothelial layer, and trabecular meshwork, the corneoscleral ring was washed in EpiLife® medium (Invitrogen) containing 1% PS (VWR, Inc.) and 0.1% Fungizone (Invitrogen, Inc.) for 20-minutes, divided into quadrants 1mm x1mm in size and placed on a 6-well cell culture plate (VWR) precoated with 50-ug/mL collagen I (BD Biosciences, Bedford, MA, USA) with epithelium side down and incubated at 37°C and 5% $CO_2$ incubator for 20-minutes. One drop of EpiLife® medium supplemented with 1% human keratinocyte growth supplement (Invitrogen), with 1% P/S (VWR), 5% fetal bovine serum (FBS, Thermo Fisher Scientific Inc., Waltham, MA), 10µg/mL mouse EGF (Invitrogen), and $10^{-10}$ M cholera toxin A (Sigma) was added to each explant and cultured overnight in the incubator. The next day, 1-mL of complete EpiLife® culture medium was added

and the medium was changed every 3-days until 80% confluence was achieved. For subculture, cells were washed with Dulbecco's Phosphate-Buffered Saline (DPBS, VWR) twice and digested with TrypLE™ Express (Invitrogen) at 37°C for 12-minutes. A single cell suspension at a density of 2 x $10^4$ cells/$cm^2$ were seeded on SF and AM and cultured for 48 to 72-hours before they were collected and subjected to the following analysis.

### 3.4. Light microscopy

Cell cultures were observed with a Carl Zeiss Axiovison Microscope (Carl Zeiss Microimaging GmbH, Jena, Germany) daily. Images were taken with an Observer Z1 fluorescent microscope (Carl Zeiss, AG) a both 10x (NA 0.45 air) objective lenses utilizing a 1.6 Optivar optic. An AxioCam HRm digital camera (Zeiss) and AxioVision software were used to capture phase contrast images of cultures.

### 3.5. Scanning electron microscopy (SEM)

Denuded AM and cells sheet constructed on SF and AM were fixed in 400-µL of Karnovsky's fixative for 45-minutes at room temperature and washed in Phosphate-Buffered Saline (PBS, VWR) 3 times. After the samples were dehydrated in a graded series of ethanol (50, 80, 90 and 100%, VWR), for 7-minutes respectively. Samples were then further dried using hexamethyldisiloxane (HMDS, Sigma-Aldrich, Inc.) solvent to remove residual

water saturation for 2-minutes and then allowed to dry for 2-hours in a desiccator. After HDMS processing, samples were sputter coated with gold for 90-seconds leaving an approximate 2-nm coating on the samples. Films were then imaged using a Quanta 600 environmental chamber SEM (FEI, Inc., Hillsboro, OR).

### 3.6. Immunofluorescent staining

Both intact and denuded AM, cell cultures on SF and AM were fixed with 4% PFA (Electron Microscopy Sciences) for 15-minutes, while for p63 staining, samples were fixed with methanol (VWR) at -20°C for 10-minutes. After three washes in PBS (VWR) for 5-minutes each, samples were blocked and permeabilized with solution containing of 1% bovine serum albumin (BSA, Sigma), 0.25% Triton X-100 (EMD Chemicals, Darmstadt, Germany), and 2.5% donkey serum (Abcam, Inc.) in PBS for 50-minutes. Primary monoclonal antibodies recognizing keratin 3/12 (Abcam, Inc., 1:100), ΔNp63a (Cell Signaling Technology, Inc. Danvers, MA, 1:200) for human corneal epithelial cells (HCEC), and pan cytokeratin (AE1/AE3, Abcam, Inc., 1:100) for intact AM samples were applied and incubated overnight at 4°C. After extensive washing, secondary antibodies were then incubated for 1-hour using appropriate isotype matched non-specific IgG as controls. Samples were mounted with VECTASHIELD® Mounting Medium with DAPI (Vector Laboratories, Burlingame, CA, USA). Images were acquired using an

Observer Z1 fluorescent microscope (Carl Zeiss, AG) with both a 10x (NA 0.45 air) and 63x (NA 1.4 oil) objective lenses utilizing a 1.6 Optivar optic. An AxioCam HRm digital camera (Zeiss) and AxioVision 4.0 software was used to capture single and z-stack images (10-25 layer range) at 0.25-um slices using DAPI, GFP, and Texas Red filter channels. The percentage of K3/12 and ΔNp63a expression in the primary cells on SF and denuded AM was compared and analyzed.

### 3.7. Cell Proliferation

Primary rabbit corneal epithelial cells (RCEC) were seeded on SF and denuded AM (n = 3) at a cell density of $2 \times 10^4$ cells/$cm^2$ in a 24-well plate (VWR). The cultures were collected for MTT assay at 24, 48, 72 and 144-hours post seeding following manufacturer instructions. Briefly, 50-uL of MTT stock solution (5mg/mL, Invitrogen) was added to the cultures containing 500 uL of fresh medium and incubate at 37 °C for 4 hours in the dark. After the medium was aspirated, 200-uL of Dimethyl Sulfoxide (Sigma**)** was added and mixed thoroughly to release the formazan. 100-uL of the resultant solution was transferred into clear 96-well plates (VWR), and the absorbance was recorded at 540-nm using a Biomek plate reader (Beckman Coulter, Brea, CA, USA). Wells containing SF and AM without cells culturing were set up as negative controls.

### 3.8. Cell Stratification

Primary RCECs were seeded at a density of 5 x $10^4$ cells/$cm^2$ on SF and denuded AM placed on the Transwell inserts fitted for 12-well plates (Corning, Lowell, MA, USA) and co-cultured with mitomycin C (Sigma) treated NIH 3T3 cells at the bottom. After confluence, epithelial cells were cultured in an air-liquid interface for 1-week. Samples were collected and fixed with 4% PFA (Electron Microscopy Sciences) for 15-minutes. F-actin filaments were stained with Alexa Fluor 488® phalloidin (Invitrogen) and the cell nucleus with DAPI (Invitrogen) following the manufacture instruction. Prior to imaging, slides were mounted with VECTASHIELD® Mounting Medium with DAPI (Vector Laboratories).

Fluorescent images of f-actin formation were taken using an Observer Z1 fluorescent microscope (Carl Zeiss, AG) with a 63x (NA 1.4 oil) objective lenses. An AxioCam HRm digital camera and AxioVision software were used to capture z-stack images (20-60 layer range) at 0.200 um slices using DAPI and Texas Red filter channels. Deconvolution was performed on each z-stack using 3D Huygens Deconvolution Software (Scientific Volume Imaging BV, The Netherlands). A total of 40-iterations were performed employing the software's Classic Maximum Likelihood Estimation (CMLE) algorithm for each z-stack. All other settings were left at manufacturer default settings. Images were produced using both maximum intensity projection (MIP) and surface rendering settings. MIP threshold levels were set at default settings, while surface-rendering threshold matchrf MIP signal localization and intensity.

### 3.9. Statistical analysis

All data was presented as sample set mean ± standard deviation (SD) calculated for each group and compared using Student's unpaired t-test by Microsoft Excel (Microsoft Corporation, Redmont, WA). Test results were reported as two-tailed p values, where $p < 0.05$ was considered statistically significant.

## 4. Results

### 4.1. Morphology of Corneal Cells Cultured on SF and Denuded AM

Transparent circular SF films were made with 14-mm diameters and around a 40-μm axial thickness. After water-anneal processing was performed, the SF was non-dissolvable in culture medium and PBS. The SF was sterilized by heating the samples at 160°C for 2-hours. The shape and physical properties remained stable after the annealing and sterilization processes. The thin transparent SF film was easy to handle when grabbed with fine forceps. The mechanical strength was enough for in vitro culture and transfer. Before thermolysin treatment, uniform staining of pan-keratin recognizing the cytoskeleton of cells was observed within the entire amniotic epithelial layer [Figure 1A]. In contrast, after treatment, only residual cellular debris on the basement membrane stained by pan-keratin can be observed [Figure 1B]. SEM results confirmed the total removal of the epithelial cells with intact

basement membranes [Figure 1C-D], which is consistent with previous findings (140).

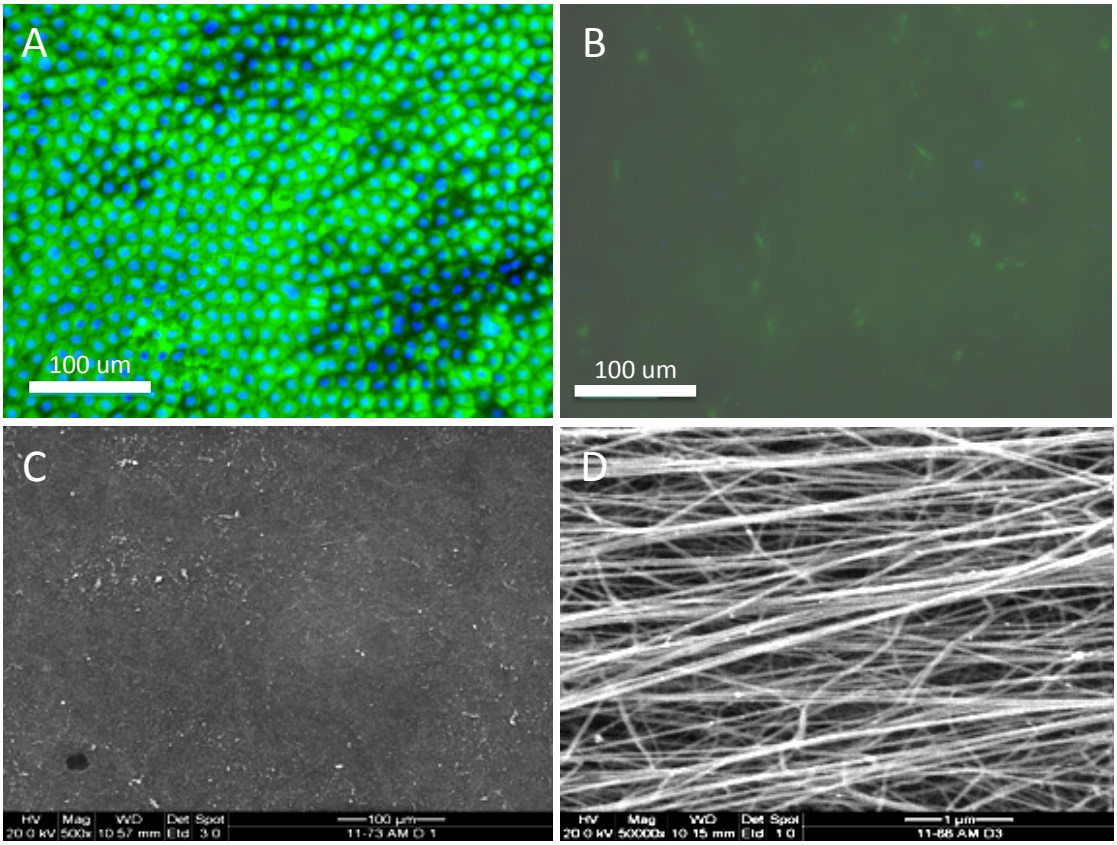


**Figure 1.** Denudation of cryopreserved amniotic membrane. AM with intact epithelium was illustrated by anti-pan cytokeratin staining (green) (A) before thermolysin treatment and (B) after treatment. Cell nuclei were counterstained with DAPI (blue). Scanning electron microscopic images of denuded AM showing the (C) denuded basement membrane and (D) a magnified image of the individual stromal fibers.

Denuded AM showed a semi-transparent appearance and the tendency of sticking together when lifted by two fine forceps [Figure 2A-B]. An Ultracell

surgical sponge (Aspen Surgical, Caledonia, MI, USA) was used to distinguish the orientation of the denuded AM, as the adherent side indicated the stroma presence. After air-drying, AM with basement membrane side up could firmly attach to either cell culture plate or Transwell insert, no detachment was observed during the subsequent cell culture. In contrast, silk film materials appeared transparent and also extremely handleable even after wetting [Figure 2C-D].

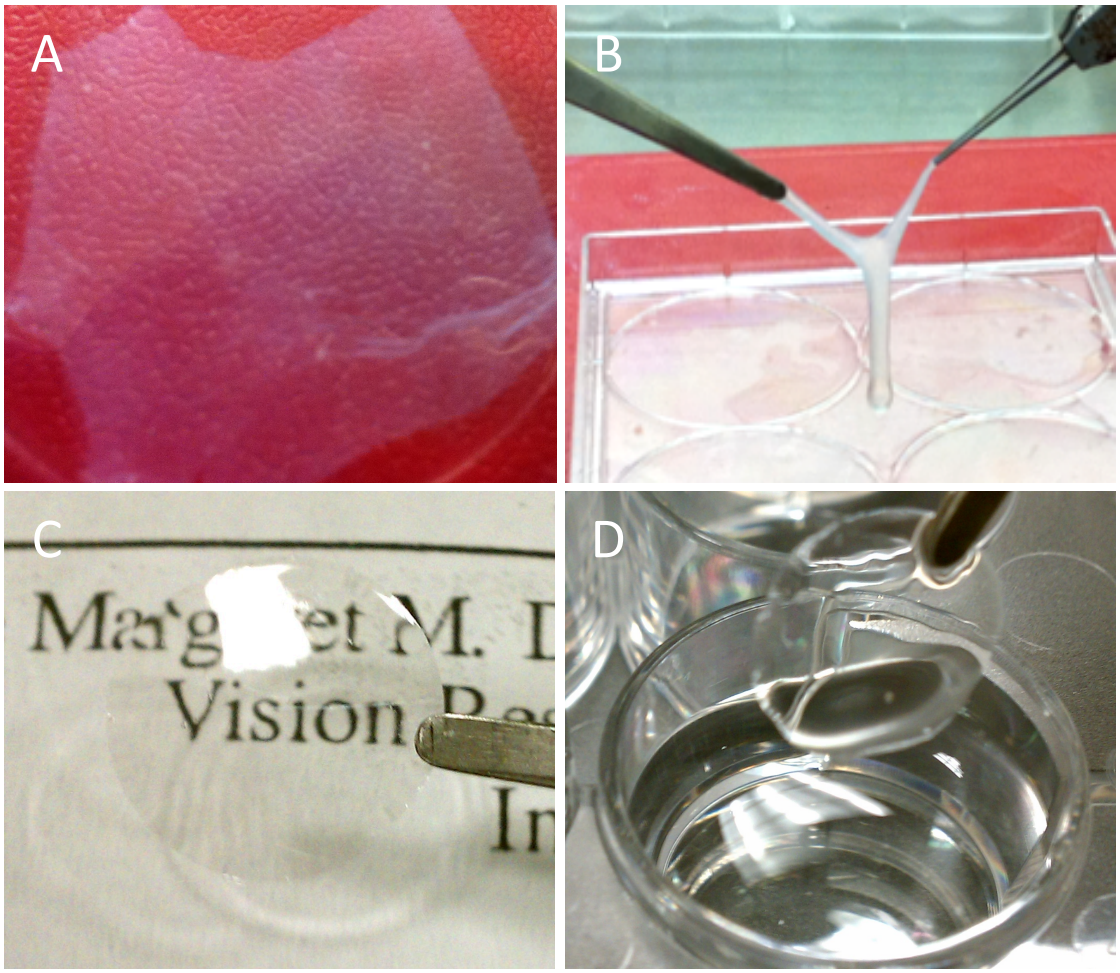


**Figure 2.** Gross images showed that denuded AM spread on the tissue culture plates was (A) semi-transparent, and (B) prone to fold then adhere together when it was lifted by two forceps. Silk film was (C) highly transparent and (D) maintained shape when handled.

Corneal epithelial cell cultures from all three donor sources could adhere and proliferate on SF and denuded AM with a polygonal appearance under phase contrast microscope [Figure 3A-C]. Abundant microvilli on the cell surface and wide junction with the neighbor cells can be viewed under SEM

[Figure D-F]. Primary corneal epithelial cells tended to form clusters and small colonies when seeded on SF at a low cell density, whereas, randomly distributed on denuded AM. No significant difference of cell morphology was observed in HCLE cultures on SF and AM. No significant toxic response to cells grown on either SF or AM, such as cell shrinkage, intracellular vacuole, detachment from the substrate, and cell death were observed during the culture process.

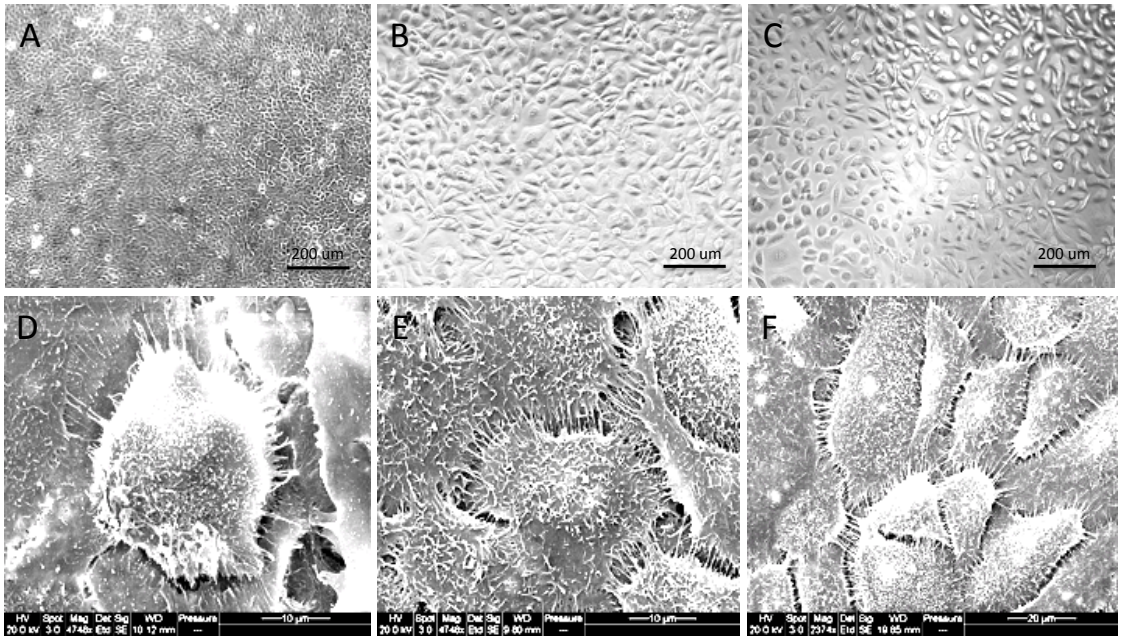


**Figure 3.** (A-C) Phase contrast images of corneal epithelial cells on SF (x10). (A) RCEC, (B) HCEC, (C) HCLE. (D-F) SEM images of corneal epithelial cells cultured on SF. (D) RCEC, (E) HCEC, and (F) HCLE demonstrating a high level of cell anchor point to the film surface, abundance of microvilli on the cell surface, and prevalent contacts between adjacent cells.

### 4.2. Cell Proliferation, Differentiation, and Stratification on SF and AM

In order to expand cells ex vivo on AM, the epithelial cells must be removed, or denuded, from the culturing surface. This enhances cell adherence through the formation of strong integrin-based adhesion complexes with the basement membrane (140). Denuding the amniotic epithelial layer with thermolysin treatment has been shown as an optimal method for tissue preparation for in vitro culture (140). The vast majority of RCEC adhered to the two substrates after 8-hours post seeding, and cell density continued to increase 1 and 6-days after cell seeding on both SF [Figure 4AC] and AM [Figure 4B and D]. MTT assays showed that the values of light absorbance of cells grown showed that the number of cells on denuded AM at 24 and 72-hours post seeding were significantly higher ($p = 0.001$) than that of cells on SF [Figure 4E]. Logarithmic growth of cells on the AM and SF was observed at 48 and 72-hours after plating, respectively. No statistical difference was observed among the negative controls, suggesting the material itself did not affect MTT absorbance significantly.

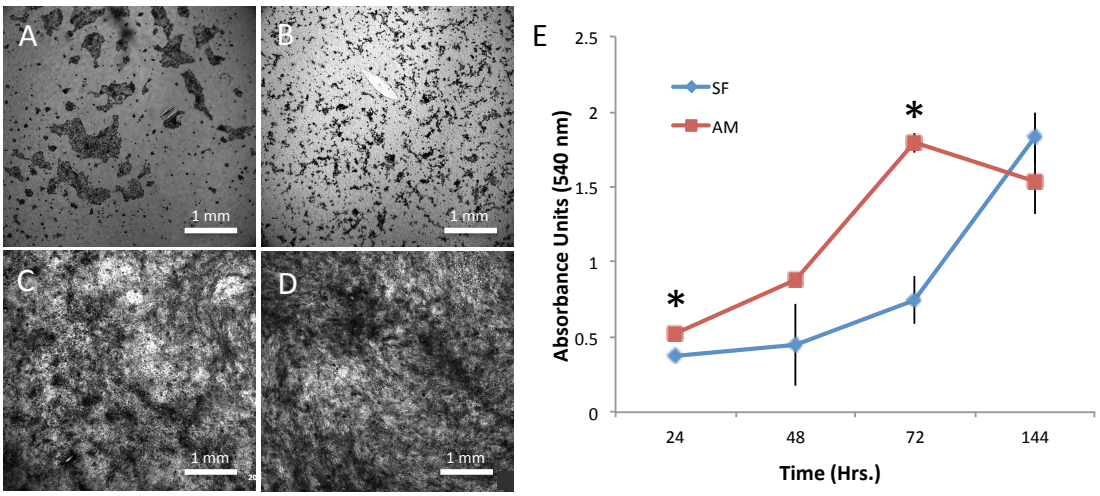


**Figure 4.** (A-D) MTT stained at day 1 and 6 in culture for HCLE cells grown on (A, C) SF and (B, D) AM). (E) At day 1 and day 3, cells cultured on AM had a statistically higher cell viability and proliferation as compared with SF ($p < .05$, $n = 4$, error bars = SD).

Immunofluorescence detection revealed that HCEC grown on SF and AM containing keratin 3/12 [Figure 5 A-D] and ΔNp63a [Figure 5 F-I] positive cells indicating that there were a mixture of cell populations undergoing variable degrees of differentiation. There were slight changes of protein expression between P1 and P2 cells on the same substrate [Figure 5 E and J], reflecting the dynamics of cell proliferation and differentiation. However, no significant difference was found between SF and AM for the two markers.

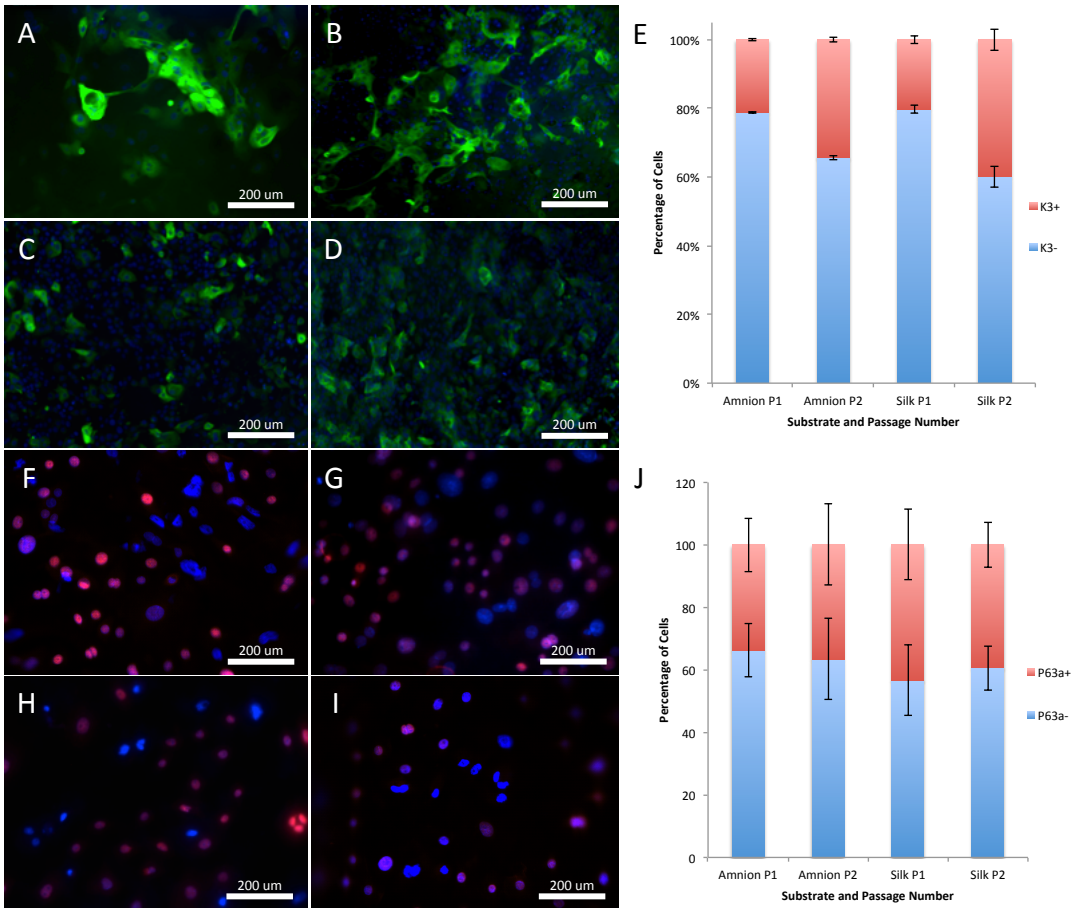


**Figure 5.** Immunofluorescent staining of RCECs cultured on (A, B) silk film and (C, D) amniotic membrane. Primary corneal epithelial cells underwent differentiation with subsequent passaging from (A, C) P1 and (B, D) P2 as demonstrated by CK3 expression (green). Immunofluorescent staining of RCECs cultured on (F, G) silk film and (H, I) amniotic membrane. Primary corneal epithelial cells underwent differentiation with subsequent passaging from (F, H) P1 and (G, I) P2 as demonstrated by p63a expression (red). Percentage HCLE expression of (E) K3 and (J) P63a proteins for cells grown on both amnion and silk substrates at passage 1 and 2 in culture.

Stratified RCEC actin and nuclear structures were imaged on the both SF and AM substrates using spinning-disk confocal microscopy, and then reconstructed z-stacks were deconvolved to provide cross-sectional images of the stratified cells. The fluorescent images provided a 3D histological image of the multi-layer stratified epithelial cell sheet structure, and represents the first known fluorescent images of their kind viewing epithelial stratification on silk film substrates [Figure 6]. Both substrates can support 2-3 layers of RCECs stratified and differentiated within 1-week of air-liquid interface culture. No significant stratified pattern was detected between cell sheets on SF and denuded AM. In addition, the natural autofluorescent signature exhibited by the silk film could be imaged, and demonstrated that the stratified cultures were well adhered to the substrate surface.

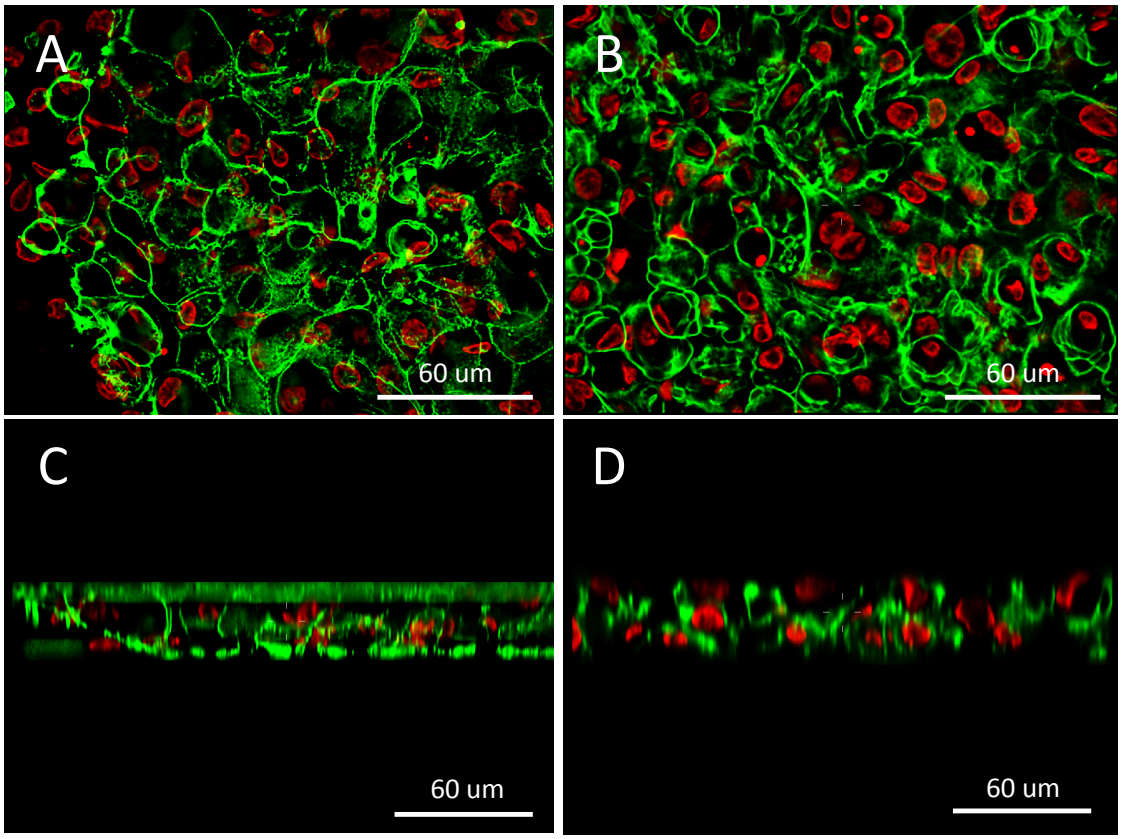


**Figure 6.** Fluorescent confocal microscopy images of RCEC stratified on (A, D) silk film and (B, D) amniotic membrane in both (A, B) en face and (C, D) cross-sectional views (red = nucleus; green = actin).

## 5. Discussion

In this study, SF films cast from *Bombyx mori* silkworm proteins were evaluated as a substrate for cell sheet generation and compared with the current clinical standard, denuded AM. Our results demonstrated that SF supports the growth of both primary and immortalized corneal epithelial cells. Cells grown on SF maintained corneal epithelial morphology, proliferative ability, and normal cell differentiation. Stratified epithelial cell sheets were

generated on SF with similar structure as cultures on denuded AM. Our study confirmed that SF could serve as a promising alternative to AM for corneal regeneration and tissue engineering applications.

Increased investigation of novel biomaterials for regenerative medicine and tissue engineering in ophthalmology is required to enhance the physicians ability to address clinical problems not currently served by the current state of the art in biomaterial technology. Specifically, when referring to corneal regeneration an ideal scaffold should have the following properties: (1) biocompatible material with non-toxic degradation byproducts; (2) free from disease transmission; (3) suitable for promoting cell growth and native tissue development; (4) transparent; (5) suitable mechanical properties; (6) modifiable for tissue growth in three dimensions; (7) modifiable shape and size to fit the corneal curvature or tissue defect; (8) available as a sterile product without compromising material properties; and (9) possesses potential for the combination with a drug or gene delivery application.

Currently, human AM is the standard substrate for ex vivo expansion of corneal epithelial cells for transplantation and clinical applications in ocular surface reconstruction. AM has been used as a temporary bandage or a permanent basement membrane due to inherent anti-inflammatory, anti-angiogenic, and anti-scarring properties (71,141). Although AM meets the criteria of (1), (2), (7) and (8) above, the material has many limitations. AM has relatively poor mechanical properties as it may tear during clinical procedure

due to material fragility (142). AM also has the tendency of curling and wrinkling when lifted with forceps or even tear if it is not properly procured, which creates difficulty in handling and transferring the material during a clinical procedure. There is also the inclination of premature material melting or dissolution in eyes due to extensive proteolytic activity with cases of severe inflammation (143,144). In addition, early detachment of the AM from the surgical site is problematic, along with the materials inherent opacity that may interfere with the patient's vision. There is also the potential risk of disease transmission and AM is required to be screened for potential infectious diseases such as HIV, hepatitis B and syphilis before implantation.

To circumvent these drawbacks, exploration of novel biomaterials is underway with promising progress. SF purified from *Bombyx mori* silk worm cocoons has been shown to be biocompatible and elicit a minimal inflammation response upon implantation (34). The use of SF has been most intensely investigated in the fields of bone (139,145,146), cartilage (20,147) and connective tissue engineering (13,148).

In this study, corneal epithelial cells were found to adhere to SF film and proliferate after plating without any detectable morphological difference when compared to denuded AM. No cytotoxic response or inhibition of cell growth was observed in the SF cultures, which indicates high biocompatibility of SF biomaterial to corneal epithelial cells. SF possesses reasonable tensile strength and was easy to handle and transfer. In addition, it is highly

transparent and may be better suited for vision restoration than semi-transparent AM. SF was easily sterilized using heat treatment and then stored at room temperature, which is also advantageous over the temperature sensitive AM that cannot be as easily sterilized and must be stored at -80°C.

Cell proliferation of RCECs on SF showed a delayed entry into growth phase when compared with AM, which may be due to the enhancement of cell proliferation through inherent growth factors known to be naturally present (i.e. EGF and keratocyte growth factor) (71,149). In addition, previous studies have shown up to a 6-fold increase in the number of attached cells on denuded AM compared with SF film and tissue culture plates, indicating the superiority of AM in promoting cell adherence and proliferation (128). This may be due to the naturally occuring structural proteins such as laminin and type VII collagen of the AM basement membrane, which may promote enhanced cell adhesion (71,150).

Corneal epithelial cells retained the normal phenotype and differentiation properties when cultured on SF films as demonstrated by the progenitor cell marker ΔNp63a (151) and differentiation marker keratin 3/12 expression (152). No statistical change in protein expression pattern was observed when cells on SF were passaged after reaching confluence. Although it has been reported that denuded AM can facilitate corneal epithelial cell differentiation compared with intact AM (153,154), the percentage of ΔNp63a positive cells in both 1$^{st}$ and 2$^{nd}$ and passage cultures were comparable in this study. When

compared between SF and AM, the status of cell differentiation was parallel with no significant difference.

Stratified corneal epithelial cells sheets were successfully constructed on both SF and AM when cultured at an air-liquid interface for 1 week. The structure of cell sheets on two substrates was similar with compact columnar cells on the basal layer with more squamous cells present on the apical layer. However, constructs on AM generally displayed more stratified layers (3-4 layers vs. 2-3 layers on SF), which was consistent with what had been previously observed (128). However, robust stratification of rabbit corneal epithelial cells on fibroin was observed using porous silk film coated chambers and a 3T3 feeder cell layer (155).

In this study the finer cytoskeletal architecture of the stratified epithelium was revealed through the use of fluorescent microscopy and image processing software. This method proved useful in producing cross-sectional images that could provide greater insight in cellular components than what standard histology techniques will allow. In addition, the natural autofluorescent signature of the silk film allows for basal layer visualization allows one to image cell attachment to the substrate surface. Future studies will continue utilizing such imaging techniques to better observe cell structure localized expression within the cell and at the attachment surface.

## 6. Conclusion

The feasibility of using *Bombyx mori* silk fibroin films as a substrate to support human and rabbit corneal epithelial cell proliferation, differentiation and stratification was demonstrated. Further investigations into various modification of silk film surface are underway to better understand how such alterations may affect cellular orientation, cell adherence, differentiation, and enhance soluble factor release or gene delivery for a given cell culture. Such insights will continue to lead to new understanding with the expectation of enhancing the ability to translate these naturally regenerative materials into clinical medicine.

CHAPTER 5

# In Vivo Assessment of Silk Film Placement on the Corneal Surface after Rabbit Corneal Epithelial Debridement

## 1. Summary

A series of studies were undertaken to assess the use of silk film upon the ocular surface in vivo. The use of silk films on the ocular surface provides unique challenges and opportunities in material properties to garner enhanced healing after injury. The physical design of the silk bandage was successfully optimized through the production of a curved body shape to enable better application and comfort to the cornea. Silk films dissolution rate was varied through the use of water-anneal processing. A rabbit corneal injury model was utilized to assess the impact of the silk biomaterial properties after corneal injury. The silk film bandage was shown to enhance corneal healing upon rabbit animal models when material dissolution was less than 24-hours. However, if material dissolution was greater than 24-hours there was a negative impact on corneal healing. In conclusion, a silk film bandage can be optimized to promote healing after corneal injury.

## 2. Introduction

Each year 2.5-million people in the United States (US) receive traumatic injuries to their eye (58). A wounded eye can cause extreme pain, swelling,

blurred vision, and even vision loss. Approximately 60,000 patients are diagnosed with trauma-related blindness each year, and 40% of all cases of blindness are caused by trauma (58,60). It is the single most important ocular environmental health problem in the US today, and in the rest of the world about 50 million eye injuries occur annually and severe injuries are a major problem in developing countries (58). Eye wounds are not limited to trauma and 11-million Americans experience ocular surface disorders each year, such as corneal ulcers, erosion, degeneration, and perforation (60,72). Many of these disorders lead to ocular surface wounds and need to be repaired through various therapies or surgical procedures. In addition, procedures such as retinal vitrectomy, photorefractive surgery, and cataract removal account for millions of additional patients left with sustained surgical wounds that are left to heal on their own (156,157).

Clinicians are limited in most cases to treatment options that only protect the eye from further injury, which then allows the body to heal on its own (60). For years researchers have pursued regenerative technologies, such as stem cells therapies and the use of amniotic membrane, in the hopes of regenerating damaged ocular tissue (158-160). However, such treatments can have varying effectiveness, may be costly to perform, and not easily accessible thus limiting its use to the most extreme diseases and injuries (72,75,141). In addition, the use of donor tissue like amniotic membrane has inherent risk for disease transmission (141), while stem cell transplantation

requires a tissue biopsy that requires injury to another eye (132). Therefore, alternative regenerative approaches are needed for greater accessibility of clinical care without increasing patient risk of disease or further injury from biopsy.

Silk proteins offer a potential alternative material to current regenerative approaches due to their high degree of biocompatibility, transparency, inability to spread infectious disease, and tunable material properties that enable their use for a wide range of biomedical applications (6,7,25). Current work has demonstrated initial evidence for using silk films in corneal tissue engineering and in ocular surface repair (21,22,54). Silk films have been found to support corneal cell growth, and able to develop stratified epithelial cell sheets equivalent to amniotic membrane substrates (22). However, limited work has been carried out in vivo to assess their capability for use in a clinical capacity. The study below illustrates for the first time a curved silk film bandage design that conforms to the shape of the eye, and that can have a tunable material dissolution rate to enhance corneal healing after injury. These initial studies demonstrate that silk films may be designed for use in ocular surface repair, and offer a platform for future development for clinical translation.

## 3. Materials and Methods

### 3.1. Production of Silk Solution

*Bombyx mori* silkworm cocoons (Tajima Shoji Co., Yokohama, Japan) were

cut into thirds and then boiled for 40-minutes in 0.02M $Na_2CO_3$ (Sigma-Aldrich) to extract the glue-like sericin proteins from the structural fibroin proteins as previously described (21). The fibroin extract was then rinsed three times in $dH_2O$ for 20-minutes per wash then dried overnight. The rinsed fibroin extract was then dissolved in 9.3M LiBr solution at room temperature, and placed covered within a 60°C oven for 4-hours. The solution was dialyzed in water for 48-hours (MWCO 3,500, Pierce, Inc.). The dialyzed silk solution was centrifuged twice at 13,000-g, and the supernatant collected and stored at 4°C. The final concentration of aqueous silk solution was 8 wt./vol.%, as determined by gravimetric analysis.

### 3.2. Preparation of PDMS Casting Surfaces

Flat polydimethylsiloxane (PDMS) substrates of 0.5 to 1.0-mm thickness were produced by pouring 5-mL of a 1:10 casting catalyst/potting solution (Momentive, Inc., Albany, NY) onto a plastic 90-mm petri dish surface. The cast PDMS solution was then degassed for 2-hours under vacuum, and then cured in an oven at 60°C overnight. The following day the cured PDMS was removed from the silicon substrate and then punched to form round 14-mm circles. The PDMS substrates were placed cast side up and dust/debris was removed by using clear tape. The surfaces were further cleaned with a 70% ethanol, three $dH_2O$ rinses, and then allowed to air dry in a clean environment.

### 3.3. Silk Film Casting and Sterilization

Silk films measuring 80-μms in thickness were created by casting 200-uL of 8% silk fibroin solution cast upon the round PDMS surface. After casting the silk solution, films were covered and allowed to dry for 24-hours to form the patterned silk film surface. Silk film samples were then water-annealed (WA) at different time points by placing the samples in water filled chambers at a 10-psi vacuum and 85% relative humidity (RH). Three sets of samples were evaluated that were annealed for 0, 20, or 40-minutes to produce varying degrees of silk solubility. This process induces ß-sheet protein secondary structure formation that produces a greater hydrophobic material with continued processing time (32,40).

### 3.4. In Vitro Silk Film Dissolution Testing and Optical Coherence Tomography (OCT) Imaging of Initial Silk Film Adhesion In Vivo

Qualitative assessment of silk film dissolution was carried out by placing samples that were WA processed for 0, 20, 40, and 240-minutes respectively into 4-mL of $dH_2O$ for 15-mintues. Images of silk film dissolution were taken on a stereomicroscope (SteREO Lumar.V12, Carl Zeiss Microscopy, Germany) to assess material solubility. In addition, the Bradford protein content assay was performed to quantitatively assess silk dissolution. Briefly, silk films from each processing time sample group (n = 3) were placed into individual QIAshredders (Quiagen, Valencia, CA). The centrifugal port of the

QIAshredder was covered with parafilm to prevent premature solution flow through, and 500-µL of $dH_2O$ was added to the QIAshredder to begin silk dissolution. The silk films were then mixed for 15-minutes, the parafilm stoppers removed, and then centrifuged. A 1:10 dilution of silk supernatant was prepared, and a 1:5 dilution of Bradford stock reagent (BioRad, Hercules, CA) was prepared. The assay was ran by preparing a 1:20 dilution of sample to reagent dilution in a 96-well plate, and absorbance was read at 595-nm. Initial attachment of unprocessed silk films to the corneal surface was observed using OCT imaging of the silk film attaching to an uninjured corneal surface, and then monitored over time with a Bioptigen SDOIS system (Research Triangle Park, NC). Before applying the silk film the rabbit's eye was treated with the topical anesthetic proparacaine.

### 3.5. Histology

Excised rabbit corneas were prepared for hemotoxylin and eosin (H&E) staining. Samples were paraffinized, and then sectioned into 7-µm thick slices. The sections were deparaffinized with two changes of Histoclear solution (National Diagnostics, Atlanta, GA), and then serial rehydrated in serial ethanol dilutions. Samples were stained in hemotoxylin and differentiated in 1% acid alcohol, and then blued in 0.2% ammonia water. Samples were counterstained in eosin solution, serially dehydrate with Ethanol dilutions, and mounted with DPX mounting medium.

### 3.6. In Vivo Injury Model and Analysis

Animals were handled according to the ARVO Statement for the Use of Animals in Ophthalmic and Visual Research, under protocols approved by the Institutional Animal Care and Use Committee at the Weill Cornell Medical College. After anesthetizing the rabbit with a ketamine/xylazine solution topical proparacaine anesthetic was applied to the eye, and a speculum was placed to maintain the eyelids open. A trephine 8-mm in diameter was used to demarcate the cornea. Epithelial debridement was performed within the marked area with a #15 surgical blade. A silk film was then applied to the corneal surface and allowed to self-adhere, or no film was applied for untreated controls. A drop of topical moxifloxacin antibiotic was applied to the eye, and rabbits closely monitored for evidence of distress or infection. The wound healing of the rabbits was monitored and examined using a slit lamp microscope. The corneal wounds were then measured using a 1-mg/mL concentration of fluorescein dye (Sigma, Inc.) at 24, 48, and 72-hour time points. Fluorescein staining indicates a deepithelized surface as denoted by green fluorescence under blue light. The data was statistically analyzed using the Student t-test.

## 4. Results

### 4.1. Silk Film Production and Self-Adhesion Characterization

Silk films were successfully created that dissolved to varying degrees in water

as a result of WA processing time [Figure 1A-D]. Unprocessed silk films had near complete dissolution in water [Figure 1A], while there was reduced dissolution for samples WA for 20-minutes where non-dissolved portions of the film remained translucent [Figure 1B]. It was shown that the edge of the silk films tended to dissolve to less of a degree than the central regions. Silk films WA for 40-minutes and above appeared to show limited dissolution in water and maintained transparency [Figure 1C-D]. Protein assay results conferred qualitative results indicating that protein dissolution was reduced on average with increased WA processing time [Figure 1E].

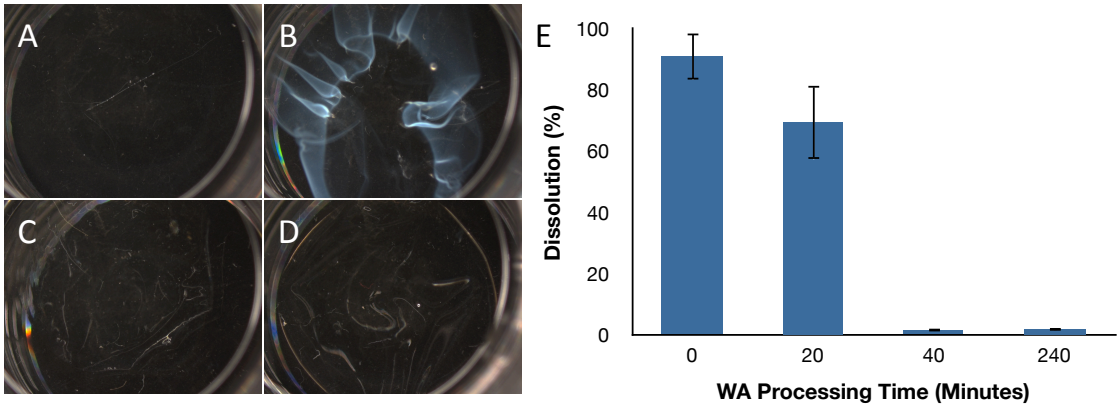


**Figure 1.** (A-D) Silk film dissolution after incubation in water for a 15-minute period reduced with increasing WA processing time at (A) 0, (B) 20, (C) 40, and (D) 240-mintues. (A) Films appeared to completely dissolve without WA processing, (B) partially dissolve after 20-minutes of processing, and appeared insoluble after (C) 40-minutes and above. (E) Protein assay results confirmed qualitative assessment that the extent of silk film dissolution in water reduced with WA processing time (n = 3, error bars = SD).

Silk films proved to be highly transparent after WA processing as previously demonstrated [Figure 2A] (25). It was found that the films could self-adhere to the cornea after both processing time points, and allowed for a non-invasive and straightforward application method of the silk film to the ocular surface. It was demonstrated that the flat silk films would readily smooth over the rabbit corneal surface as it hydrated as monitored by slit lamp photography [Figure 2B-C]. As the film hydrated it began to turn into a gelatinous consistency as the material began to dissolve. This gelatinous material remained adhered to the cornea surface.

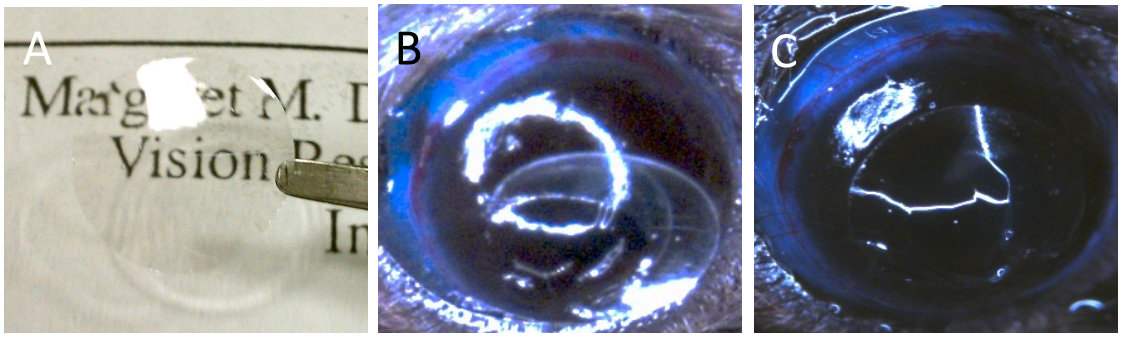


**Figure 2.** (A) The silk film bandage is transparent and administered using forceps, (B) applied directly to the cornea, and (C) then readily adheres as it hydrates.

Time-lapse OCT images were taken of the untreated silk film's adhesion response to the uninjured rabbit cornea [Figure 3A]. Upon initial application the film produced standing wave morphology with peaks in thickness ranging from 79 to 114-µm in thickness [Figure 3B]. After 1-minute

post-application the silk film thickness had evened out to around 100-um, which corresponded to a 25% increase in thickness [Figure 3C]. Over a 3-minute time period the silk film increased up to 136-µm in thickness, which corresponded to a 70% increase in silk film thickness post-application [Figure 3D-E]. The thickness of the film then began to decrease as the material began to dissolve after 4-minutes post application [Figure 3F]. After 10-minutes post-application the silk film thickness had reduced to around 100-µm in thickness, and the edge regions appeared to maintain both consistent thickness and attachment to the corneal surface [Figure 3G]. After a total of 45-minutes upon the eye portions of the silk film remained non-dissolved and silk film particulates were spread over the cornea in various regions [Figure 3H]. The rabbit cornea appeared unaffected by the presence of the material, and the animal showed no signs of discomfort or subsequent inflammation after the silk film's application.

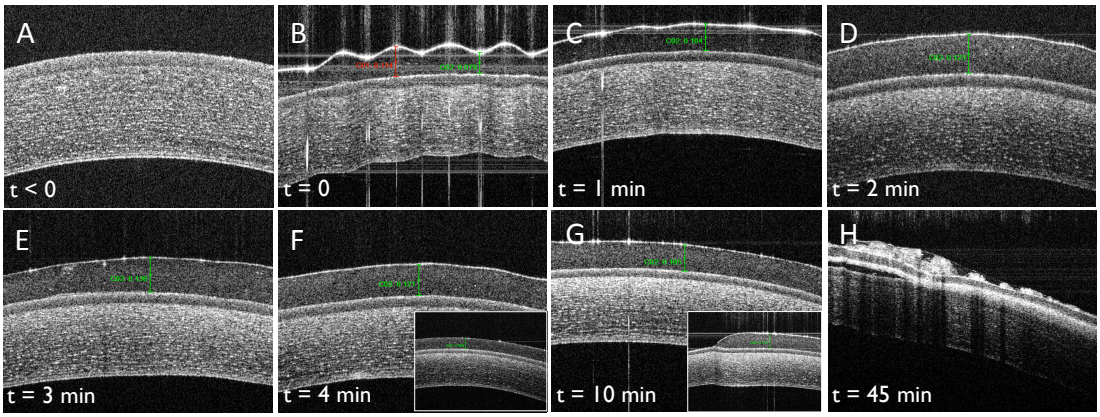


**Figure 3.** Silk film initial adhesion to the (A) cornea was evaluated over time with OCT imaging from (B-F) 0 to 4-minutes, (G) 10-minutes, and (H) 45-minutes respectively. (B) The silk film was found to form a standing wave morphology upon initial adhesion, (C-E) then swelled as the material hydrated. (F-G) This was followed by a period of material dissolution as the film reduced in thickness. (G) The film edge showed uniform thickness and remained well adhered to the corneal surface after 10-minutes post application. (H) Insoluble portions of the silk film were measured at 45-minutes showing the remaining silk particulates.

### 4.2. In Vivo Healing Post Epithelial Debridement

Three sets of animal trials were performed for silk films that were WA processed for 0, 20, and 40-minutes respectively to assess the impact of the material presence on corneal healing. Unprocessed silk films dissolved on the ocular surface within 5-minutes post-application [Figure 4A], and demonstrated no effect on healing when compared to the untreated control group [Figure 4B-C]. No silk remained after 1-hour post-application as revealed by the visual inspection of the rabbit within the cage.

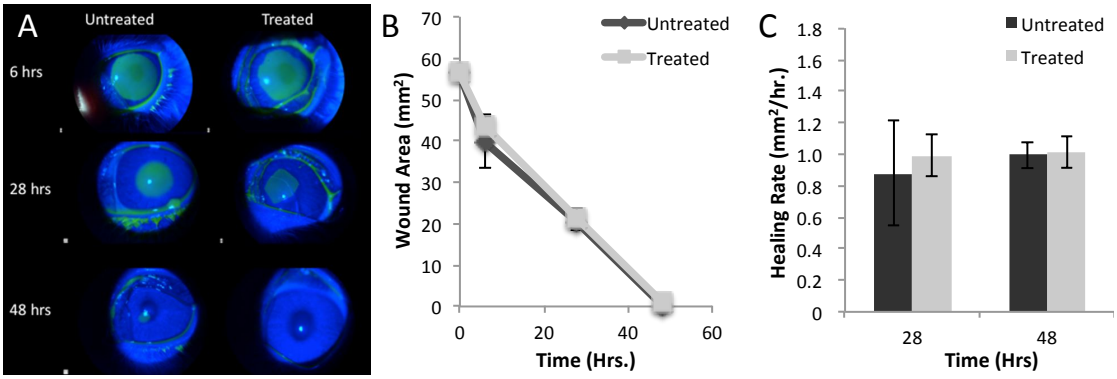


**Figure 4.** (A) Fluorescein staining images of rabbit corneal healing progression for treated and untreated rabbits over a 48-hour period. (B) Wound area size and (C) healing rate were similar between silk film treated and untreated animals (n = 3, error bars = SD).

The presence of the silk film did not adversely affect the overall corneal epithelium healing after 7-days post-surgery as revealed by H&E staining [Figure 5]. Corneas from both untreated and treated groups demonstrated a completely healed epithelial layer, reformation of the basement membrane, and an absence of inflammatory cells. The corneal stroma region appeared unaffected, with the absence of any neovascularization or inflammatory cells. In addition, no remnants of the silk film were observed in the histology samples.

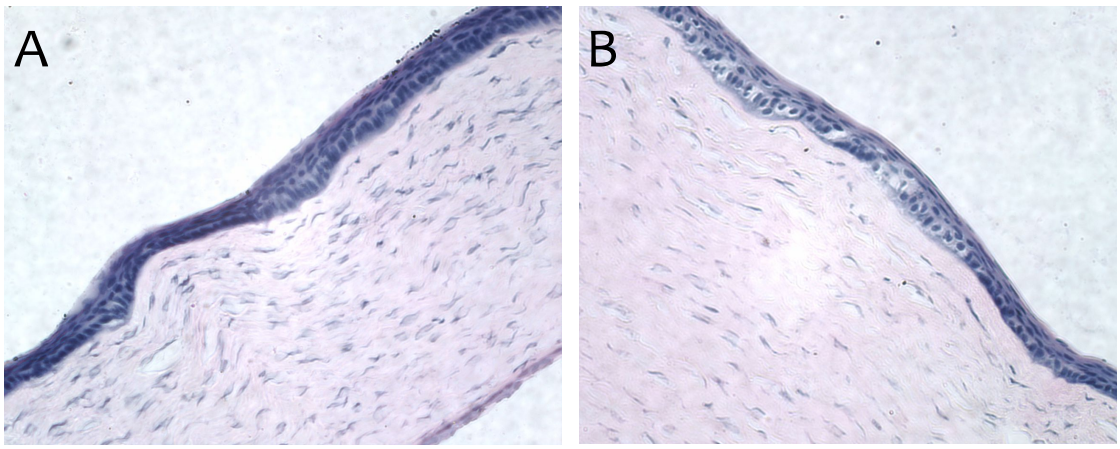


**Figure 5.** Histological examination of rabbit corneas 7-days after epithelial debridement for (A) untreated and (B) treated animals. The presence of the silk film material did not negatively impact the cornea stroma architecture or the reepithelialization process. Silk film remnants were not found in the tissue sectioning.

Silk films that were water annealed for 20-minutes were than applied onto the debrided epithelium [Figure 6A]. The silk film material was found to reside on the ocular surface for up to 10-hours post-procedure. In addition, the silk film treated group demonstrated a significant increase (30%, $n = 3$, $p < 0.05$) in healing rate over the first 24-hour period, while the film was still present on the wound bed when compared to untreated controls [Figure 6B-C]. After 48-hours the silk film was no longer present on the corneal surface, and it was shown that the healing rate was similar to untreated controls.

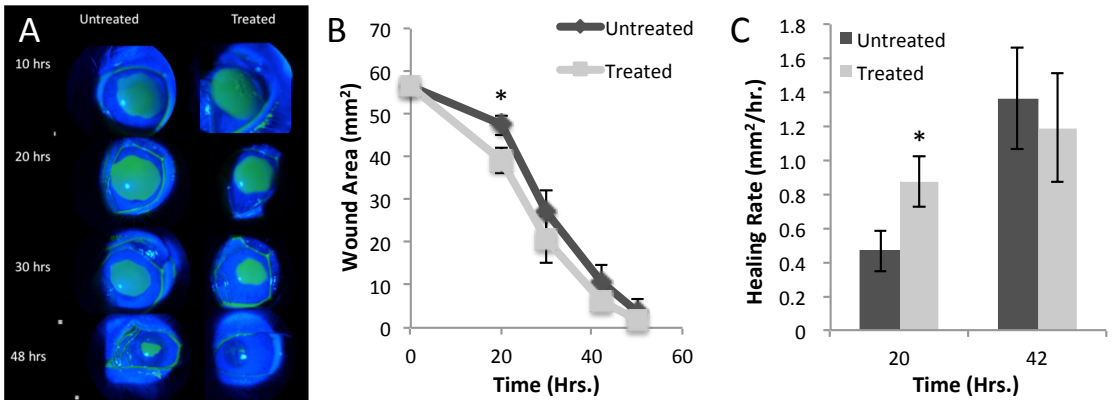


**Figure 6.** (A) Time course images of fluorescein stained epithelial debridement area for untreated and silk film treated rabbit groups. (B) Wound healing profiles demonstrated a significant reduction in wound size for treated animals over a 42-hour period post-procedure. (C) A statistically significant increase in healing rate was demonstrated over the first 20-hours post-procedure for treated animals when compared to untreated controls. (* indicates $p < 0.05$ compared to untreated controls, n=3, error bars = SD)

Silk films that were water annealed for 40-minutes were than applied onto the debrided epithelium [Figure 7A]. Films were still present on the corneal surface 48-hours post-procedure, at which point they were removed with forceps. Non-dissolved films were found to negatively impact healing rate when compared to untreated controls [Figure 7B]. This was also seen as a statistically significant decrease in healing rate for silk treated animals after 48-hours post-application [Figure 7C]. These results indicated that the presence of non-dissolving silk films was causing adverse effects on corneal healing.

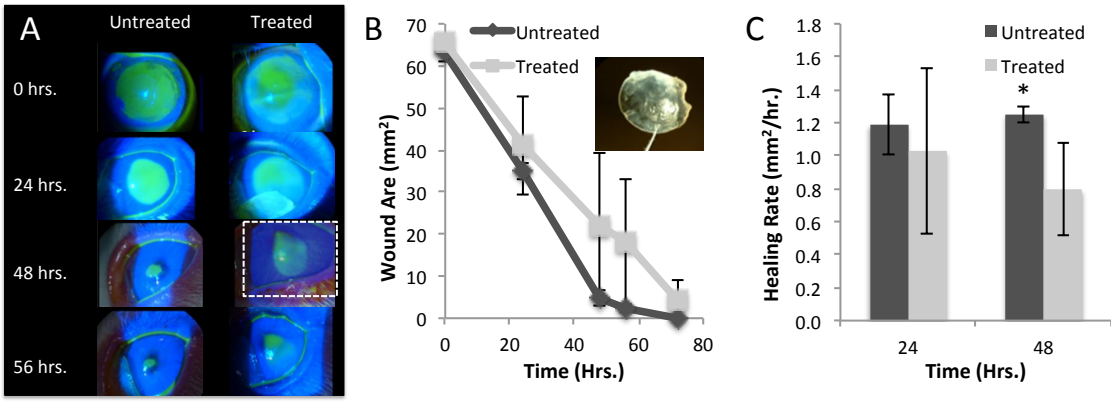


**Figure 7.** (A) Time course images of fluorescein stained epithelial debridement area for untreated and silk film treated rabbit groups, where the film was removed at the 48-hour post-surgery time point as indicated by the white box. (B) The wound healing profile demonstrated an increase in average wound size over time for treated animals over a 48-hour period post-procedure when the silk film was removed as shown as an image inset. (C) A statistically significant increase in healing rate was demonstrated for untreated controls at the 48-hour time point as compared to silk film treated animals (* indicates $p < 0.05$ compared to untreated controls, n=3, error bars = SD).

## 5. Discussion

Silk films offer a potential material for use in ocular surface reconstruction (22). This is primarily due their transparent nature, high degree of biocompatibility, and the ability to control material properties such as dissolution and degradation rates (6,25,32). The silk film dissolution rate was changed by altering the material's hydrophobicity through the formation of α-helix and β-sheet protein secondary structures by using the WA process (32,40,52). As a result silk films were produced for application to the rabbit cornea, and were

found to be transparent and possess varying dissolution rates in water.

In addition to changing material dissolution, the silk films were made to self-adhere to a given surface. This material property has been thought to be due to increased surface tension as a result from the material hydrating, and as a result the silk film turns into a gelatinous material that remains adhered to a given surface (35,52). This adhesive property was utilized to allow for a straightforward method to attach the silk film to the rabbit cornea surface. The mechanism of silk film attachment, hydration, and dissolution was observed using OCT imaging. Results indicated that the silk film uniformly attached to the cornea surface, and produced a wave-like morphology during the initial hydration process. After 2-minutes post-application the silk film began to hydrate and readily smoothed into an even thickness while remaining adhered to the cornea surface. This was followed by a subsequent uniform expansion of the material thickness as the silk film continued to swell from hydration. This process was rapid as the film reached its maximum thickness within a few minutes after application. The silk film appeared to both swell and simultaneously begin to dissolve, which was seen as a reduction in silk film thickness around 5-minutes after application. It was noticed that film dissolution was much less rapid, and it was seen that insoluble particulates remained on the eye after 45-minutes post-procedure. These results demonstrated that a self-adhering silk film could be designed to maintain residency on the cornea, while remaining attached to the epithelial surface.

The dissolution rate of the silk film appears to be an important factor in regards to the overall in vivo response. Rabbit animal trials demonstrated that silk films could be used to enhance reepithelialization after surgery by 30% if the material retained a limited period of residence time over the corneal injury site. This optimal residence time is thought to be somewhere between 10 to 24-hours post-application as taken from fluorescein staining. It was apparent that silk film designed to dissolve within an hour after application had a negligible effect on healing after 24-hours post-procedure. Histology revealed that the presence of the silk protein material did not impart a negative effect on the cornea post-application. However, if the residence time of the silk film on the injury site was too extensive this appeared to inhibit healing. This inhibition appeared to be a result of mechanical scraping that the insoluble silk film may have imparted on the healing epithelium. These results illustrate that there is an optimal silk film residence time to promote corneal healing after injury.

More work is needed to better understand the optimal silk protein secondary structure content that must be obtained to promote optimal healing. Furthermore, it is still unclear as to why the silk film promotes enhanced healing. This effect may be a simple result of mechanically covering the wound site or may be more chemical in nature as silk is known to be highly non-inflammatory (6,7). In summary, the animal results illustrate how silk films can be engineered for use in ocular surface repair.

## 6. Conclusion

Transparent and highly biocompatible silk films are promising biomaterials choices for clinical use in the area of ocular surface repair. Silk films were developed to self-adhere to the cornea surface and dissolve at varying rates. These various silk films were applied in vivo upon the rabbit cornea with debrided epithelial surfaces. Results demonstrated a lack of material toxicity and enhanced healing rates for films with residence times under 24-hours. These initial results indicate that silk films may be further optimized for use in ocular surface repair to enhance wound healing after accidental or surgical injury.

CHAPTER 6

# Human Corneal Limbal-Epithelial Cell Response to Varying Silk Film Topography Geometry *In Vitro*

## 1. Summary

Silk fibroin films are a promising class of biomaterials that have a number of advantages for use in ophthalmic applications due to their transparent nature, mechanical properties and minimal inflammatory response upon implantation. Freestanding silk films with parallel line and concentric ring topographies were generated for in vitro characterization of human corneal limbal-epithelial (HCLE) cell response upon differing geometric patterned surfaces. Results indicated that silk film topography significantly affected initial HCLE culture substrate attachment, cellular alignment, cell-tocell contact formation, actin cytoskeleton alignment, and focal adhesion (FA) localization. Most notably, parallel line patterned surfaces displayed a 33%-54% increase on average in initial cell attachment, which corresponded to an over 2-fold increase in FA localization when compared to other silk film surfaces and controls. In addition, distinct localization of FA formation was observed along the edges for all patterned silk film topographies. In conclusion, silk film feature topography appears to help direct corneal epithelial cell response and cytoskeleton development, especially in regards to FA distribution, in vitro.

## 2. Introduction

Silk proteins have evolved as the arthropod's material for producing external structures over the last 380-million years (1), and produce the world's strongest natural fibers once extruded from the insect's body (3). Silk fibers are commonly associated with textile manufacturing and use as a medical suture, however recently a silk biopolymer solution derived from these fibers has been used to form a wide range of materials forms, such as films, sponges, hydrogels, and solid blocks (4). In this regard, silk may be considered an engineering grade biopolymer in which the formed material properties may be modulated primarily through the induction of protein secondary structure formation (i.e. alpha-helices and beta-sheets) and by controlling water content through a variety of processes (26,37,161). One of the primary uses of regenerated silk materials is in the production of scaffolding material in the fields of tissue engineering and regenerative medicine due to their inherent biocompatibility (6,162). Specifically, silk films offer a wide platform for biomaterial innovation due to their highly controlled material properties, ease of fabrication, biocompatible nature, and potential for chemical modification (9,25,47,48). One interesting material property of silk films is their ability to produce topographic features on the micro and nanometer scale, which allows for the formation of surface patterned culture surfaces for cell growth (21,25,83). Topographic contact guidance of cells by surface topography can have dramatic effects upon cellular development,

extracellular matrix (ECM) alignment and formation, cell proliferation, cellular adhesion, and proliferation and apoptosis (21,81,83,163). In this way silk film substrates offer an elegant system to produce customized patterned surfaces that can be designed to promote a desired cellular response with potential to elicit a clinically desirable effect (48).

Silk films are currently being developed for use in ophthalmology for use in the cornea due to their transparent nature and biomaterial properties (21,21,22,54). Recent work has focused on developing silk films for use in ocular surface repair and corneal tissue engineering applications (22,40,54). The role of surface topography influencing corneal epithelial response is a subject of interest due to the potential ramifications in expediting the wound healing process post injury. Engineered surfaces can be designed to enhance corneal epithelial adhesion, migration, proliferation, extracellular matrix (ECM) production, and cellular alignment which are all important aspects in the wound healing response (80,121,122,164,165). However, these studies have been performed upon material surfaces not suitable for *in vivo* implantation (i.e. silicon and plastic) and future *in situ* tissue integration and regeneration. Therefore, silk films offer the potential to optimize the material *in vitro* with the added potential benefit for *in vivo* translation.

It would be advantageous to produce a silk film topography that has been engineered to enhance the corneal epithelial healing response. However, limited studies have been performed to date that characterize corneal

epithelial response upon such patterned silk substrates. The goal of the present study is to characterize the relationship between silk film topography and corneal epithelial cell response. In the present work silk films with varying surface topography feature geometries (i.e. parallel lines and concentric circles) were produced using standard photolithography, ion-etching, and soft-lithographic techniques to produce cell culture substrates (166-168). The surface topographies produced for this study were designed to allow for a controlled *in vitro* comparison of various cellular responses such as cell morphology, cell attachment, culture growth, and cytoskeletal localization and distribution over time in culture.

## 3. Materials and Methods

### 3.1. Production of Silk Solution

*Bombyx mori* silkworm cocoons (Tajima Shoji Co., Yokohama, Japan) were cut into thirds and then boiled for 40-minutes in 0.02M $Na_2CO_3$ (Sigma-Aldrich) to extract the glue-like sericin proteins from the structural fibroin proteins as previously described (21,169). The fibroin extract was then rinsed three times in $dH_2O$ for 20 minutes per wash. The rinsed fibroin extract was then dissolved in 9.3M LiBr solution at room temperature, and placed covered within a 60°C oven for 4-hours. The solution was dialyzed in water for 48-hours (MWCO 3,500, Pierce, Inc.). The dialyzed silk solution was centrifuged twice at 13,000-g, and the supernatant collected and stored at 4°C. The final concentration of

aqueous silk solution was 8 wt./vol.%, as determined by gravimetric analysis.

### 3.2. Patterned Silicon Wafer Production

Silicon wafers possessing either parallel line or concentric ring topographies were prepared using standard photolithographic and ion etching techniques. The specific topographies were selected to compare how geometric shape, such as line and circular patterns, affect cell response both initially and at later culture time points. The features composing the various geometric surface topographies possessed dimensions measuring a 2-um width, 4-um pitch, and 1.5-um depth. Width and pitch measurements were chosen based on previous literature that demonstrated this dimension produced a contact guidance effect upon corneal epithelium, which modulated various cellular characteristics such as alignment and adhesion (40,80,104,121,122). The 1.5-um depth was chosen based on previously cited experiments that indicated this depth appears to have a negligible effect on cellular function (25,123). As a result the selected dimensions allow for the controlled comparison of cellular response upon various geometric surface topographies without adding potential variables from feature width, pitch, or depth. A 21-die array in a [3:5:5:5:3] design was fabricated upon a 100-mm silicon wafer. Individual dies have a 10-mm diameter separated by 5-mm spacing. Feature dimensions were verified using scanning electron microscopy (SEM).

Photolithography mask patterns were designed using L-edit software

(Tanner EDA, Inc.) and then imported into a DWL66 laser pattern generator and direct write machine (Heidelberg Instruments, Heidelberg, Germany) for production onto a photoresist coated glass substrate. The finished mask was then placed within an Autostep 200 DSW i-line wafer stepper (GCA, Inc.) for photolithographic patterning of photoresist coated 100-mm diameter silicon wafers. Wafers coated with 1-um thick layer of photoresist (Megaposit™ SPR™ 220-3.0, Dow Chemical, Inc.) were produced that possessed the 21-die wafer array. The wafers were then placed into a Unaxis 770 ion etching device (Plasma-Therm, LLC, St. Petersburg, FL) to produce 1.5-um depth etch. The above process was designed to provide repeated topographic features measuring 2-um in width, 4-um in pitch, and 1.5-um in depth over a circular surface area with a 1-cm diameter. Feature sizes were then imaged using an Ultra SEM (Zeiss, Inc.).

### 3.3. Casting Surface Preparation

Flat polydimethylsiloxane (PDMS) substrates of 0.5-1.0-mm thickness were prepared by pouring 5-mL of a 1:10 casting catalyst/PDMS (Momentive, Inc., Albany, NY) solution onto the patterned silicon wafer surfaces. The cast PDMS solution was then degassed for 2-hours under vacuum, and then cured in an oven at 60°C overnight. The following day the cured PDMS was removed from the silicon substrate and then punched to form round 14-mm circles centered on the patterned surface. The PDMS substrates were placed cast side up and

dust/debris stripped using clear tape. The surfaces were further cleaned with a 70% ethanol wash (EtOH), three distilled water ($dH_2O$) rinses, and then allowed to air dry in a clean environment. PDMS surfaces were used for multiple silk film castings. Before additional casting, the PDMS surfaces were prepared using a 9.3-M LiBr soaking step with subsequent EtOH and $dH_2O$ rinses to remove residual silk fibroin protein from the surface.

### 3.4. Silk Film Casting and Sterilization

Silk films 40-um in thickness were cast using 75-uL of 8% silk fibroin solution cast upon the round PDMS surfaces as previously described (21,21). After casting, films were covered with a venting lid and allowed to dry for 24-hours to form the patterned silk film surface. Appropriate numbers of silk films were prepared depending on the experimental setup. Silk film samples were then water-annealed (WA) by placing the samples in water filled containers (i.e. emptied plastic desiccator) in which a vacuum (10-psi) was used to produce a water-vapor saturated environment and left to sit for greater than 4-hours. This process induces ß-sheet protein secondary structure formation and produces a water-insoluble silk film for cell culture (40,170). The silk film sample surface topographies were imaged using SEM to verify surface feature dimensions.

After the WA process, silk film samples were removed from their PDMS surfaces and submerged within 70% EtOH for 15-minutes in a clean bench environment. In addition, 15-mm diameter glass cover slip control surfaces

and stainless steel O-rings (Superior Washer, Inc., Hauppauge, NY) measuring 15.4-mm in outer diameter and 11.6-mm inner diameter were submerged within 70% EtOH for the same time period. Silk film samples and glass control surfaces were then placed pattern side up into 24-well plates, and a stainless steel O-ring was placed on top to hold the film down to the culture well bottom surface. Films were then subsequently washed three times with 1-mL of sterile PBS. The silk film samples were left in the final PBS wash until ready for cell seeding.

### 3.5. HCLE Cell Preparation and Culture

A previously established immortalized human corneal-limbal epithelium (HCLE) cell line was kindly provided by Dr. Ilene Gipson (Schepens Eye Research Institute, Harvard Medical School, Boston, MA). The HCLE cultures were chosen based on the cell line's highly characterized history, and reliability when working with new substrates such as patterned silk films (21,98,164). The cells were given keratinocyte serum free medium (K-SFM), 1% 100X penicillin-streptomycin and 0.3-M $CaCl_2$. In addition, the medium was supplemented with 0.45 vol.% bovine pituitary extract (BPE), and 0.2-ng/mL of epithelial growth factor (EGF, Human recombinant). Media supplies were purchased from Invitrogen (Eugene, OR). The HCLEs were cultured until 90% confluent upon TCP, and then seeded upon the various silk films and glass topographies. A seeding density of 10,000 cells per $cm^2$ was chosen based on

the fact cultures would reach near confluency after 3-days post seeding. Culture media was changed every 48-hours post seeding.

### 3.6. Nucleic Acid Content Assay

The CyQuant NF (Invitrogen, Inc., Eugene, OR) assay was utilized to assess cellular nucleic acid content as a measure of initial cellular adhesion and culture proliferation upon the silk film and TCP surfaces. The stainless steel rings were removed from the sample wells, the sample surfaces were transferred to a new 24-well plate, and the cultures were placed into a -80°C freezer overnight following the manufacturers recommendations. HCLE cultures (n = 4) for each surface were prepared and harvested at 4-hours, 3-days, and 7-days time points post cell seeding. Standard curves were developed by seeding 10,000, 20,000, 40,000, 60,000, and 75,000 cells in a 24-well plate (n = 3), centrifuged to attach cells to well bottom surfaces, media was removed, and the plate was placed in the freezer with samples. The following day, 500-uL of prepared CyQuant solution from the supplied protocol (5% 20x lysis buffer, 94.75% sterile $dH_2O$, and 0.25% 400x CyQuant dye reagent) was added to each sample and standards. Samples were placed in a 37°C incubator for 5-minutes, shaken, and then 200-uL sample volumes were pipetted into 96-well plates. Control samples without cells were used as blank samples for silk and glass surfaces. Dye binding was measured by fluorescence with an excitation wavelength of 485-nm and an emission

wavelength of 530-nm using a SpectraMax M2 fluorimeter microplate reader (Molecular Devices, Inc., Sunnyvale, CA). Fluorescent activity was then converted to cell number using the produced standard curves ($R^2$ value = 0.99).

### 3.7. Scanning electron microscopy (SEM)

Cross-sectional silk film material samples were placed in liquid $N_2$ and cracked down the center of the film using a razor blade. Biological samples were washed with PBS and then fixed with Karnofsky's fixative (Electron Microscopy Sciences, Hatfield, PA) for 15-minutes at room temperature. Samples were processed through serial EtOH dehydration baths (50, 70, 90, and 100% EtOH) for 2-minutes per bath concentration. Samples were then further dried using hexamethyldisiloxane (HMDS, Sigma-Aldrich, Inc.) solvent to remove residual water saturation for 2-minutes (79,80,87,121,166), and then allowed to dry for 2-hours in a desiccator . After HDMS processing, samples were sputter coated with gold for 90-seconds leaving an approximate 2-nm coating on the samples. Films were then imaged using an Quanta 600 environmental chamber SEM (FEI, Inc., Hillsboro, OR).

### 3.8. Imaging and fluorescent staining

All phase contrast, differential interference contrast (DIC), and fluorescent images were taken using an Observer Z1 fluorescent microscope (Carl Zeiss,

AG) with either a 2.5x (NA 0.12 air), 10x (NA 0.45 air), or 63x (NA 1.4 oil) objective lens as indicated utilizing a 1.0 or 1.6 Optivar optic as indicated. An AxioCam single channel camera and AxioVision software (Carl Zeiss, AG) were used to capture all images as indicated.

Phase contrast images of cultures at1-day post seeding were captured using a 10x objective and 1.6 Optivar. Samples from each substrate were fixed with 4% paraformaldehyde in PBS for 15-minutes, permeabilized with 0.4% Tween-20 in PBS for 5-minutes, and blocked with 2% BSA in PBS for 30-minutes at room temperature. Anti-vinculin primary antibody (V9131, Sigma, St. Louis, MO) was incubated with cells at 1:600 dilution for 1-hour at room temperature, followed by incubation with Oregon Green 488 goat anti-mouse secondary antibody (O11033, Invitrogen, Eugene, OR) at a 1:800 dilution for 1-hour. F-actin and nuclei were then stained by incubating cells in 1:100 dilution of Alexa Fluor 568 Phalloidin (A12380, Invitrogen, Inc., Eugene, OR ), and 1:10,000 dilution of DAPI (83210, AnaSpec, San Jose, CA) for 20-minutes and 5-minutes, respectively while protected from light. After rinsing using PBS, samples were mounted, and protected with a glass cover slip.

### 3.9. Image Analysis and Processing

Particle analysis of nuclei density upon various culture surfaces was performed by collecting a 7x6 array of fluorescent images of DAPI stained samples (n = 4) using a 2.5x objective and MosaiX software equipped on the

AxioVision software package. Images were then opened in ImageJ software (NIH), converted into 8-bit format, the threshold was set within 5% of the right signal distribution curve to eliminate background, and then particles were counted using the 'Analyze Particle' tool.

For cell spreading measurements the10x objective and MosaiX software was used to take 4x4 arrays of phalloidin stained cells for F-actin. Images were then analyzed in ImageJ software using the "Trace" tool (N = 3, n = 10) utilizing a double blind measurement protocol of cell spreading as determined by measuring the demarcated outline of the actin cytoskeleton. The 'center' region of each image was considered to be the 100 um radius from the center of the 1-cm culture surface area, while the 'periphery' region was considered to be a 100-um ring width circumference at the outermost region of the 1-cm culture surface area.

Vinculin and actin fluorescent images were taken using either the 10x or 63x objective utilizing a 1.6 Optivar. Z-stack images (10-25 layer range) were captured at 0.25-um slices using DAPI, GFP, and Texas Red filter channels. Additionally, DIC microscopy was used to image the patterned silk film surface for each z-stack layer. For images captured using the 63x objective deconvolution was performed on each z-stack using 3D Huygens Deconvolution Software (Scientific Volume Imaging BV, The Netherlands) to assist with reducing the strong background fluorescence emitted from the silk protein substrates. A total of 40-iterations were performed employing the

software's Classic Maximum Likelihood Estimation (CMLE) algorithm for each z-stack, as it was found that increasing the number of iterations had a minimal effect on improving the image. All other settings were left at manufacturer default settings. Images were produced using both maximum intensity projection (MIP) and surface rendering settings. MIP threshold levels were set at default manufacturer settings, while surface-rendering threshold was set to match MIP image signal localization and intensity. The number of vinculin-positive FAs was quantified, and the plot profile of actin fibers was obtained by using ImageJ (NIH) Plot Profile function. Analysis of vinculin percent image area, number, and average area size were calculated using the ImageJ 'Particle Analysis' functionality. This was accomplished by separating the collected vinculin channel from the deconvoluted z-stack images, then transforming the image into an 8-bit rendering, and the threshold setting was set outside the 95% pixel intensity distribution profile to aid in eliminating background signal.

### 3.10. Western Blot

HCLE cells were cultured upon the various silk film surfaces and glass substrates for 4-hours (n = 12) and 3-days (n = 6) each. The sample number was doubled for the 4-hour time point to ensure enough protein would be collected for Western Blot analysis. At each time point the cell media was removed, and each sample was washed 2x with PBS at 4°C. Following PBS

removal, a 200-uL sample of RIPA buffer solution (Thermo Scientific, Rockford, IL) was added to each sample to release intracellular protein. The RIPA solution was prepared with 3-mL of RIPA buffer each that contained 20-mM Tris, pH 7.2, 150-mM NaCl, 1% Triton X-100, 1% sodium deoxycholate, 0.1% sodium dodecyl sulfate (SDS)), and 30-uL of protease and phosphatase inhibitors (100x Halt™ single-use cocktail, Thermo Scientific). The cell protein was collected using a 1-cm cell scraper device (BD Biosciences, Bedford, MA), and the cell lysate solution was then collected and added to the next sample well to increase the concentration of protein. This process was repeated for each substrate sample group, and the resulting protein lysate was mixed on ice for 15-minutes and then centrifuged at 14,000-RCF for 15-minutes (5415 D, Eppendorf, Inc.). The supernatant was then collected and the cell debris discarded. This experiment was repeated 3x.

The protein concentration of each sample was determined using the bicinchroninic acid (BCA) assay (Thermo Scientific, Rockford, IL) as previously described (40,48,169), and all samples were diluted to 30-ug/mL concentration. Next, 10-uL of NuPAGE® LDS Sample Buffer (4x, Invitrogen, Inc.) was added to each sample, and the protein ladder sample was prepared with 10-uL of LDS, 25-uL of RIPA buffer solution, and 5-uL of protein mix (10747-012, Invitrogen, Inc.). All samples were then heated at 70°C for 10-minutes. Next, two NuPAGE® gels (1.0 mm x 15-well, 4-12% Bis-Tris, Invitrogen, Inc.) were loaded with 15-uL of sample, and ran in 1x NuPAGE®

MES SDS Running Buffer (20x, Invitrogen, Inc.) using a constant 200-V setting for 40-minutes.

After completing electrophoresis the gels were removed from their plastic cases and the proteins were transferred to a polyvinylidene fluoride (PVDF) membrane using the iBlot® Gel Transfer Device (Invitrogen, Inc.). The membrane was then placed into infrared (IR) compatible blocking buffer (Odyssey®, LI-COR Biosciences) for 1-hour. Next, 1:400 primary antibody dilutions of vinculin (V9131, Sigma, Inc.), actin (AB1801, Abcam, Inc.), and GAPDH (AB9483, Abcam, Inc.) were prepared in blocking buffer. Membranes were then incubated in primary antibody solution at 4 °C for 24-hours and then washed 3x with 0.1% TWEEN® 20 (Sigma-Aldrich, Inc.) for 10-minutes each. The appropriate infrared dye labeled secondary antibody solutions were prepared at a dilution of 1:5,000 (IRDye®, LI-COR Biosciences, Inc.) for vinculin, GAPDH, and actin in blocking buffer, and membranes were incubated for 1-hour covered from light. The membranes were then rinsed 3x with 0.1% TWEEN® 20 for 10-minutes each. The membranes were then analyzed on an infrared Odyssey machine (LI-COR Biosciences, Inc.) using Odyssey V3.0 software utlizing both 700-nm and 800-nm wavelengths. Protein densitometry measurements were attained by first adjusting the image display curve to remove background, and then the densitometry was measured with a standard rectangular area for each membrane sample. Ratios from the various sample readings were then calculated.

### 3.11. Statistical analysis

Statistical analysis was performed using the Student's t-test. Differences were considered significant when $p < 0.05$.

## 4. Results

### 4.1. Characterization of Silk Substrates and HCLE Response

Patterned silicon wafers possessing both parallel lines and concentric ring feature geometries were successfully produced, and then used to mold negative pattern imprints onto PDMS surfaces using soft lithography methods (48,104). Patterned silk films of the original silicon pattern were then successfully created as previously shown (25,87,121). Final silk film feature dimension were analyzed using SEM, which demonstrated the expected feature dimensions formed on the silk surface (Figure 1). Flat and patterned silk film surfaces could be produced with high fidelity (Figure A-C). In addition the correct feature pitch was produced on both lined and ringed silk surfaces (Figure B-C) which corresponded with previous results (21,87). Cross-sectional analysis of the silk films demonstrated a smooth surface for flat films (Figure 1D), and correct feature depth was achieved for both patterned surface geometries (Figure 1E).

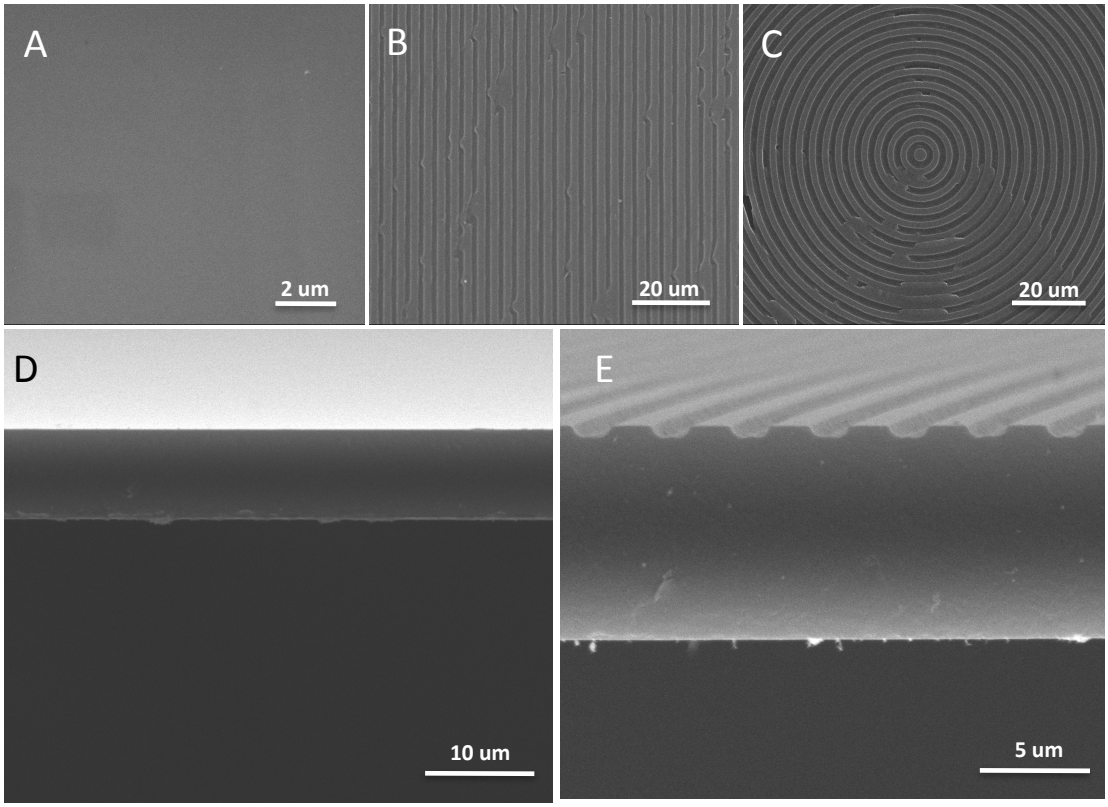


**Figure 1.** En face SEM images of silk film surfaces for (A) flat, (B) parallel lined, and (C) concentric ringed topographies. Cross-sectional images for both (D) flat and (E) patterned silk surfaces demonstrate feature depth and bulk film structure. Measured silk feature dimensions and geometries were comparable to the expected design parameters of a 2-um width, 4-um pitch, and 1.5-um feature depth.

HCLE cells were seeded upon the various silk surfaces and glass controls. Phase contrast imaging after 3-days in culture revealed cultures growing readily on all surfaces (Figure 2A-D). Overall cellular growth upon the surface was similar between controls and flat silk surfaces (Figure 2A-B). In addition patterned feature geometries did not appear to affect cellular growth

as well (Figure 2C-D). Cell counts for the various surfaces after 4-hours in culture revealed that parallel line features appeared to significantly increase (n = 4, $p < 0.05$) initial cell attachment by 33-54% on average when compared to other substrates (Figure 2E). All other surfaces demonstrated similar cell counting results.

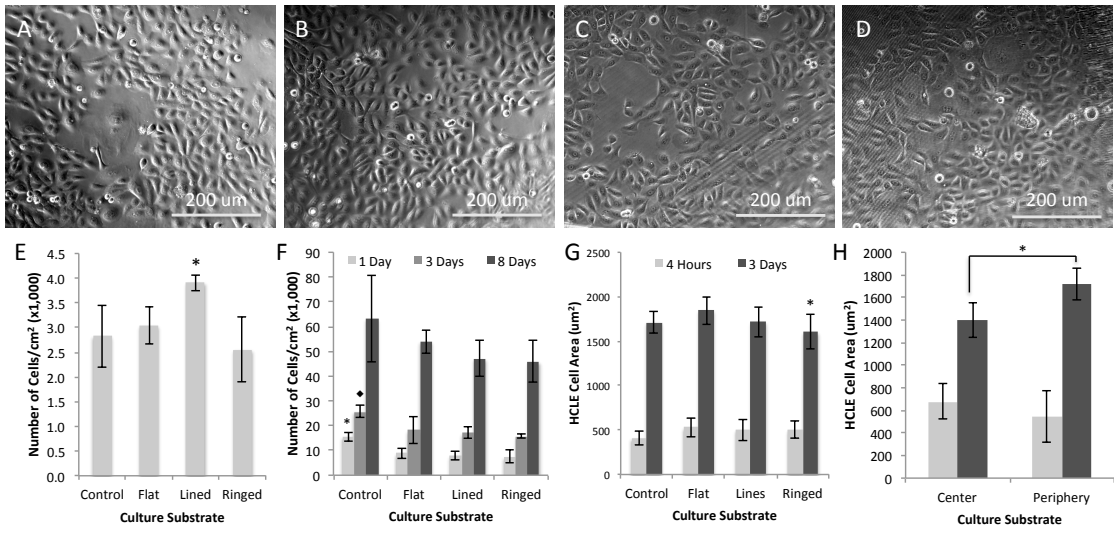


**Figure 2.** Phase contrast images of HCLE cells grown on (A) glass surfaces and (B) flat, (C) lined, and (D) ringed silk substrates after 3-days in culture. (E) Cell counting results for the various substrates at 4-hours in culture where lined silk substrates showed the greatest initial adhesion of HCLEs (* indicates $p<0.05$ compared to all substrates, n = 4, error bars indicate SD). (F) Nucleic acid assay results showing growth characteristics for the various substrates over an 8-day period where glass substrates show greater cell numbers, which then begin to equalize over time in culture (* indicates $p < 0.05$ compared to all substrates and lined and ringed respectively, n = 4, error bars indicate SD). (G) Cell spreading results for the various

cultures, illustrating at 4-hours in culture spreading is the same while at 3-days a difference is detected between flat and ringed silk surfaces (* indicates $p < 0.05$ compared to flat, n = 30, error bars indicate 95% CI). (H) Further spreading analysis revealed that spreading on ringed surfaces is less towards the center where increased feature curvature is present (* indicates $p < 0.05$ for 3-day time points, n = 30, error bars indicate 95% CI), however no significant difference was observed between the peripheral region of the ringed features and the flat silk surfaces (data not shown).

Nucleic acid content assay results revealed the growth profiles for the cultures over an 8-day period (Figure 2F). It was shown that control surfaces had a significant increase in cell number after 1-day in culture ($n = 4$, $p < 0.05$), and had on average a 67%-100% increase in cell number. By 3-days in culture the cell number was still significantly higher on control surfaces as compared to silk, but this increase had decreased to 44%-63% on average and signified silk surfaces were gaining confluence. By 8-days in culture cell numbers were not significantly different between the various surfaces as all cultures were confluent.

Cell spreading was also assessed on the various surfaces (Figure 2G). No significant differences in cell area size was observed for all surfaces at 4-hours in culture. However, by 3-days in culture there was a significant decrease ($N = 3$, $n = 10$, $p < 0.05$) of 15% of cell area on average for cultures on ringed silk surfaces when compared to flat silk films. This was further

analyzed by measuring the center and periphery culture regions for each substrate. Ringed surfaces were the only samples that had a decrease in cell spreading in the center region of the culture substrate when compared to their respective periphery regions ($N = 3$, $n = 10$, $p < 0.05$) (Figure 2H). This was a 23% decrease in cell area on average when comparing between center and periphery on ringed surfaces, while equating to a 32% decrease in cell area on average when comparing between cells growing on the ringed surface central area as compared to flat silk surfaces.

SEM imaging was utilized to visualize cell-surface attachment and intercellular contact formations after 1-day in culture. HCLE cell alignment was observed along the length axis of the parallel line features, and cell processes extended into the pitch depth (Figure 3A). Cell alignment was most prevalent among single cells when compared to cell clusters. The geometry of the surface pattern appeared to dictate cell alignment as cultures grown on concentric ring features appeared to bend with the topography curvature (Figure 3C). This effect was observed near the center region of the ringed features where the degree of curvature was greatest. Comparison of cell morphologies at the border of flat and lined silk film surfaces revealed that culture growth did not appear hampered by the either flat or patterned substrates (Figure 3B). Intercellular contact formation was greatly affected by the presence of the surface pattern. On flat silk substrates intercellular contact were evenly formed along the cell borders (Figure 3D). However, cells cultured

on patterned surfaces formed intercellular contacts localized along the apical surface of the feature, and not within the pitch gap (Figure 3E).

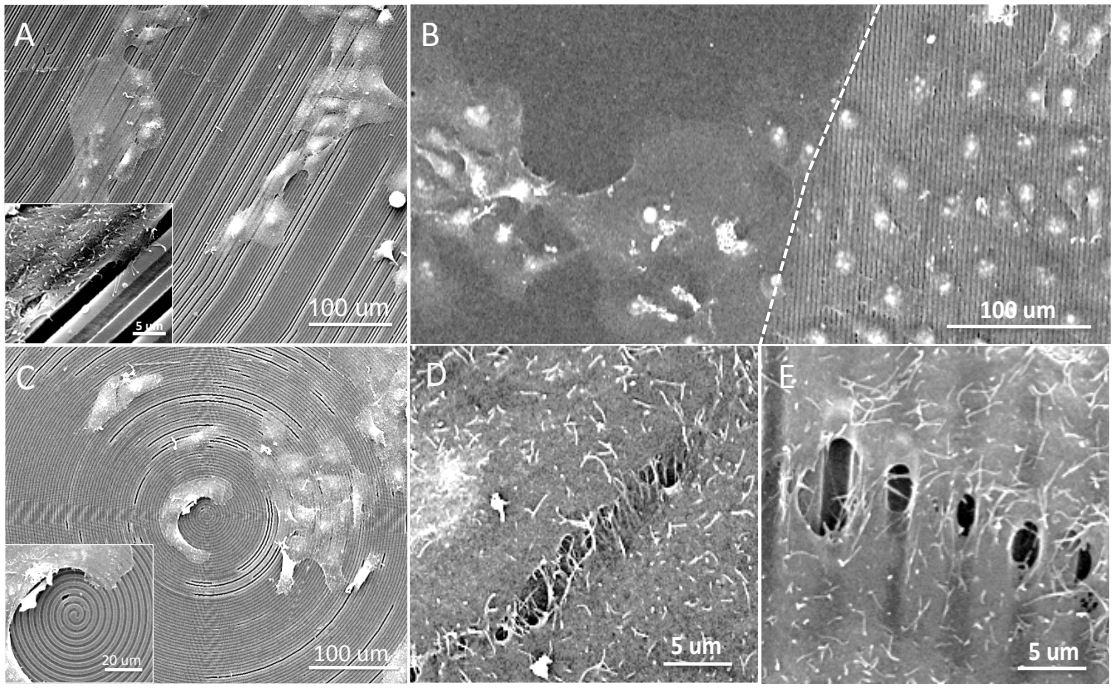


**Figure 3.** Representative SEM images of HCLE cultures upon silk film surfaces after 1-day in culture upon surface features arranged in (A) parallel line and (C) concentric ring geometries. (B) Direct comparison between cells cultured upon border region of flat and patterned silk film surfaces as demarcated by the dotted line revealed similar growth characteristics. Cell contact area for cells cultured upon (D) flat and (E) patterned silk film surfaces indicated the difference in cell-cell contact morphology especially in regard to gaps formed over the feature depths.

## 4.2. Characterization of Cytoskeletal Localization Upon Patterned Versus Flat Silk Film Topographies

HCLE actin fibril architecture and vinculin formation were assessed at 4-hours and 3-days post seeding to assess initial cell adhesion and near-confluent culture time points. The cytoskeleton architecture was significantly affected by the presence of the silk film surface topography. Within 4-hours after cell seeding patterned silk film surfaces induced formation of the actin fibrils along the length of the surface feature axis. Differences in actin formation were observed between patterned and flat silk surfaces. On flat surfaces actin formed primarily in a ring along the cell body periphery (Figure 4A), while on patterned surfaces actin fibers extended across the cell body (Figure 4B-D). By day 3 in culture this difference in actin formation became more pronounced on both the flat (Figure 4E) and patterned surfaces (Figure 4F-G). Differences in actin formation were observed between the parallel line and concentric ring surfaces. On the lined surfaces the actin fibers formed across the cell body tended to align along the length axis of the patterned features (Figure 4F). However, on the concentric ring surfaces actin fibers also formed across the cell body, but did not align with the ringed feature patterns as apparently (Figure 4G).

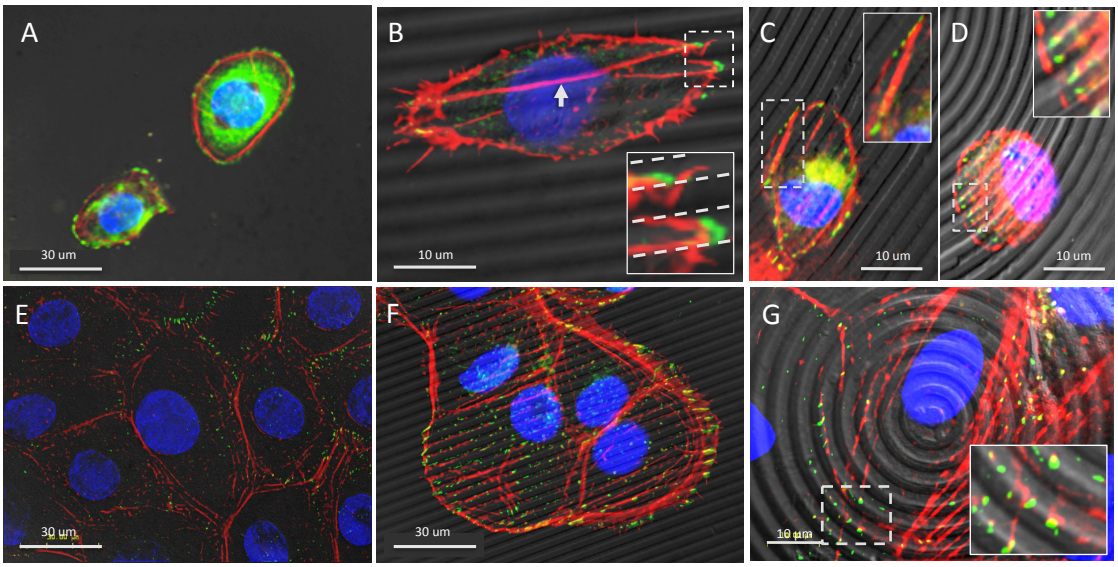


**Figure 4.** Representative fluorescent microscopy images of HCLE cytoskeletal architecture (red – actin, green – vinculin, blue – nucleus) overlayed upon DIC images of respective silk film culture surfaces for (A) flat, (B) lined, and (C,D) ringed topographies after 4-hours in culture. Imaging demonstrated actin fibril and vinculin localization near the cell periphery on flat surfaces, while on patterned surfaces fibril elongation occurred along the feature axis and vinculin localization occurred along the feature edge. Boxed regions show enlarged regions of interest for actin and vinculin localization on patterned silk surfaces. Images taken at 3-days in culture on (E) flat, (F) lined, and (G) ringed silk film topographies demonstrated similar results, but to a greater extent.

FA formation also appeared to be significantly affected by the presence of the surface pattern when observing vinculin localization. On flat silk surfaces vinculin localized towards the cell periphery (Figure 4A), which was also the case for glass controls (data not shown). However, on patterned silk

surfaces vinculin distributed at additional sites along the basal surface of the cells (Figure 4B-D). Specifically, it was observed that vinculin was primarily localizing at the feature edge as formed by the vertical side-wall and horizontal apical surface of the silk substrates. The localization of vinculin to the feature edge was further investigated through the use of 3-dimensional (3D) surface rendering software, which creates a digital rendering of the original fluorescent signature (81,82,170). After 3 days in culture, HCLE cells grown on patterned silk film surfaces appeared to have vinculin localized to the feature edge (Figure 5A). Upon closer examination it was found to localize consistently at the feature edge surfaces (Figure 5B), and the vinculin protein globule extended downward into the feature depth (Figure 5C), which coincided with the location of the feature sidewalls (Figure 5D)

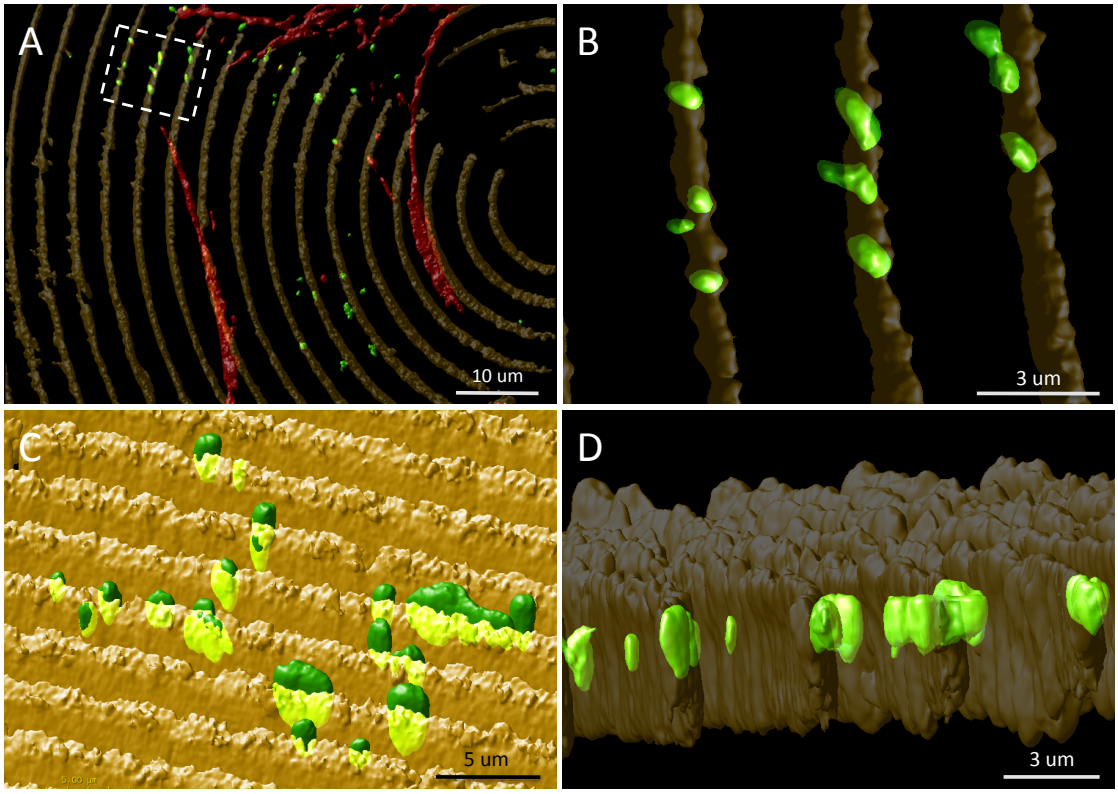


**Figure 5.** Representative 3D surface renderings of a fluorescent microscopy image of an HCLE cell cultured for 3-days upon a concentric ring silk film surface topography. (A) En face image of cytoskeletal architecture (red – actin, green – vinculin) and silk film wall topography (yellow) for a cell cultured in center region of the silk film surface. (B) Magnified image of boxed area of interest from panel-A demonstrating localized vinculin formation on the patterned feature edge region. Alternative angled profile views demonstrating (C) vinculin localization to upper half of feature wall height and (D) penetrating structures into the feature depth.

The influence of surface topography on actin formation was further investigated by analyzing the fluorescent signature intensity of fibril localization upon patterned and flat silk film substrates. Actin alignment was largely absent

after 3-days in culture upon flat silk surfaces (Figure 6A), and the plot profile of a single cell illustrated the absence of intracellular actin formation with an increased signal intensity located at the cell periphery (Figure 6C). Patterned silk topographies exhibited an enhanced effect on intracellular actin fibril alignment (Figure 6B), which was demonstrated by a periodic signal pattern in the plot profile that was characteristic of the surface feature dimensional design (Figure 6D). The frequency of signal peaks appeared in 4-um frequency intervals, and corresponds with the 4-um pitch of the patterned features.

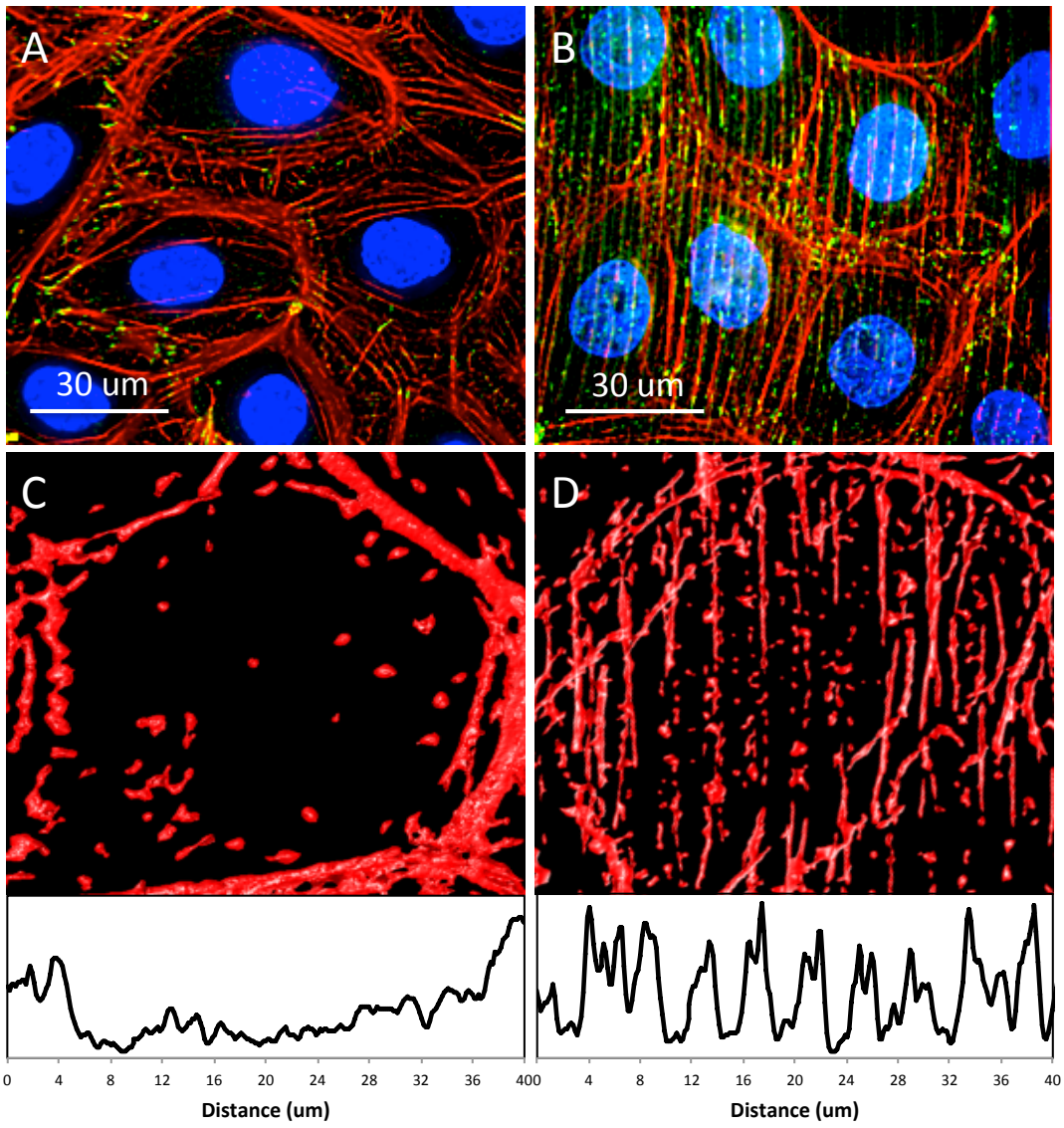


**Figure 6**. Fluorescent microscopy images of the cytoskeletal localization (red – actin, green – vinculin) upon both (A) flat and (B) patterned silk film surfaces. Representative images of cell actin localization upon (C) flat and (D) lined silk film surfaces with respective surface plot profiles shown below demonstrating actin fibril localization towards the periphery on flat silk film surface, and fibril alignment along the patterned lined silk topography as indicated by the periodical intensity peaks corresponding to feature presence.

The influence of surface topography on vinculin formation was further investigated by analyzing the localization of fluorescent signature intensity on patterned and flat silk film substrates at 3-days in culture. Vinculin localization upon flat silk film surfaces was found both intracellularly and at the cell periphery (Figure 7A), which was represented in stochastic patterning of signal (Figure 7C). However, the patterned silk surfaces demonstrated a more pronounced alignment of vinculin than actin fibrils (Figure 7B). Plot profile analysis demonstrated that vinculin localization strongly correlated to the presence of topographic feature edges (Figure 7D). A strong frequency of signal intensities was apparent at 2-um distances upon patterned silk film substrates, which was characteristic of the surface feature dimensional design.

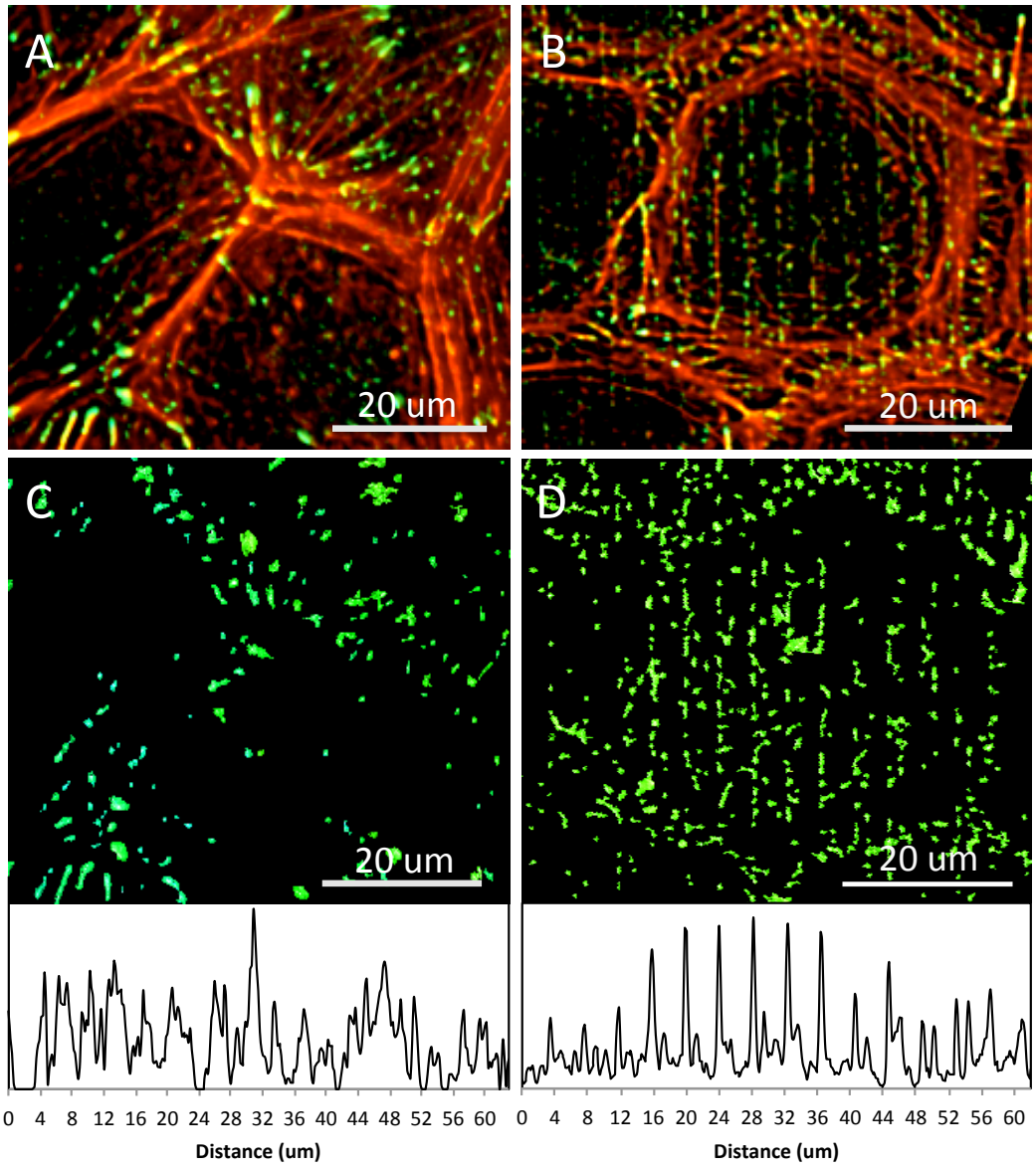


**Figure 7.** Fluorescent microscopy images of cytoskeletal localization (red – actin, green – vinculin) upon (A) patterned and (B) flat silk film surfaces, with (C-D) respective vinculin localization surface plots shown below to illustrate degree of FA patterning corresponding to signal intensity peaks upon patterned silk topographies as compared to the stochastic peak intensity profiles for flat silk surfaces.

### 4.3. Analysis of Vinculin Localization and Cytoskeletal Protein Quantification

As a marker of focal adhesions (FA), vinculin fluorescent signal localization was compared between parallel line and concentric ring patterned silk substrates, flat silk surfaces, and glass controls. Percent total vinculin area localization significantly increased ($n = 7$, $p < 0.05$) on parallel lined topographic features by over 2-fold on average when compared to other substrates after 4-hours in culture (Figure 8A). After 3-days in culture, lined feature surfaces demonstrated the greatest percent reduction in vinculin localization for all substrates when compared to respective 4-hour time points. Specific sites of vinculin concentration for HCLE cells on both patterned silk topographies and glass control substrates were measured as an estimate of FA size (Figure 8B). Analysis of the discrete areas of vinculin localization at 4-hours in culture revealed that there was no difference between estimated FA size over the various substrates. At the 3-day time point an over 4-fold increase in estimated FA size occurred on all silk film substrates, while glass substrates showed a minimal increase in size between the two time points. In summary, lined topographies experienced the greatest decrease in total vinculin localization, while demonstrating the least increase in discreet vinculin area over time as compared to other silk substrates.

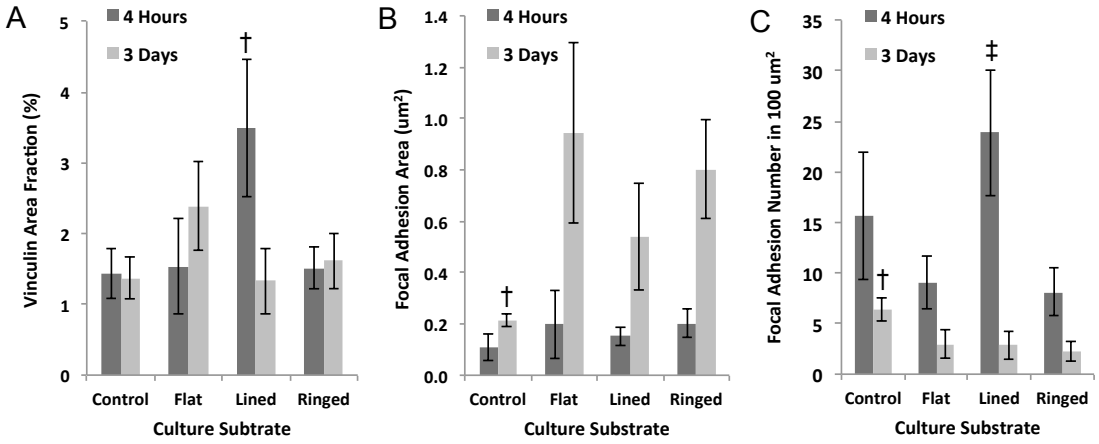


**Figure 8.** (A) Quantified analysis of vinculin signal area as a percentage of total image area indicating lined silk film surfaces had the greatest vinculin localization at 4-hours in culture and similar levels across all substrates after 3-days in culture. (B) Individual FA area as defined by discrete areas of vinculin measurements indicating silk surfaces had significantly larger FAs than control surfaces by 3-days in culture. (C) Total FA number per 100 $um^2$ area as defined by vinculin staining upon various culture substrates indicating the highest number on lined silk surfaces as compared to other silk surfaces after 4-hours in culture, and a significant decrease in FA number by 3-days in culture for all surfaces (n = 7; error bars = 95% CI; †‡ - indicates $p<0.05$ when compared between groups and between other silk substrates respectively).

Further analysis investigated the number of FA formed per area of culture substrate as indicated by the presence of vinculin signal (Figure 8C). The analysis revealed that all substrates had a 2 to 5-fold decrease in FA number when comparing 4-hour and respective 3-day time points in culture. The largest decrease in FA number was observed for parallel line feature

topographies, which showed a 5-fold decrease over time in culture. In addition, the parallel line substrates were equivalent in number for FA formations as compared to glass control substrates after 4-hours in culture. However, all silk substrates showed a statistically significant ($n = 7$, $p < 0.05$) decrease in FA formation by day 3 in culture when compared to glass controls. Similar results were shown on glass substrates, however the FA number was reduced to a much lesser extent.

Western blots detecting actin, vinculin, and GAPDH controls were performed to investigate whether the observed effects of the various silk film surfaces on actin and vinculin localization were related to a difference in quantity of the proteins, or to an alteration in their distribution. It was shown that all proteins were produced at detectable levels for all surfaces and at both 4-hour and 3-day time points (Figure 9A-B). Analysis of densitometry measurements revealed actin/GAPDH ratios were consistent for all substrates at the 4-hour time point, and then at 3-days in culture there was a significant increase in actin/GAPDH ratios for all silk substrates, but not glass controls (Figure 9C). In addition, actin/GAPDH values were significantly reduced on glass surfaces when compared to flat and lined silk film surfaces, and on average this corresponded to a 34%-42% decrease on average. Vinculin/GAPDH ratios were found to significantly increase between the two sampling time points for all surfaces, with glass controls having the lowest change in expression on average (Figure 9D). Vinculin/actin ratios remained

relatively consistent amongst all surfaces for both time points, with a significant increase for all substrates between time points (Figure 9E).

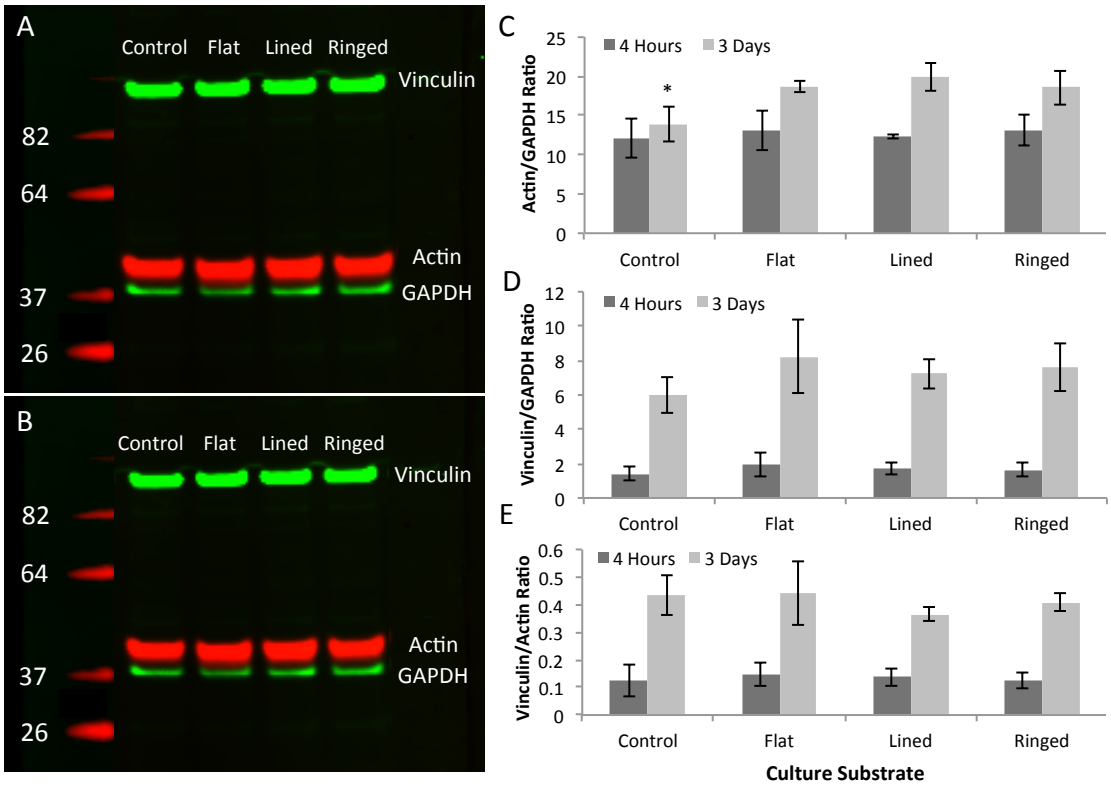


**Figure 9**. IR western blot results for actin, GAPDH, and vinculin proteins present in HCLE cells cultured upon the various silk and glass surfaces after (A) 4-hours and (B) 3-days in culture. Analysis of protein OD measurements ratios after 4-hours and 3-days in culture for (A) actin/GAPDH, (B) vinculin/GAPDH, and (C) vinculin/actin ratios (n = 3; error bars = standard deviation; * - indicates $p < 0.05$ when compared to control).

## 5. Discussion

Silk film surfaces can be patterned to produce micro to nano-topographic

features that affect various aspects of cell function (21,90,93,98,171). The influence of surface topography to affect corneal epithelial cell response has been previously shown to effect proliferation, migration, tissue development, and cell adhesion on silicon surfaces (79,80,87,121). However, the use of silicon is not favorable for *in vivo* translation, fabrication of such materials requires a high level of expertise, and per sample production is relatively costly. Using patterned silk surfaces offers a number of advantages based on their biomaterial properties, and as a result of their straightforward and inexpensive production methods (40,48). Therefore, silk films with both parallel line and concentric ring topographies were fabricated to assess cellular response to varying feature geometries and material surfaces. Such patterned silk surfaces have not been used as a culture substrate for a corneal epithelial cell type before.

HCLEs were able to attach and grow to confluency on both patterned and flat silk surfaces. Cell growth characteristics were similar overall between the various silk substrates, however overall cell number was less when compared to glass surfaces. After a week in culture silk surfaces possessed similar cell numbers as glass surfaces, and indicate that silk surfaces offer a viable substrate for cell expansion. These results may also indicate that silk film surface chemistry may inhibit cell proliferation to some degree as previously demonstrated, however it is still unclear what is causing this effect (48). Silk films with lined surface features appeared to demonstrate an

enhanced characteristic of increasing initial cell adhesion when compared to other silk and glass surfaces. Such findings are not completely unexpected as previous results have been reported for corneal epithelium grown on patterned silicon surfaces (87,121). This has largely been characterized as a result of increased attachment area presented to cells on patterned surfaces, and may enable enhanced cell binding to the surface (87). However, similar initial attachment was not observed for concentric ring surfaces as would be expected if this was only a topographic effect, and may be related to the degree of patterned feature curvature. In addition, a significant decrease in cell spreading within the center region of concentric ring surfaces where the degree of feature curvature is the highest was also observed. Feature curvature has been shown to affect cell responses such as proliferation, apoptosis, and differentiation (81,82), and further work is needed to assess feature curvature and initial cell adhesion characteristics.

The presence of the surface pattern produced significant differences in cell morphology, which is most likely due to topographic contact guidance (90,93,171). In the above study, the most prominent changes occurred with cell body orientation and intercellular contact formation. HCLE cells tended to align with the patterned feature length axis. Additionally, the morphology of cell-to-cell contact formation was greatly affected by the presence of the pattern. Cell-to-cell contacts appeared to be more prominent upon the patterned culture substrates when compared to flat surfaces. In addition, gaps

appeared between contact regions on the patterned silk surfaces, while found to not be present on the flat substrates. This result is not unexpected, as these cell contact gaps occur in the absence of a basal culture surface between patterned surface features. This effect illustrates the impact that patterned surfaces have on cell-to-cell interaction, and may have farther reaching implications for intercellular communication (1,172).

In addition to cell morphology and alignment, components of the cytoskeleton were also significantly influenced by the presence of the surface pattern. Actin fibrils, which are one of the primary components of the cytoskeleton, were found to highly align with the silk film's surface topography. Contact guidance of actin fibril formation appeared to be directed along the length axis of the patterned features as shown in previous studies (3,84,173). The control of actin fibrils directionality to induce cell alignment has been shown to have powerful implications in the development of tissue engineered constructs for the cornea (27,93). In addition to fibril localization, analysis of the actin/GAPDH ratios from western blot results indicate that as the HCLE cells grow to confluency there is an increase in actin on silk film substrates when compared to glass controls surfaces. Equivalent ratio values were found on both flat and patterned silk surfaces, and these results may suggest that silk film material chemistry may be playing a role in cytoskeletal development as well and not based strongly on topography. Future work is needed to better elucidate how directionality of these fibrils is both determined and controlled

mechanistically through the use of surface topography.

Previously, it was been shown that the presence of a feature edge surface provides an 'optimal' anchor location for FA complex formation (26,37,86,161). The FA complex is a critical component in cellular signal transduction between the extracellular and intracellular environment by connecting integrin substrate anchoring proteins to the actin fibrils of the cytoskeleton (6,162,174). Vinculin is an important protein component of the FA complex, which is thought to help stabilize this structure during and after formation (9,26,47,48,175). The results above demonstrate that vinculin localization primarily occurs along the feature edge, and corresponded with actin fibril anchoring. Furthermore, this localizing effect was not impacted by feature edge geometry as both lined and ringed topographies demonstrated this characteristic. The prevalence of vinculin localization to the silk film feature edge may indicate that topographic edges expose cells to a greater amount of 'attachable' culture substrate regions. This hypothesis is supported by the fact that the addition of the patterned features introduces an increased density of edge lengths accessible to the adhering cells, while effectively reducing the culture surface by half. Increased presence of edge structures, and not increased surface area, may significantly drive the formation of vinculin along the feature edge. Once these surface anchor points are established the actin fibrils can polymerize from the feature edge surface, and as a result this may help to induce the observed contact guidance effect of

cytoskeletal alignment. Further work should be undertaken to visualize the formation of the cytoskeleton in real time, which could provide answers to how contact guidance is induced upon a patterned substrate.

HCLE cells cultured upon silk film substrates tended to reduce vinculin localization while simultaneously increasing vinculin size over time. A similar effect was also witnessed upon glass surfaces, but to a lesser extent. Silk films as a culture substrate promoted increased vinculin area size when compared to glass substrates. Increased vinculin localization, as demonstrated on the silk film substrates above, have been shown to act as a scaffolding protein to support FA development and promote cell-to-surface attachment (21,25,83,175). These results suggest that the silk substrates offer a favorable substrate for cell attachment, which may be enabled through enhanced FA development. However, the analysis of vinculin/GAPDH ratios from western blot results indicated that no increase in protein formation was induced by the presence of the silk film pattern, or the change in material substrate. These results may indicate that patterned feature edges appear to redistribute intracellular proteins, such as vinculin, by providing a localized assembly point during FA formation as opposed to inducing increased protein production. Analysis of additional FA proteins along with determination of cell-to-surface attachment forces may provide further understanding of how silk surface topography effects cell attachment.

## 6. Conclusions

Silk films are a novel class of biomaterials, which have the potential to be tailored for ophthalmic applications pertinent to ocular surface repair (21,22,54,81,83,163). In the current study corneal epithelial *in vitro* interactions were assessed on patterned silk film surfaces. The response of an HCLE cell line to culture substrates with either parallel lines or concentric ring surface topographies were compared to flat silk and glass control surfaces. The effects that these patterned biomaterials have on initial cell-to-surface attachment and cytoskeletal development over time was explored. The results above taken together illustrate the various effects that silk surface topography may have on cultured HCLEs. The combined observations of direct effects on cell attachment, spreading, and cytoskeletal protein distribution illustrate a sample of parameters that may be controlled for by topography design.

Of particular interest is the finding that lined surface topographies increase initial cell attachment, while simultaneously increasing localization of vinculin and FA formation at the same time. This illustrates the fact that lined surface topographies may promote enhanced cell attachment through redistributing intracellular FA proteins to the feature edges. This redistributing effect may be driving subsequent actin alignment either through fibril formation from FA contacts or through another nondescript mechanism. It can be shown that feature geometry, such as with the added presence of curvature, is an important factor in surface design as demonstrated through the cell response

upon concentric ring features. Concentric ring geometries did not enhance initial cell adhesion, promoted reduced cell spreading, and do not induce enhanced initial FA formation. Actin fibrils were found extending from the ringed feature edge and anchored at FA complexes. However, as somewhat expected the formed actin fibrils did not align with the curved features but instead crossed over various features especially in regions of high curvature. Interestingly, vinculin redistribution was still prevalent upon ringed feature edges, thus suggesting the importance of edge presence for guiding FA localization. The enhanced initial attachment of cells and increased FA number upon parallel lined features may correlate to the fact that such topography may promote actin alignment in their native direction, while ringed features do not and therefore may not enhance initial cell attachment or FA formation through not promoting fibril directional alignment. Additional studies will need to investigate the intracellular mechanistic relationships that the presence of the various surface topographies may have on actin fibril formation and alignment. Further work may build off these results in the development of silk film designer surfaces that promote an enhanced corneal epithelial cell response, such as epithelial cell adhesion, that could find use in the development of clinically relevant cell carrier surfaces or in the production of a tissue engineered cornea.

CHAPTER 7

# Surface Topography Guides Corneal Epithelial Cell Sheet Migration

## 1. Summary

Collective cell behavior of migrating human corneal limbal-epithelial (HCLE) cell sheets were studied on flat and micro-patterned silk film surfaces. The presence of topographic features significantly increased cell sheet alignment by 75% through enhancing cell sheet migration along the feature edge axis. This occurred through influencing cell migration direction for individual cells composing the collective cell sheet. This was demonstrated as 3-fold decrease in cell migration efficiency (η) for cell sheets migrating perpendicular to the feature edge on silk substrates. Directional selection appeared to be influenced through a cytoskeletal protein localizing effect elicited by the presence of the patterned feature edge region. This was demonstrated by the localized formation of actin fibrils, focal adhesions, and GTPases near the feature edge. As a result directional selectivity of individually migrating cells seems to be less inhibited along the feature edge where there is a decrease in protein localizing edge regions. Future efforts will expand on the use of patterned silk films to augment a specific cell response that can produce a collectively relevant clinical effect.

## 2. Introduction

Basement membranes are sheet-like extracellular matrix (ECM) structures located on the basal side of epithelial tissue, and provide a complex 3D nanoscale topography that offer a physical support and chemical ligand binding sites for epithelial cell attachment and migration (24,89,176). In addition, basement membranes are broadly involved in many physiological processes such as tissue repair, embryogenesis, and morphogenesis (6,21,22,24,26,54,88,177). The interaction of basement membrane surface topography with surrounding cells may profoundly influence cell functions through a phenomenon known as contact guidance. The phenomenon of contact guidance is characterized by the response of cells to structures on the nano to micro scale and result in changes in local cell adhesion, polarization, migration, and differentiation (25,79-81,171). The topography of the human corneal epithelial basement membrane, the Bowman's layer, has been characterized to be a felt-like arrangement of fibers with processes and pores that have feature sizes in the nano- and micro-scale range (21,87). Further work has demonstrated that the presence of the surface topography is important for corneal epithelial adhesion, migration, and tissue development (40,79,80,80,121,121,122,178).

The effects of contact guidance are mainly observed as an alignment of the cytoskeleton, elongation of cell morphology, and oriented cell migration in the direction of the underlying patterns (123,173,178,179). Such studies have

shown that the topographic cues, independent of biochemistry and mechanics, can significantly influence cell behaviors. Recent studies have shown that the size and shape of patterned substrates can direct the differentiation of progenitor cells (21,82). Such studies provide evidence that the topographic cues may not only regulate cell phenotypic behaviors, but also profoundly influence gene expression. As a result the naturally occurring cues to illicit contact guidance could play an important role in regulating cell function during various biological processes. Investigation is currently underway to apply such biomimetic principles into the development of tissue-engineered constructs, including corneal tissue-engineering (21,40,93,180).

Current investigations of contact guidance have primarily focused on the behavior of single cell suspensions cultured on silicon wafers or synthetic polymer surfaces. However, the use of silicone wafers or non-biocompatible materials do not integrate with the surrounding tissue environment and make in vivo translation improbable. Furthermore, seeding of single cells for the study of epithelial contact guidance does not recapitulate the in situ environment where epithelium spreads over surfaces en masse (89,164,176). During corneal homeostasis and wound healing, corneal epithelial cells are not isolated, but instead proliferate and migrate as cells sheets with the potential for myriad intercellular interactions that may be greatly influenced by the presence of topographic features. As a result such studies may not be optimal from both a physiological and in vivo translation standpoint. The current study

circumvents these issues by investigating the influence of contact guidance on more physiologically relevant cell sheets cultured on a highly biocompatible silk film substrate.

Developing biomaterial technology is a foundational area of research in the emerging fields of tissue-engineering and regenerative medicine. Regenerated silk protein solution is considered to be a novel choice of biomaterial selection due to the protein's inherent biocompatibility and nonimmunogenic properties when implanted in vivo (7,9,34). Silk films cast from this regenerated protein solution have been found to be transparent and possess tunable material properties in terms of mechanical strength, degradation rate, geometric design, and both surface chemistry and topography (24-27). These properties combined with inherent biocompatibility and transparency make it uniquely suited for use in the cornea as a clinical tool and for tissue-engineering purposes (21,22,24,88,128,177). It has also been shown that silk films can be surface patterned on the nanoscale (25,47,79-81,100,171), and these film topographies may be used to influence corneal cell properties (21,48,87,98). The current study aims to better understand how surface topography affects epithelial cell sheet migration, which is an essential property for successful healing of the ocular surface after injury (79,80,121,178,181). Here, silk films with patterned micro-surface topography were seeded with human corneal-limbal epithelial (HCLE) cells to study the effect of these surface structures on corneal epithelial sheet

migration. Findings from this study will contribute to the knowledge of how collective corneal epithelial cell sheets are influenced by topographic cues in their microenvironments and how these interactions influence cell behaviors. Findings will support ongoing efforts to better understand how fundamental surface design criteria may be produced to enhance clinical applications in ocular surface repair and cornea tissue engineering.

## 3. Materials and Methods

### 3.1. Production of Silk Solution

*Bombyx mori* silkworm cocoons (Tajima Shoji Co., Yokohama, Japan) were cut into thirds and then boiled for 40-minutes in 0.02M $Na_2CO_3$ (Sigma-Aldrich) to extract the glue-like sericin proteins from the structural fibroin proteins as previously described (21). The fibroin extract was then rinsed three times in $dH_2O$ for 20-minutes per wash then dried overnight. The rinsed fibroin extract was then dissolved in 9.3M LiBr solution at room temperature, and placed covered within a 60°C oven for 4-hours. The solution was dialyzed in water for 48-hours (MWCO 3,500, Pierce, Inc.). The dialyzed silk solution was centrifuged twice at 13,000-g, and the supernatant collected and stored at 4°C. The final concentration of aqueous silk solution was 8 wt./vol.%, as determined by gravimetric analysis.

### 3.2. Patterned Silicon Wafer Production

Silicon wafers possessing parallel line topographies were prepared using standard photolithographic and ion etching techniques. The features were designed to have a 2-µm width, 4-µm pitch, and 1.5-µm depth. Width and pitch measurements were chosen based on previous literature that demonstrated this dimension produced a contact guidance effect upon corneal epithelium, which modulated various cellular characteristics such as alignment and adhesion (40,80,121,122). The 1.5-µm depth was chosen based on previously cited experiments that indicated this depth appears to have a negligible effect on cellular function and eliminates the potential cell response variability resulting from feature depth in the study (123).

Photolithography mask patterns were designed using L-edit software (Tanner EDA, Inc.) and then imported into a DWL66 laser pattern generator and direct write machine (Heidelberg Instruments, Heidelberg, Germany) for production onto a photoresist coated glass substrate. The finished mask was then placed within an Autostep 200 DSW i-line wafer stepper (GCA, Inc.) for photolithographic patterning of photoresist coated 100-mm diameter silicon wafers. Wafers coated with 1-µm thick layer of photoresist (Megaposit™ SPR™ 220-3.0, Dow Chemical, Inc.) were produced as a 21-die array in a [3:5:5:5:3] design upon a 100-mm silicon wafer. Individual dies have a 10-mm diameter separated by 5-mm spacing. Feature dimensions were verified using SEM. The wafers were then placed into a Unaxis 770 ion etching device

(Plasma-Therm, LLC, St. Petersburg, FL) to produce 1.5-µm depth etch. The above process was designed to provide repeated topographic features measuring 2-µm in width, 4-µm in pitch, and 1.5-µm in depth over a circular surface area 1 cm in diameter. Feature sizes were then imaged using an Ultra scanning electron microscope (SEM, Zeiss, Inc.).

### 3.3. Casting Surface Preparation

Flat poly dimethylsiloxane (PDMS) substrates of 0.5 to 1.0-mm thickness were produced by pouring 5-mL of a 1:10 casting catalyst/potting (Momentive, Inc., Albany, NY) solution onto patterned silicon wafer surfaces. The cast PDMS solution was then degassed for 2-hours under vacuum, and then cured in an oven at 60°C overnight. The following day the cured PDMS was removed from the silicon substrate and then punched to form round 14-mm circles centered on the patterned surface. The PDMS substrates were placed cast side up and dust/debris stripped using clear tape. The surfaces were further cleaned with a 70% ethanol wash, three $dH_2O$ rinses, and then allowed to air dry in a clean environment. PDMS surfaces were used for multiple silk film castings. Before additional casting, the PDMS surfaces were prepared using a 9.3M LiBr soaking step with subsequent ethanol and $dH_2O$ rinses to remove residual silk fibroin protein from the surface.

### 3.4. Silk Film Casting and Sterilization

Silk films 40-µms in thickness were cast using 75-µL of 8% silk fibroin solution cast upon the round PDMS surfaces as previously described (21). After casting, films were covered with a venting lid and allowed to dry for 24-hours to form the patterned silk film surface. Appropriate numbers of silk films were prepared depending on the experimental setup. Silk film samples were then water-annealed (WA) by placing the samples in water filled containers (i.e. emptied plastic desiccator) in which a vacuum (10-psi) was used to produce a water-vapor saturated environment and left to sit for greater than 5-hours. This process induces ß-sheet protein secondary structure formation and produces a water-insoluble silk film for cell culture (40). The silk film sample surface topographies were imaged using SEM to verify surface feature dimensions [Figure 1].

After the WA process, silk film samples were removed from their PDMS surfaces and submerged within 70% EtOH for 15-minutes in a clean bench environment. In addition, 15-mm diameter glass cover slip control surfaces and stainless steel O-rings (Superior Washer, Inc., Hauppauge, NY) measuring 15.4-mm in outer diameter and 11.6-mm in inner diameter were submerged within 70% EtOH for the same time period. Silk film samples and glass control surfaces were then placed pattern side up into 24-well plates, and a stainless steel O-ring was placed on top to hold the film down to the culture well bottom surface. Films were then subsequently washed three times

with 1-mL of sterile PBS. The silk film samples were left in the final PBS wash until ready for cell seeding to maintain material hydration.

### 3.5. Cell Culture and Collective Cell Migration Assay

A previously established immortalized human corneal-limbal epithelium (HCLE) cell line was kindly provided by Dr. Ilene Gipson (Schepens Eye Research Institute, Harvard Medical School, Boston, MA). The HCLE cultures were chosen based on the cell line's highly characterized history, and offers much reliability when working with new culture substrates (164). All cell media supplies were purchased from Invitrogen (Eugene, OR). The cells were cultured in keratinocyte serum free medium (K-SFM, Invitrogen) with 1% 100X penicillin-streptomycin, 0.3 M $CaCl_2$, 0.45 vol.% bovine pituitary extract (BPE), and 0.2 ng/mL of epithelial growth factor (EGF, Human recombinant). The HCLE cell lines were cultured until 90% confluent and then trypsinized. Trypsinzation was halted using passaging media (DMEM/F12 with 10% calf serum and 1% 100X penicillin-streptomycin), the cells were spun down, and the cell pellet was suspended in a small volume of K-SFM to achieve a final cell density of $10^7$-cells/mL. In order to create a collective cell sheet, 1-µL droplet of cell suspension was seeded upon the patterned and flat silk films and round glass cover slip controls placed in a 24-well dish. The cultures were incubated at 37$^o$C and 5% $CO_2$ for 30-minutes to allow for cell attachment. Finally, 0.5-mL of media was added to each well and changed every two days.

### 3.6. Microscopy Setup

All phase contrast, differential interference contrast (DIC), and fluorescent images were taken using an Observer Z1 fluorescent microscope (Carl Zeiss, AG) with either a 2.5x (NA 0.12 air), 10x (NA 0.45 air ) or 63x (NA 1.4 oil) objective lens utilizing either a 1.0 or 1.6 Optivar optic (OV) as indicated. An AxioCam single channel camera and AxioVision software (Carl Zeiss, AG) were used to capture all images as indicated.

### 3.7. Cell Droplet Dispersion Assay

After the cell droplets were seeded upon the various surfaces and incubated for 1-day, phase contrast images were taken to record the shape of the collective cell sheets (n = 4) using a 10x objective lens. A mosaic of several images were combined together using the MozaiX program within the Zeiss AxioVision software package in order to view the entire culture. ImageJ was used to analyze the aspect ratio of cells in culture by measuring the maximal length of cell spreading parallel to the patterns over cells spreading normal to the patterns.

### 3.8. CyQuant Nucleic Acid Content Assay for Cell Proliferation

The CyQuant NF (Invitrogen, Inc., Eugene, OR) assay was utilized to assess cellular nucleic acid content as a measure of initial cellular adhesion and culture proliferation upon the various silk film substrates and glass coverslip

controls. After 1 and 5-days of cell culture 500-µL of CyQuant NF solution was added to each sample (n=3 for each surface) including a blank control that was incubated without the presence of cells and incubated for 2-hours at 37°C. Then 200-µL of post-incubation sample solution was collected into a 96-well plate. Sample fluorescence intensity was then measured using a SpectraMax M2 fluorimeter microplate reader (Molecular Devices, Inc., Sunnyvale, CA) with excitation wavelength at 485-nm and emission wavelength collected at 530-nm. Averaged blank control values (n=3) were subtracted from all sample readings.

### 3.9. Collective Cell Migration Assay and analysis

After 1-day of incubation to allow cells to attach and form a collective cell sheet upon silk film surfaces, cell migration was monitored using the microscope's 24-well plate micro-incubator (PeCon, GmbH; M24 S1). Time-lapse phase contrast imaging was utilized to record a frame every 10-minutes over a 10-hour period. In order to study the effects of surface patterns on cell migration the microscope objective was focused on the edges of cell sheet. Additionally, for patterned silk surfaces cell sheet migration moving either parallel or perpendicular to the surface pattern direction was imaged to elucidate the effects of surface feature edge orientation. The sheet migration effects elicited from cell population growth and cell-cell contact formation were inhibited in the cell sheet cultures. To reduce growth pressure from dividing

cells, confluent HCLE cultures were incubated for 2-hours in media containing 4-ug/ml of the mitotic inhibitor Miomycin-C (MMC). Culture were then subsequently trypsinized and replated as a cell droplet. To reduce cell-to-cell contacts cultures were fed media containing mouse anti-E cadherin (AEC) at a concentration of 5-ug/ml (SHE78-7, Invitrogen).

As a comparative measure for leader cell formation upon the various surfaces tortuosity values (τ) for the cell sheet border was assessed by measuring the arc-chord ratio from the extracted images of the time-lapse videos, which is defined as:

$$\tau = (\frac{L}{C} - 1)$$

Where L is the total curve length of the migrating cell sheet border as measure using the 'Free-hand' tool in ImageJ, and where C is the measured linear distance between the ends curve length ends as measured using the ImageJ 'Line' tool.

Cell sheet migration rate was quantified by exporting phase contrast images from the time-lapse movies at initial 0-hour and 10-hour time points in culture. Quantification was accomplished by opening images in ImageJ software (ver. 1.45, NIH), and using the 'Distance between Polylines' plugin to measure the average distance and respective standard deviation between cell sheet borders at the varying time points at 10-μm intervals along a 1,000-μm total distance. To accomplish this, the initial measurement angle was set in the respective direction of the cell sheet migration as indicated from each

respective sample video. The 0-hour image cell sheet border was traced using the 'Trace' tool within the plugin, and the respective 10-hour time point image was then overlaid and the cell sheet border traced. This was done for n = 4 samples for each surface condition. Single cell migration was analyzed using the 'Tracking' package in AxioVision software for individual time-lapse movies. Randomly sampled cells from various cell sheet cultures (n = 20, N = 4) were tracked from representative locations of the cell sheet on silk and glass surfaces. For silk surfaces flat and cells traveling either parallel or perpendicular to the feature edge were assessed. The software compiled measurements for total distance, straight distance, tortuosity, and migration rate. In addition, the cell sheet migration efficiency (η) was calculated as:

$$\eta = \frac{\Delta x_S}{\Delta t_S} \Big/ \frac{\Delta x_C}{\Delta t_C}$$

where $\Delta x_S$ and $\Delta t_S$ is the change in cell sheet movement and corresponding times respectively, while $\Delta x_C$ and $\Delta t_C$ is the change in single cell movement and corresponding times respectively. Standard deviation were taken as the quotient propagated error.

### 3.10. Immunofluorescent Staining and Imaging

Following time-lapse imaging of cell migration, all samples were fixed with 4% paraformaldehyde in PBS for 15-minutes, permeabilized with 0.4% Triton in PBS for 5-minutes, and blocked with 2% BSA in PBS for 30-minutes at room

temperature. Focal adhesions and GTPase proteins were visualized by immunostaining with a 1:600 dilution of primary antibodies for vinculin (V9131, Sigma, St. Louis, MO), RhoA (ab54835, Abcam, Cambridge, MA), phosphorylated RhoA (p.RhoA, ab41435, Abcam, Cambridge, MA), and Rac1+Cdc42 (ab18758, Abcam, Cambridge, MA) for 1-hour at room temperature, followed by incubation with Oregon Green 488 goat anti-mouse secondary antibody (O11033, Invitrogen, Eugene, OR) at a 1:800 dilution for 1-hour. F-actin and nuclei were then stained by incubating cells in 1:100 dilution of Alexa Fluor 568 Phalloidin (A12380, Invitrogen, Inc., Eugene, OR) and 1:10,000 dilution of DAPI (83210, AnaSpec, San Jose, CA) for 20 and 5-minutes respectively, while protected from light. After rinsing with PBS, samples were placed on a glass slide and covered with a glass cover slip and mounting media (Vectashield, Vector Laboratories, Inc., Burlingame, CA). Fluorescent images were taken using the microscope setup described above using the 63x objective lens. The number of vinculin-positive focal adhesions was quantified by using ImageJ, and a linescan of actin fibers was obtained by using MetaMorph software (Molecular Devices, Inc., Sunnyvale, CA).

### 3.11. Western blot analysis of GTPase protein content

HCLE cell sheets were cultured as described above upon the various silk film surfaces and glass substrates for 2-days. The cell media was removed, and each sample was washed 2x with PBS at 4°C. Following PBS removal, a 200-

uL sample of RIPA buffer solution (Thermo Scientific, Rockford, IL) was added to each sample to release intracellular protein. The RIPA solution was prepared with 3-mL of RIPA buffer each that contained 20-mM Tris, pH 7.2, 150-mM NaCl, 1% Triton X-100, 1% sodium deoxycholate, 0.1% sodium dodecyl sulfate (SDS)), and 30- µL of protease and phosphatase inhibitors (100x Halt™ single-use cocktail, Thermo Scientific). The cell protein was collected using a 1-cm cell scraper device (BD Biosciences, Bedford, MA), and the cell lysate solution was then collected and added to the next sample well to increase the concentration of protein. This process was repeated for each substrate sample group, and the resulting protein lysate was mixed on ice for 15-minutes and then centrifuged at 14,000-RCF for 15-minutes (5415 D, Eppendorf, Inc.). The supernatant was then collected and the cell debris discarded. This experiment was repeated 3x.

The protein concentration of each sample was determined using the bicinchroninic acid (BCA) assay (Thermo Scientific, Rockford, IL) as previously described (169), and all samples were diluted to 30-ug/mL concentration. Next, 10-µL of NuPAGE® LDS Sample Buffer (4x, Invitrogen, Inc.) was added to each sample, and the protein ladder sample was prepared with 10-µL of LDS, 25-µL of RIPA buffer solution, and 5-µL of protein mix (10747-012, Invitrogen, Inc.). All samples were then heated at 70°C for 10-minutes. Next, two NuPAGE® gels (1.0 mm x 15-well, 4-12% Bis-Tris, Invitrogen, Inc.) were loaded with 15-µL of sample, and ran in 1x NuPAGE® MES SDS Running

Buffer (20x, Invitrogen, Inc.) using a constant 200-V setting for 40-minutes.

After completing electrophoresis the gels were removed from their plastic cases and the proteins were transferred to a polyvinylidene fluoride (PVDF) membrane using the iBlot® Gel Transfer Device (Invitrogen, Inc.). The membrane was then placed into infrared (IR) compatible blocking buffer (Odyssey®, LI-COR Biosciences) for 1-hour. Next, 1:600 primary antibody dilutions of RhoA (ab54835, Abcam, Cambridge, MA), phosphorylated RhoA (p.RhoA, ab41435, Abcam, Cambridge, MA), and Rac1+Cdc42 (ab18758, Abcam, Cambridge, MA) were prepared in blocking buffer. Membranes were then incubated in primary antibody solution at 4 °C for 24-hours and then washed 3x with 0.1% TWEEN® 20 (Sigma-Aldrich, Inc.) for 10-minutes each. The appropriate infrared dye labeled secondary antibody solutions were prepared at a dilution of 1:2,000 (IRDye®, LI-COR Biosciences, Inc.) for vinculin, GAPDH, and actin in blocking buffer, and membranes were incubated for 1-hour covered from light. The membranes were then rinsed 3x with 0.1% TWEEN® 20 for 10-minutes each. The membranes were then analyzed on an infrared Odyssey machine (LI-COR Biosciences, Inc.) using Odyssey V3.0 software utilizing both 700-nm and 800-nm wavelengths. Protein densitometry measurements were attained by first adjusting the image display curve to remove background, and then the densitometry was measured with a standard rectangular area for each membrane sample. Ratios from the various sample readings were then calculated.

## 4. Results

### 4.1. Silk film surface topography affects cell sheet migration.

Micro-patterned silk films were successfully cast from PDMS molds with both flat and patterned surfaces. SEM imaging revealed that the flat silk film surfaces were free from significant roughness [Figure 1A], and that the correct patterned feature dimensions were produced for surfaces with parallel line surface features [Figure 1B]. In addition, the desired feature depth of 1.5-μm along with consistent feature wall formation was also attained as illustrated by cross sectional imaging analysis [Figure 1F]. Cultured cell sheets appeared to demonstrate healthy and confluent morphologies at 1-day in culture upon both flat [Figure 1B] and patterned [Figure 1E] surfaces. Additional cross-sectional analysis indicated that cells formed adherent contact with both flat [Figure 1C] and patterned silk culture substrates [Figure 1F]. It was also observed that culture cells adhered to the pattern surface and did not contact the entire feature depth as desired.

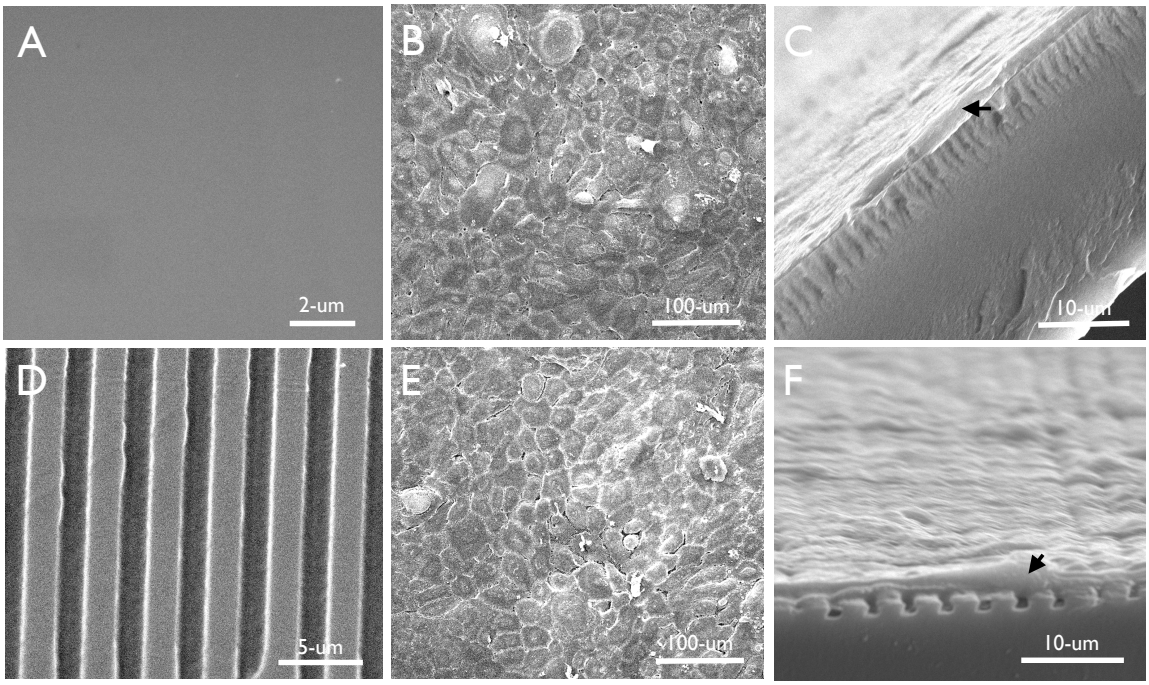


**Figure 1.** (A) Flat silk film surfaces were absent of significant surface roughness, and (B) sustained healthy cell sheet cultures with (C) apparent cellular adherence to the culture surface. (D) Desired lined patterns of 4-μm feature pitch dimensions with 2-μm ridge widths were formed upon the silk film surfaces, and (E) sustained healthy cell sheet cultures with (F) apparent cellular adherence to the top surfaces of the patterned surface topography.

High-density cell suspension droplets were successfully seeded upon the silk film surfaces and glass controls within 2-hours post-seeding. Whole cell sheet dispersion was then characterized upon the various surfaces by measuring the length and width dimensions of each droplet over time [Figure 2A]. After 1-day in culture the measured cell sheet aspect ratio upon patterned

silk film surfaces was increased by 60% on average ($p < 0.05$) when compared to flat silk surfaces and glass controls [Figure 2B]. Analysis indicated that the cell sheets dispersed in a parallel direction along the silk film's patterned feature edge. However, on flat silk and glass surfaces the cell sheets dispersed in a uniform isotropic pattern. Nucleic acid content was assessed to confirm that cell sheet dispersion differences were not primarily a function of culture proliferation. Cell proliferation upon glass controls showed no significant difference when compared to silk surfaces after 1-day in culture, while both flat and patterned silk surfaces demonstrated a significant increase in cell proliferation compared to glass controls after 5-days in culture [Figure 2C]. The results indicate that cell sheets have a greater propensity to proliferate on silk film surfaces when compared to glass controls over time. However, no proliferative difference existed between the flat and patterned silk surfaces indicating that cell sheet dispersion was not a function of cell proliferation.

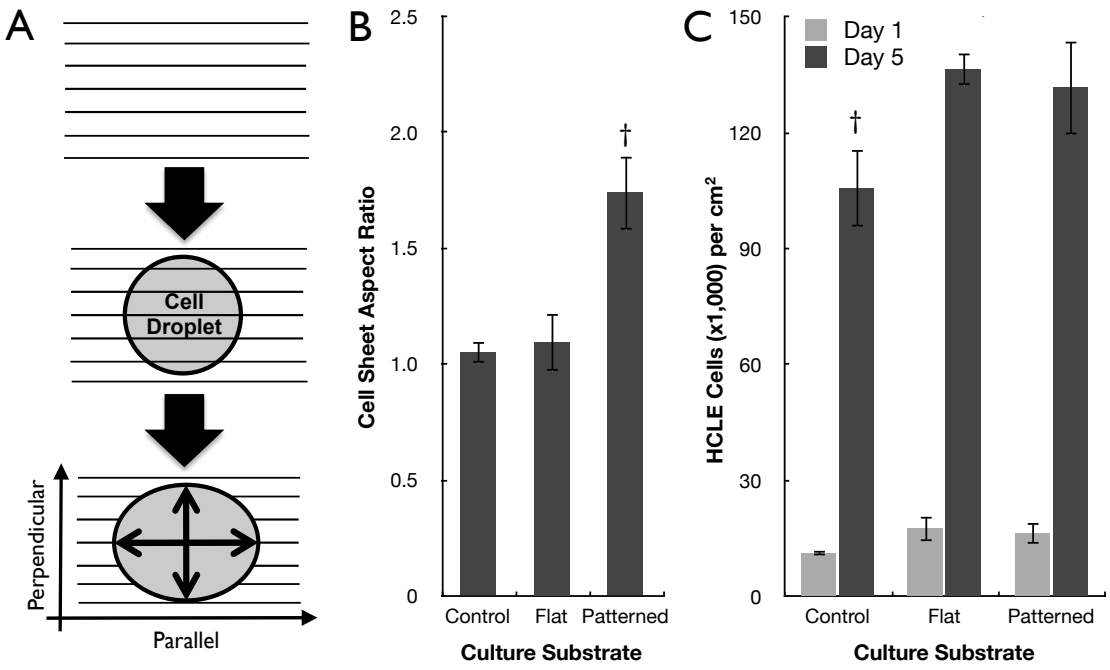


**Figure 2.** (A) Schematic demonstration of a cell droplet forming a collective sheet that disperses parallel to the patterned silk feature axis as measured by the culture length to width aspect ratio, with parallel versus perpendicular directions defined. (B) The aspect ratios of cell sheets on patterned silk surfaces after 1-day in culture ($n = 4$, † indicates $p < 0.05$ when compared other substrates, error bars = SD). (C) Cell proliferation on various surfaces at 1-day and 5-days in culture as quantified by nucleic acid content ($n = 3$, † indicates $p < 0.05$ when compared to other substrates of similar group, error bars = SD).

A dynamic study of collective cell migration was performed using phase-contrast time-lapse imaging of the epithelial cell sheets. Based on the dispersion trends witnessed between flat [Video S1] and patterned surfaces [Video S2-S3] attention was focused on the cell sheet boundary regions. For patterned surfaces with lined features this regions was separated into cells

migrating perpendicular [Video S2] or parallel [Video S3] to the silk film feature edge axis. Flat surfaces were measured in accordance to the major cell sheet migratory axis. When comparing patterned silk film surfaces, cell sheet migration rate was greater for movement parallel to the patterned feature edge [Figure 3A], while limited dispersion occurred perpendicular to the patterned edge direction [Figure 3B]. A detailed observation showed a greater presence of leader cell activity ahead of the migrating cell sheet for cultures moving parallel to the patterned feature axis, while appearing absent for sheets migrating in the perpendicular direction. This was quantified by measuring tortuosity ($\tau$) for the cell sheet migration border regions. Analysis revealed that $\tau$ had a significant 2-fold increase ($n = 4$, $p < 0.05$) for cells migrating in the parallel direction on patterned surfaces when compared to perpendicularly migrating cell sheets and flat surfaces [Figure 3C]. The value for $\tau$ was not significantly different between the other culture surfaces.

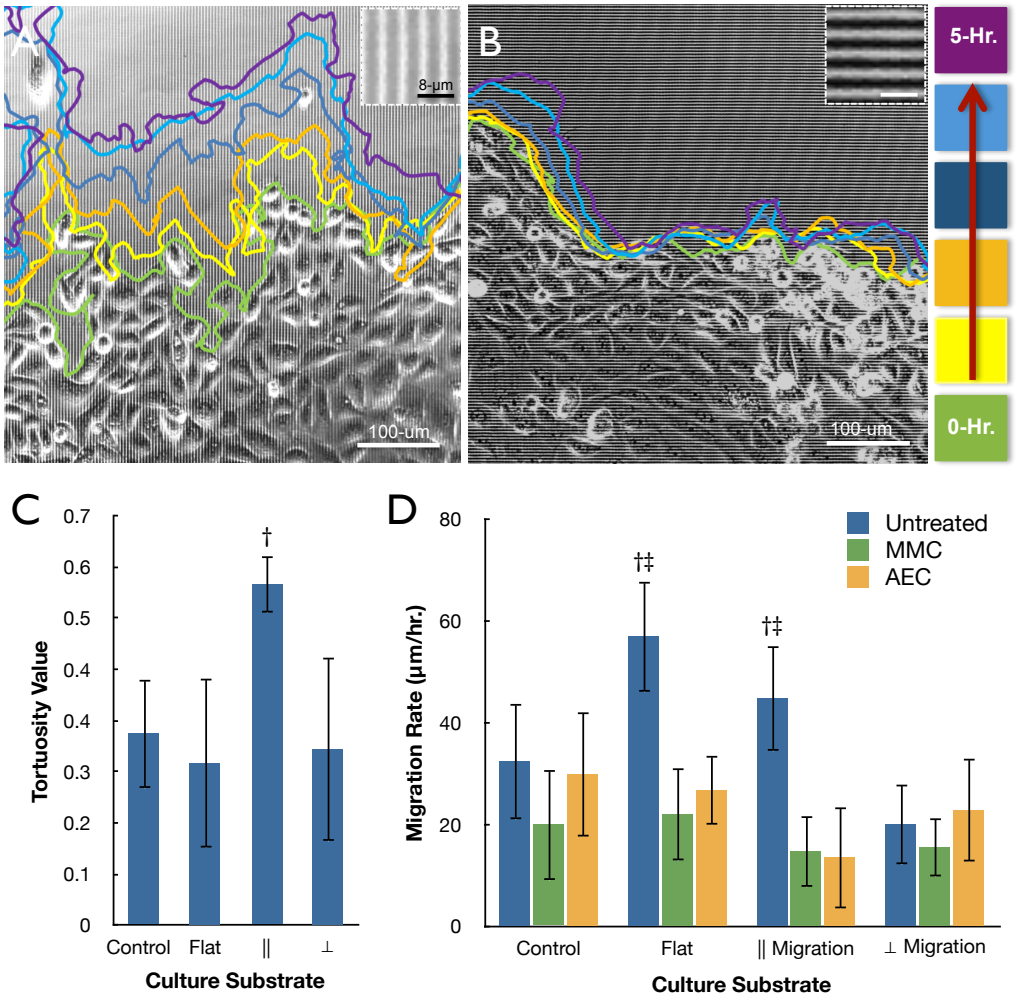


**Figure 3.** Phase contrast images of migrating cell sheets on patterned silk films substrates traveling in the (A) parallel or (B) perpendicular direction of the feature edge as indicated by the inset images of the patterned surfaces, and color tracings are taken at 1-hour increments as indicated by the colored legend. (C) Tortuosity measurements for the migrating cell sheet border on glass controls, flat silk, and patterned silk surfaces accounting for sheet movement parallel (II) and perpendicular (⊥) to the feature edge axis respectively. (D) Cell sheet migration rate on glass controls, flat silk, and II or ⊥ directions to the patterned silk surfaces for untreated, MMC treated, and AEC treated cultures (n = 4, †‡ indicate $p < 0.05$ to the patterned ⊥ direction within groups and between treatment groups respectively, error bars = SD).

Migration rate was assessed over a 10-hour period by comparing cell sheet borders at both 0-hour and 10-hour time points. The distance traveled between these two time points was quantified upon silk culture surfaces and glass controls to determine the affect of surface topography on migration rate. In addition, cell sheets were cultured in the presence of the mitotic inhibitor Mitomycin-C (MMC) or anti-E-cadherin (AEC) antibodies to evaluate the effect of cell proliferation and cell-to-cell interaction respectively. It was found that untreated cells had the highest rate of migration on flat silk surfaces, which was almost twice as fast on average when compared to glass control surfaces ($p < 0.05$, $n = 4$) [Figure 3D]. In addition, a significant over 2-fold drop in migration rate was found on flat surfaces treated with MMC and AEC antibodies respectively ($p < 0.05$, $n = 4$). In addition, a 2-fold drop in migration rate was also observed on patterned silk film surfaces treated with MMC and AEC respectively ($p < 0.05$, $n = 8$).

Sheet migration rate in a direction parallel or perpendicular to the patterned feature edge orientation was also assessed on pattered silk film substrates. It was found that cell sheet movement parallel to the feature edge direction was over 2-fold higher on average ($p < 0.05$, $n = 4$) when compared to cell sheet movement perpendicular to the feature edge direction for untreated cultures [Figure 3D]. The migration rate in the parallel direction for patterned silk surfaces was similar to flat silk surfaces. In addition, a drop in migration rate was shown to exist for cells moving in the parallel direction

when cultures were treated with either MMC or AEC respectively. No change in migration rate was observed for cultures migrating perpendicular to the feature edge for cultures treated with either MMC or AEC respectively.

**4.2. Topographic influence on individual cell alignment and migration.**

The polarity of individual cells upon each surface was characterized through actin staining of the cell sheet cultures upon patterned silk surfaces. The deflected angles from the major length of the cell to the surface pattern feature edge axis were quantified respectively [Figure 4A]. Imaging revealed that the cell polarity was increased at the boundary edges as indicated by a reduction in the measurement of the deviation of cell major axis alignment with the surface pattern axis. Near the boundary edge of the cell droplet this deviation only measured approximately 10°, while within the center region of the droplet this deviation was nearly 45° degrees [Figure 4A]. Thus, cells within the center region of the droplet possessed a random orientation with respect to the patterned feature axis [Figure 4B], while cell orientation demonstrated a polarity along the patterned feature edge at sheet boundary regions [Figure 4C-D]. The individual cell polarity at the sheet edges correlated with the direction of cell migration observed in our time-lapse experiments. Cell sheet migration appeared to be preferred in the parallel direction of the patterned feature axis [Figure 4C]. Correspondingly, cell migration was less preferred for cell sheet migration perpendicular to the patterned feature axis [Figure 4D].

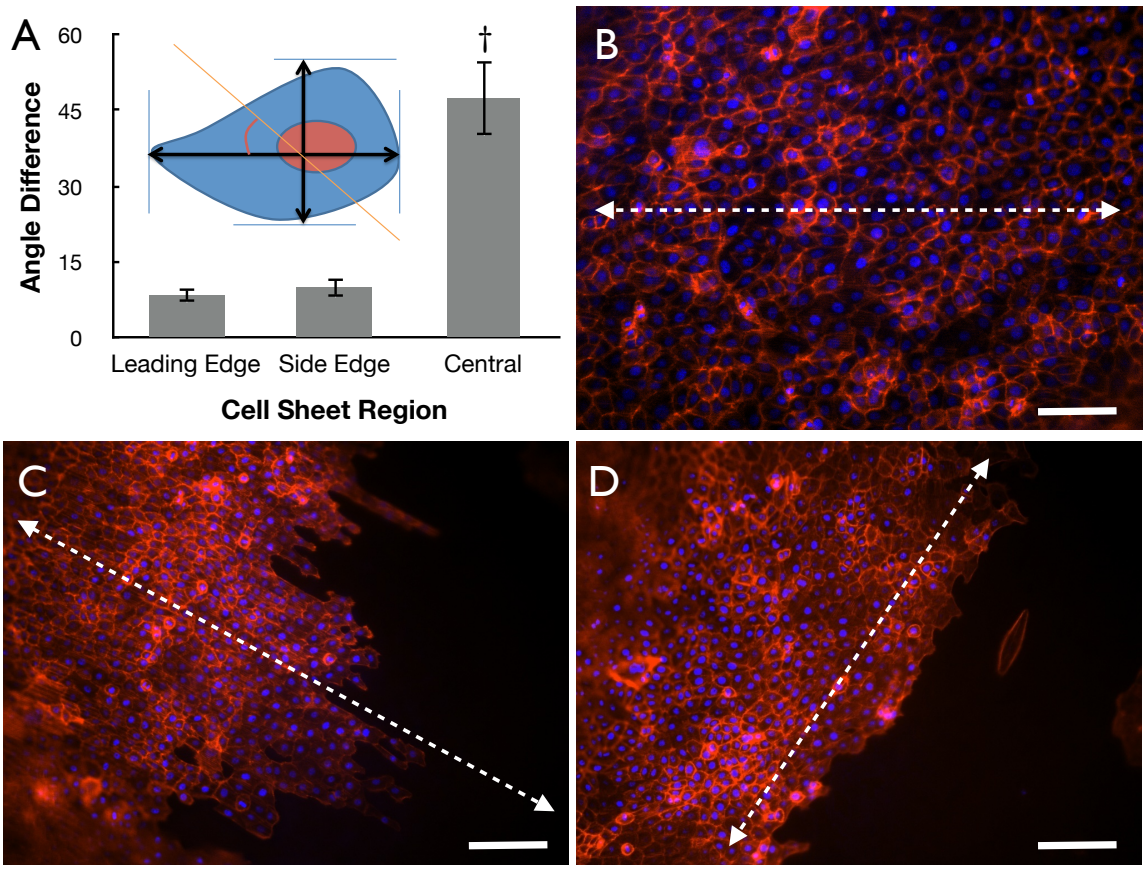


**Figure 4.** (A) Polarity of HCLE cells at the leading edge, side edge, and central regions of the cell sheet, with inset schematic illustrating measurement method (n = 4, † indicates $p < 0.05$, error bars = standard deviations). (B-D) Actin (red) and nuclei (blue) staining of cells located within the (B) central region and (C-D) border regions of the migrating cell sheet with arrows indicating patterned feature edge axis (scale bar = 100-μm).

Migratory paths of individual HCLE cells within the previously observed migrating cell sheets were analyzed for flat and patterned silk film samples and glass control time-lapse videos [Figure 5A-D]. In addition, single cells migrating on patterned silk films in both parallel and perpendicular directions to

the feature edge were also studied. Initial qualitative assessment indicated that cells migrating on flat surfaces and in the parallel direction of the feature edge appeared to move radially away from the cell origin point, while perpendicularly traveling cell trajectories tended to follow the feature edge. Further migratory analysis revealed that total distance and straight distance traveled for single cells was significantly higher ($N = 4$, $n = 20$, $p < 0.05$) on flat silk film surfaces when compared to all other culture substrates [Figure 5E]. However, it was also shown that straight distance traveled was significantly higher for cells moving in the parallel direction to the feature edge when compared to cells moving in the perpendicular direction ($N = 4$, $n = 20$, $p < 0.05$). Tortuosity measurements were significantly lower ($N = 4$, $n = 20$, $p < 0.05$) for single cells migrating on flat and in the parallel direction on patterned silk films when compared to glass controls, and nearly 3-fold higher on average than perpendicularly migrating cells [Figure 5F]. Migration rate was also significantly higher for single cells on flat silk film surfaces when compared to other substrates ($N = 4$, $n = 20$, $p < 0.05$) (Figure 5G). When comparing cell sheet migration efficiency ($\eta$), which is measured as the cell sheet migration velocity over the respective individual cell migration velocity, it was observed that $\eta$ for perpendicularly moving cultures was nearly 3-fold less than cells traveling either on flat silk surfaces or parallel to the topography, and $\eta$ was approximately 2-fold less than glass control surfaces [Figure 5G].

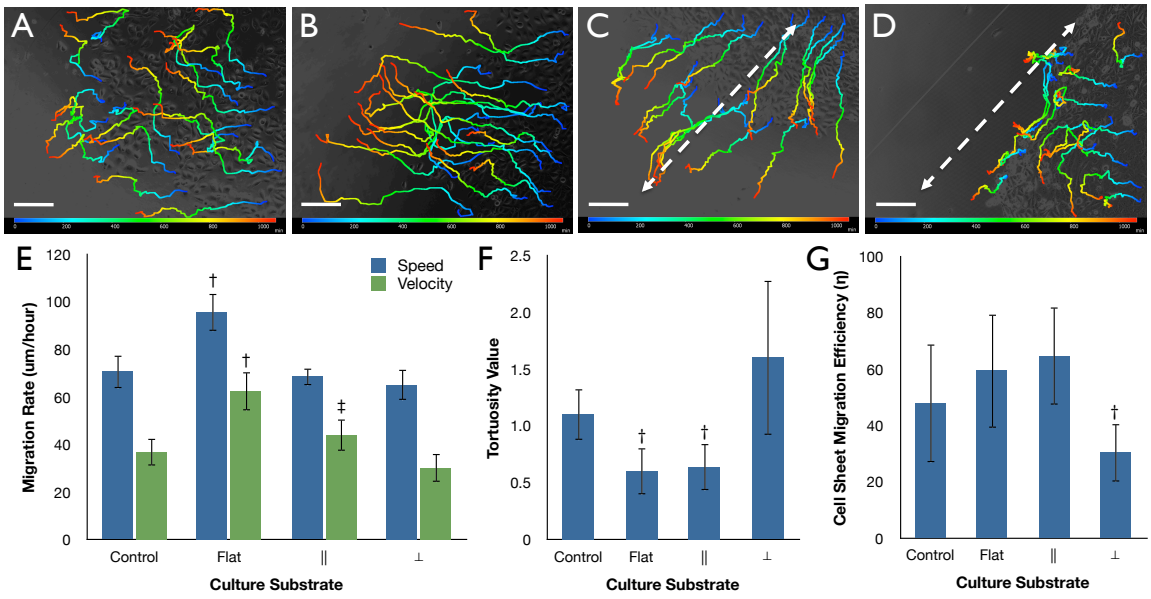


**Figure 5.** Migratory paths of individual HCLE cells on (A) glass control, (B) flat silk, (C) parallel (||) and (D) perpendicular (⊥) movement to the patterned silk topography over a 10-hour culture period (N = 4, n = 20). Color indicates time 0 (blue) to 10-hour (red) time points, and white dashed arrows indicate direction of the silk topography (scale bars = 200-μm). Singular cell migratory measurements for (E) total distance and straight distance measurements († indicates $p < 0.05$ when compared to culture substrates in similar groups, ‡ indicates $p < 0.05$ when compared to ⊥), (F) tortuosity values († indicates $p < 0.05$ when compared to control and ⊥ substrates), and (G) migration rate for singular cellular movement upon various substrates († indicates $p < 0.05$ when compared to all other substrates). (H) Cell sheet migration efficiency (η) for cultures migrating on the various substrates conditions († indicates $p < 0.05$ when compared to all other substrates). Error bars = SD for all graphs.

### 4.3. The effect of silk film surface patterning on cytoskeleton formation.

In order to better understand how cell-surface interactions influence collective

cell migration, further investigation into the distribution of actin and vinculin protein formation was assessed. Initial observations revealed that cell cultures on both glass [Figure 6A] and flat silk film surfaces [Figure 6B] had actin fibril and focal adhesion (FA) formations along the basal cell body periphery. Patterned silk film surfaces appeared to induce alignment of actin fibrils and FA formation within the central region of the cell basal surface localized along the feature edges [Figure 6C]. Aligned features present in cells were located at both the cell sheet border region and internally in the cell sheet. Analysis of vinculin formation upon the various surfaces revealed an over 10-fold increase on average in FA localization within the central basal area of cells cultured upon patterned surfaces when compared to cultures on flat surfaces [Figure 6D]. Actin fibril alignment on the silk film surfaces were further investigated using line scan analysis of single HCLEs within the cell sheet culture. It was seen that actin fibril alignment was not present on flat silk film surfaces [Figure 6E], while directed fibril alignment was observed on the various patterned surfaces [Figure 6F]. The absence of actin fibril formation within the intracellular region was visualized as a U-shape pixel intensity profile after performing a line-scan analysis, while periodic peaks were seen on patterned silk surfaces corresponding with the presence of the feature edges.

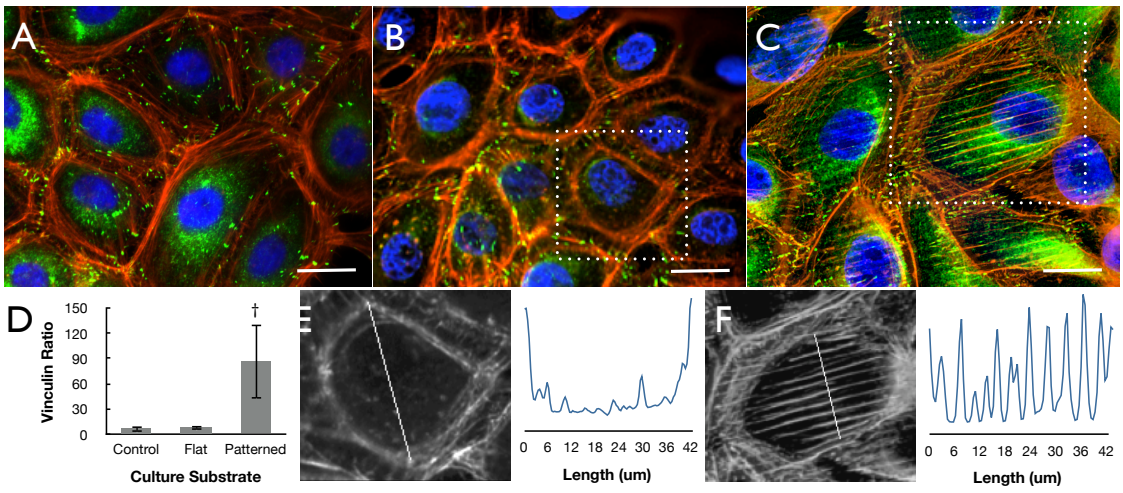


**Figure 6.** Fluorescent microscopy images of HCLE cells on (A) glass, (B) flat silk, and (C) patterned silk surfaces (nuclei - blue, actin – red, and vinculin - green, scale bars = 20-μm). (D) Quantification of intracellular to cellular periphery FA formations as indicated by vinculin staining. Fluorescent images and corresponding line-scan analysis of actin fiber distribution of HCLEs cultured on (E) flat and (F) patterned silk film surfaces, where the inset white line of each image indicates region of analysis.

To better understand the mechanistic basis of guided actin fibril alignment along the patterned silk film feature edge GTPase protein localization was visualized using immunofluorescent microscopy on HCLEs grown on flat and pattern silk films and glass control substrates. Imaging revealed that RhoA, phosphorylated RhoA (P.RhoA), Rac1 and Cdc42 proteins were distributed throughout the cytoplasm for cultures on glass control surfaces [Figure 7A-C] and flat silk film surfaces [Figure 7D-F]. However, on patterned silk films surfaces GTPase proteins were found to concentrate along the feature edge axis [Figure 7G-I]. To assess if this was

primarily a protein localizing or translation effect western blot analysis was undertaken to assess GTPase content for cultures grown on the various surfaces. Results indicated that RhoA, P.RhoA, Rac1, and Cdc42 proteins were isolated in similar quantities from the various culture substrates [Figure 7J-K]], and indicates that the patterned surfaces are inducing a localizing effect.

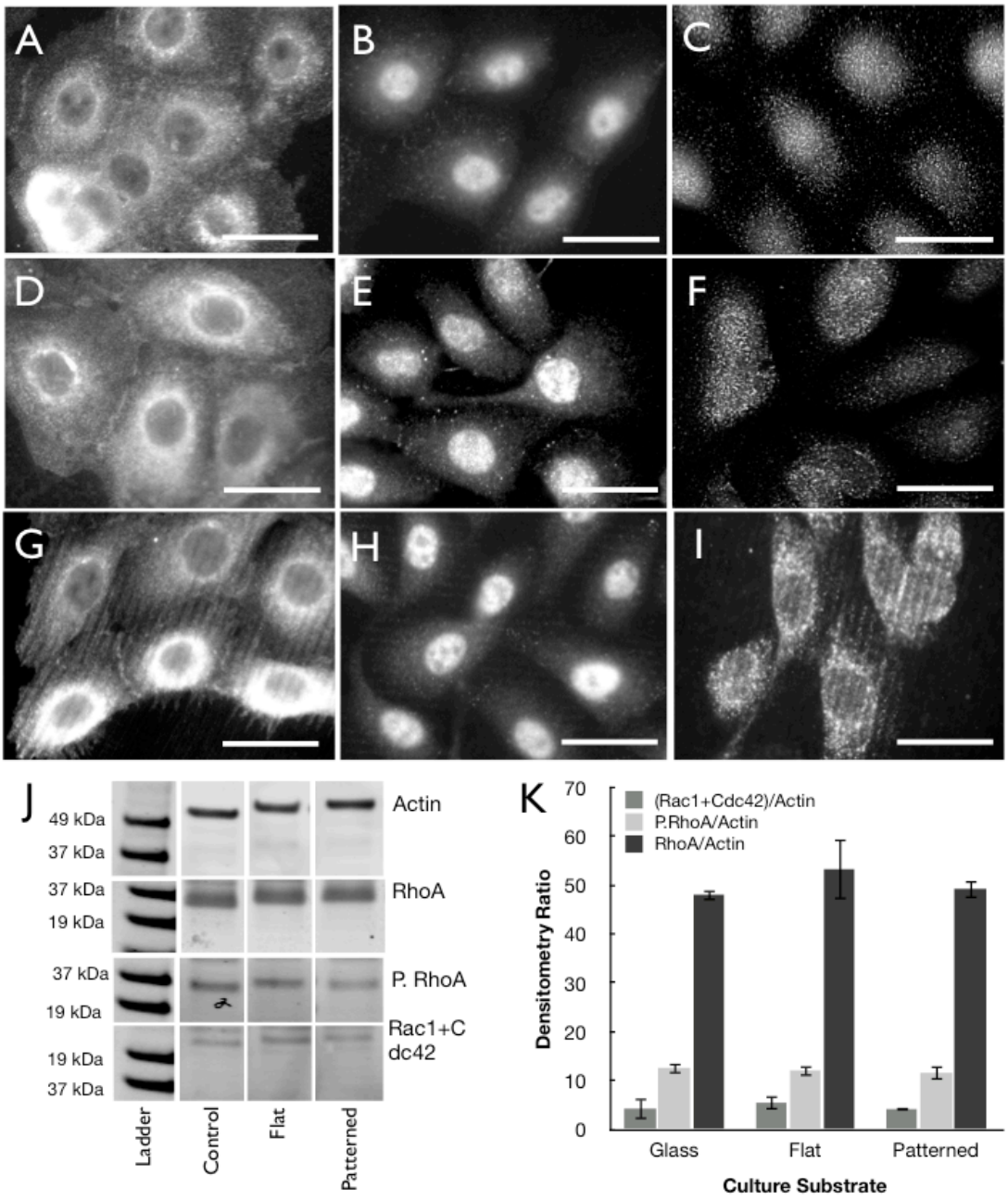


**Figure 7.** Immunofluorescent imaging of RhoA, P.RhoA, and Rac1+Cdc42 antibody binding for (A-C) glass, (D-F) flat silk, and (G-H) patterned silk surfaces respectively. (J) Western blot membrane staining and (K) densitometry results for the various GTPases (n = 3, error bars = SD).

## 5. Discussion

For the first time patterned silk film surfaces were successfully used to evaluate collective corneal epithelial cell migration in vitro. The above results indicate that topographic silk film features may be utilized to influence important cell sheet properties such as migration rate and direction. These effects were observed over multiple dimensional magnitudes from shaping cell sheet geometry to protein localization. The silk film micro-topography was shown to affect overall cell sheet growth. Whole cultures aligned along the feature edge axis on patterned silk surfaces, while growing isotropically on flat silk and glass control surfaces. Such macroscopic effects must be derived from a more fundamental process at the individual cellular level, which was further explored.

Cell sheet migration on flat silk surfaces was twice as fast when compared to both glass control and patterned silk film surfaces. Upon closer analysis it was revealed that a near equal expedited migration rate was found for cells moving in the parallel direction to the patterned feature edge axis, however no expedited migration was shown for cells moving in the respective perpendicular direction. These results infer that HCLE migration rate is impacted by both material makeup and the topographic presence of the silk film substrates. The micro-to-macro effects of epithelial sheet directional alignment appeared to be accomplished through changes in migration rate as dictated by cellular orientation to the patterned feature edge. Epithelial cells

migrating parallel to the feature edge axis were shown to move at a rate 2-3 fold faster than cells moving in a perpendicular direction.

It was observed that epithelial cells located at the cell sheet border tended to elongate along the feature edge. This elongation appeared to accelerate or slow epithelial sheet migration depending if the movement was parallel or perpendicular to the patterned feature edge respectively. When observing HCLEs located in the central region of the sheet such cell elongation was not apparent, thus suggesting cell elongation and alignment are largely a border region effect when there is an absence of surrounding neighbors.

Two of the established forces that influence collective cell sheet migration is mitotic population pressure arising from proliferating cells within the sheet, and also from cell-to-cell contacts that form between leader cells at the border region of the cell sheet (89,173,176,178,179,182). Inhibiting these forces reduced migration rate by half on flat silk surfaces and for parallel cell sheet movement on patterned silk substrates. No effect on cell sheet migration rate was shown to occur for cells moving perpendicular to the lined features. As a result of this discrepancy in migration rate between the two different movement directions in relation to the topography edge axis, it was speculated that a contact guidance force heavily influenced the cell sheet dynamics (84,171).

Observations of single HCLE movement within the sheet revealed

differences in migration rate between the collective group and individual cells making up the sheet. Total distance traveled by singular cells was not affected by the directional approach to the pattern, however the straight distance traveled was decreased for cells traveling perpendicular to the feature edge. As a result singular cells traveling perpendicular to the feature edge moved in a more tortuous path as they are guided along the edge direction instead of moving with the collective cell sheet direction. Most intriguing is the finding that the directional approach to the pattern edge does not affect individual cell migration rate, however singular migration rate is increased in the absence of silk topography.

Singular cells migrate nearly 4-fold faster to their respective cell sheets traveling in the perpendicular direction of the patterned feature edge. These findings infer that the overall effect that each individual cell has on moving the collective sheet is significantly decreased for migration perpendicular to the patterned feature edge. The feature edge acts similar to a guiding track for individual cell migration, in which movement is preferred with the edge as opposed to against it. This guiding track effect on singular cells is amplified at the level of the collective cell sheet where the en masse movement is slowed in the perpendicular direction of the feature edge. In more physically relevant terms, $\eta$ can be defined as the ratio of the cell sheet migration rate that is considered to be useful energy output, over the average individual cell migration rate and taken to be the total energy input for the collective sheet.

Thus, η in a given direction can be controlled through the use of surface topography by modulating the degree of uniformity for directed individual cell movement.

To explore the potential effects that the surface topography is having on individual cells within the collective sheet formation effects on the cytoskeletal where more closely investigated. The HCLE actin cytoskeleton was noticeably affected by the presence of the surface pattern, with significant fibril alignment upon patterned silk film surfaces. Most notably both actin fibrils and cellular focal adhesions (FAs), as indicated from vinculin staining, were found to localize and align in accordance with the pattered feature edge location. Such contact guidance effects on the actin cytoskeleton have been cited for other patterned substrate materials and corneal cell types respectively (21,79,80,82,98). In addition, FA formation was found to occur in the intracellular region for cells grown on patterned surfaces, but largely absent on flat silk film and glass control surfaces. Such results indicate that the presence of the patterned feature topography induces FA formation in vitro and may play a role in affecting cell migration through augmenting cytoskeletal formation (85,183).

To better understand how the presence of the silk surface patterning dictates actin fibril formation a number of GTPase proteins important for actin cytoskeleton formation were observed. GTPase proteins RhoA, Cdc42, and Ras1 are important in actin fibril formation and protein recycling

(21,93,177,184,185). All three proteins were found to preferentially localize in the regions of the cell correlating to the location of the patterned surface features, however they were centrally distributed on flat surfaces. In addition, overall protein content remained consistent on all culture substrates thus suggesting surface patterns primarily promote a protein localizing effect. These results tend to infer that the actin fibril formation would preferentially take place in these regions of high GTPase activity, thus the pattern surface may be acting to guide actin fibril assembly through a protein localizing effect. The localizing effect of the pattern surface upon important cytoskeletal forming proteins will greatly dictate cytoskeletal dynamics, and as a result impact the cell sheet migration rate through directing individual cell movement.

The addition of patterned features creates migrating cell sheets that are more compact in nature and have border region leader cells elongating in the feature edge direction. In finite regions where the pattern edge is located there is an increased preference for actin fibril and FA formation. As in the case of cells moving perpendicular to lined feature edge cell migration is more likely to be directed along the continuous feature edge region where protein localization is occurring, and as a result there is an inhibition in directional selection for perpendicular movement of singular cells. In contrast, cells moving parallel to the feature direction have a more limited number of locations that enhance protein localization, and ultimately this reduction in localizing edge region may inhibit directional selection for movement less.

This effect manifests itself at the single cell level where individual cells will be preferentially guided along the parallel direction of the surface feature edge axis. As a result the η in a given direction is largely dictated by the collective sum of preferred individual cell movement. This preferred directional cell movement is largely dictated by edge feature presence, mitotic population pressure, and leader cell activity. On the other hand cell sheets on flat silk surfaces appear to move in a less compacted and isotropic pattern upon the culture surface. The absence of surface features does not influence protein localization and as a result actin and FA formation appear to remain isolated to the cell periphery. Singular cells travel faster and less compactly due to the lack of directional guidance, which results in a uniform η in all directions as dictated by mitotic population pressure and leader cell activity. A summary illustration of these findings is shown in Figure 8.

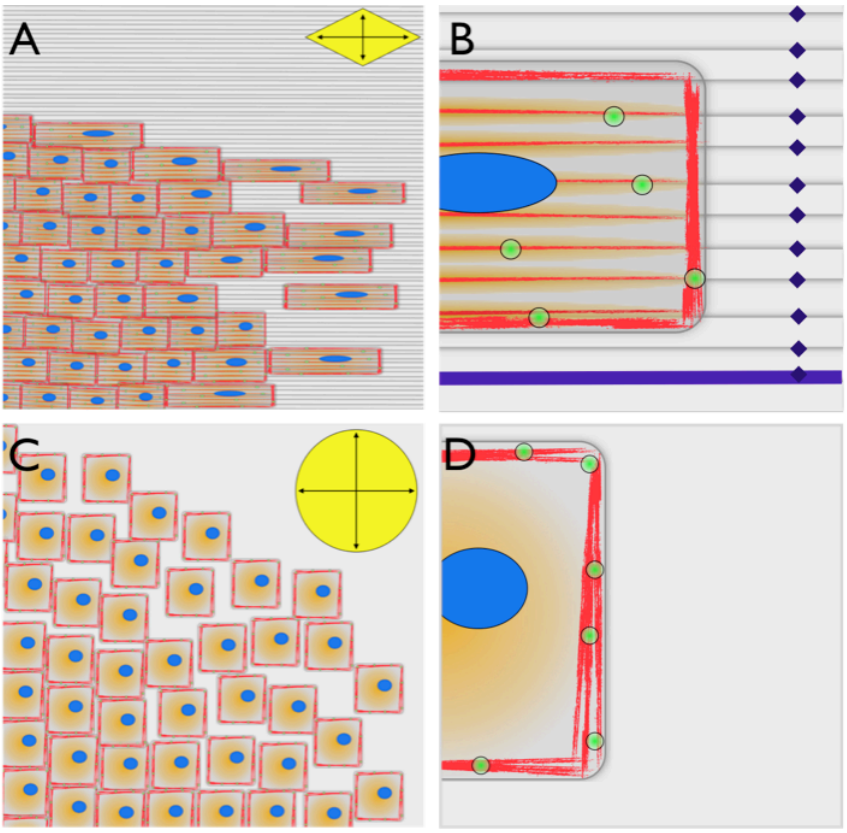


**Figure 8.** Schematic representations of cell sheet migration on (A-B) patterned and (C-D) flat silk film surfaces. (A) Cell sheet migration on patterned silk surfaces was compact in nature with leading border cells elongating in the parallel direction of the patterned feature edge. Migration rate was 2-fold higher in the parallel direction of the feature edge when compared to perpendicular movement direction as indicated by the vectors contained in the yellow diamond. (B) Actin fibril (red), FA (green), and GTPase (orange) proteins were found to preferentially localize along the surface feature edges as indicated in purple. (C) In contrast, cell sheet migration on flat silk film substrates was less compact with leading cells maintain a normal cuboidal morphology, and migration rate was similar in all directions. (D) Actin fibrils and FAs were found to primarily localize at the cellular basal periphery region with GTPase proteins localizing uniformly within the central region of the cell.

## 6. Conclusion

Patterned silk films greatly affect cell migration and cytoskeleton dynamics in vitro. The inhibition of HCLE cell sheet migration upon a patterned silk film surface appears to be derived from the formation of cytoskeletal proteins upon the various surfaces. The presence of feature edge topography plays a significant role in localizing actin fibrils, FAs, and GTPases. As a result there appears to be increased formation of the cytoskeleton structure at these feature edge locations. Most notably, the addition of the surface topography plays an important role in dictating cell sheet migration rate by directing individual cell migration direction along the feature edge axis through contact guidance effects. Future work may build off these results to design cell surfaces that may more efficiently direct cell sheet migration, with the hope of utilizing such topography to develop clinically relevant devices to enhance wound healing after trauma or contain cell migration to confined regions within the body.

CHAPTER 8

# Conclusion

Silk biomaterials are emerging as a multifunctional choice biopolymer that is able to meet the needs of an array of biomedical challenges. The diversity of the material's use rests in the ability to controllably alter the biomaterial's protein secondary structure and transform an array of material property characteristics. By its nature silk fibroin protein is an engineering grade biopolymer, which can be processed into a customized form to serve a specific purpose. This dissertation highlights the use of silk films as one geometrical configuration that can be produced from the solubilized regenerated silk solution. Although films in general may seem somewhat generally lackluster and two-dimensional, the published findings here demonstrate how the use of such structures can be used over a wide range of dimensional scales and scientific understanding. Silk film substrates represent an opportunity to use a highly controlled system to better understand underlying biological principals from protein interaction to epithelial tissue formation.

Controlling the water content of the silk film can be used to fundamentally alter a variety of material properties such as transparency, oxygen permeability, swellability, dissolution rate, and tensile modulus (40,49,52). This is accomplished because water acts as a lubricating entity within the bulk material, and allows for the movement of the silk protein chains

to form more thermodynamically stable secondary structures such as α-helices ad β-sheets (31,32,43,51,52). A newly formed silk film is a dehydrated aggregation of protein chains, which will rearrange through the introduction of a solvent lubricant such as water or methanol (40,110). The process of water-annealing, which is the introduction of controlled water vapor content to the silk film, can be used to control silk material properties through inducing a relatively slow formation of silk secondary structures (32,186). In addition, the relatively slow protein structure transition allows for greater silk film transparency and the ability to modify material solubility (52). These specific properties enable for the production of biomaterial substrates that are ideal for both in vitro characterization and ocular surface applications.

Insoluble silk films can be prepared for cell culture in a reproducible fashion that allows for large sample sets due to their straightforward production methodology (48). These substrates can be successfully sterilized and seeded with a variety of cell types. Of particular interest to ocular surface reconstruction is the ability to culture confluent layers of stratified epithelium tissues. The use of silk films to develop stratified epithelial layers is comparable to the current standard amniotic membrane (187). Amniotic membrane is from a donated tissue source, the placenta of a birthing woman, and has been found to be useful in ocular surface reconstruction (64,70). However, amnion has a number of drawbacks such as the potential for viral transmission, accessibility problems, material handleability, expense, and

refrigeration requirements (70,72). The use of silk bypasses these issues and offers a novel alternative for use as an ocular surface repair material.

Because of their highly biocompatible nature silk film designed to induce a specific response in vitro can be rapidly translated for in vivo experiments (9,10,12,34). As a result silk films have the potential to more effectively translate basic research to clinical use. The silk film material properties were designed to produce a silk film that would self-adhere to the corneal surface and dissolve after application. The ability of the silk film to enhance healing was proven using a rabbit cornea injury model where the epithelium is debrided, the silk film is placed on top of the wound site, and healing is monitored over time. By optimizing the silk film residence time on the injured cornea surface there was an enhancement in healing rate over untreated groups. However, if the residence time of the silk film is too short there is no enhanced effect, and alternatively if the residence time is too long there is an inhibition of corneal healing. These results indicate how controlling silk film material properties can be used directly to affect a clinically relevant outcome.

On a basic scientific level silk film biomaterials offer a number of interesting properties that can be harnessed to assess cell response. One specific insight is better understanding the impact of surface topography on cellular response. Silk films have the unique feature of possessing the ability to be surface patterned at the nanoscale (25). The use of topography impacts

cell response at a fundamental level of cytoskeleton organization and mobility. This is especially important for epithelial cells, which actively produce their own topographically rich basement membrane surfaces in situ (57). The addition of curvature to topographic features also influences fundamental cell properties such as initial cell attachment and cell body spreading. Focal adhesion formation is directed to the topography edge, and important cytoskeleton forming proteins, such as GTPases (185), also localize to these regions. As a result the cytoskeleton formation is directed to form along the edge region. In this way the use of surface topography is a non-chemical way to introduce a significant effect upon cells in culture.

Such seemingly subtle effects manifest themselves in significant ways when cells are seen as a collective sheet of tissue. This is especially important in developing new materials for ocular surface repair where surface topography could be designed to promote epithelial healing. In situ, epithelial cells move in a collective sheet across a wound site. Surface topography guides individual cells more effectively in a given direction. As a result, surface topography can be designed to promote efficient cell sheet movement in one direction and inhibited in another direction on a given growth substrate. As a result, epithelial tissue growth can be directionally guided by an engineered surface topography. Further work is needed to translate patterned surfaces that are optimized to guide cells across a given wound site to the clinical setting.

By altering silk fibroin protein secondary structure through the use of water-based methods silk films biomaterials have proved to be an adaptable material form for scientific exploration and translation clinical science. Through engineering design silk film biomaterials can be produced with customized material properties for a given application. Of immediate consideration is the use of these materials for use in ocular surface repair due to their high level of transparency and inherent biocompatibility. However, continued efforts will need to focus on better understanding how the material can be more finely controlled through new and innovative processing methods. Such findings will lead to greater adaptability of the material for a given application in both ophthalmology and the biomedical sector as a whole. Taken together silk films are a dynamic system that can be utilized for scientific exploration from the molecular to clinical dimension.

REFERENCES


1. Shear W, Palmer J, Coddington J, Bonamo P. A Devonian spinneret: early evidence of spiders and silk use. Science. 1989;246(4929):479.

2. Kaplan D. Silk polymers. An American Chemical Society Publication; 1994. p. 370.

3. Shao Z, Vollrath F. Materials: Surprising strength of silkworm silk. Nature. 2002;418(6899):741.

4. Rockwood DN, Preda RC, Yucel T, Wang X, Lovett ML, Kaplan DL. Materials fabrication from Bombyx mori silk fibroin. Nature protocols. 2011 Sep. 22;6(10):1612–31.

5. Minoura N, Aiba S, Higuchi M, Gotoh Y. Attachment and Growth of Fibroblast Cells on Silk Fibroin. Biochemical and …. 1995.

6. Altman G, Diaz F, Jakuba C, Calabro T, Horan R, Chen J, et al. Silk-based biomaterials. Biomaterials. 2003;24(3):401–16.

7. Vepari C, Kaplan D. Silk as a biomaterial. Progress in Polymer Science. 2007;32(8-9):991–1007.

8. Omenetto F, Kaplan D. New Opportunities for an Ancient Material. Science. 2010;329(5991):528.

9. Meinel L, Hofmann S, Karageorgiou V, Kirker-Head C, McCool J, Gronowicz G, et al. The inflammatory responses to silk films in vitro and in vivo. Biomaterials. 2005;26(2):147–55.

10. Fini M, Motta A, Torricelli P, Giavaresi G. ScienceDirect.com - Biomaterials - The healing of confined critical size cancellous defects in the presence of silk fibroin hydrogel. Biomaterials. 2005.

11. Pra ID, Freddi G, Minic J, Chiarini A. ScienceDirect.com - Biomaterials - De novo engineering of reticular connective tissue in vivo by silk fibroin nonwoven materials. Biomaterials. 2005.

12. Huang W, Begum R, Barber T, Ibba V, Tee NCH, Hussain M, et al. Regenerative potential of silk conduits in repair of peripheral nerve injury in adult rats. Biomaterials. 2012 Jan.;33(1):59–71.

13. Etienne O, Schneider A, Kluge JA, Bellemin-Laponnaz C, Polidori C, Leisk GG, et al. Soft tissue augmentation using silk gels: an in vitro and

in vivo study. Journal of periodontology. Am Acad Periodontology; 2009;80(11):1852–8.

14. Mandal B, Grinberg A, Gil ES. High-strength silk protein scaffolds for bone repair. 2012.

15. Wang Y, Blasioli D, Kim H, Kim H, Kaplan D. Cartilage tissue engineering with silk scaffolds and human articular chondrocytes. Biomaterials. 2006;27(25):4434–42.

16. Yang Y, Yuan X, Ding F, Yao D, Gu Y, Liu J, et al. Repair of rat sciatic nerve gap by a silk fibroin-based scaffold added with bone marrow mesenchymal stem cells. Tissue Engineering Part A. 2011 Sep.;17(17-18):2231–44.

17. Park S-H, Gil E-S, Cho H, Mandal BB, Tien LW, Min B-H, et al. Intervertebral Disk Tissue Engineering Using Biphasic Silk Composite Scaffolds. Tissue Engineering Part A. Mary Ann Liebert, Inc. 140 Huguenot Street, 3rd Floor New Rochelle, NY 10801 USA; 2012 Mar.;18(5-6):447–58.

18. Patra C, Talukdar S, Novoyatleva T, Velagala S. Silk protein fibroin from Antheraea mylitta for cardiac tissue engineering 10.1016/j.biomaterials.2011.12.036 : Biomaterials | ScienceDirect.com. Biomaterials. 2012.

19. Altman AM, Gupta V, Ríos CN, Alt EU, Mathur AB. Adhesion, migration and mechanics of human adipose-tissue-derived stem cells on silk fibroin–chitosan matrix. Acta Biomaterialia. 2010 Apr.;6(4):1388–97.

20. Yan L-P, Oliveira JM, Oliveira AL, Caridade SG, Mano JF, Reis RL. Macro/microporous silk fibroin scaffolds with potential for articular cartilage and meniscus tissue engineering applications. Acta Biomaterialia. 2012 Jan.;8(1):289–301.

21. Lawrence B, Marchant J, Pindrus M, Omenetto F, Kaplan D. Silk film biomaterials for cornea tissue engineering. Biomaterials. 2009;30(7):1299–308.

22. Harkin DG, George KA, Madden PW, Schwab IR, Hutmacher DW, Chirila TV. Silk fibroin in ocular tissue reconstruction. Biomaterials. Elsevier; 2011.

23. Kim U, Park J, Kim HJ, Wada M. Three-dimensional aqueous-derived

biomaterial scaffolds from silk fibroin. Biomaterials. 2005.

24. Kalluri R. Angiogenesis: Basement membranes: structure, assembly and role in tumour angiogenesis. Nat Rev Cancer. 2003 Jun.;3(6):422–33.

25. Lawrence B, Cronin-Golomb M, Georgakoudi I, Kaplan D, Omenetto F. Bioactive silk protein biomaterial systems for optical devices. Biomacromolecules. 2008;9(4):1214–20.

26. Lawrence B, Omenetto F, Chui K, Kaplan D. Processing methods to control silk fibroin film biomaterial features. Journal of materials science. 2008;43(21):6967–85.

27. Rockwood D, Preda RC, Yucel T, Wang X, Lovett ML, Kaplan DL. Materials Fabrication from Bombyx mori Silk Fibroin. Nature protocols. 2011;In press.

28. Desjardins M. Phagocytosis: at the crossroads of innate and adaptive immunity. Annu. Rev. Cell Dev. Biol. 2005.

29. Onuki Y, Bhardwaj U. A review of the biocompatibility of implantable devices: current challenges to overcome foreign body response. J Diabetes Sci …. 2008.

30. Chen X, Shao Z, Marinkovic N, Miller L, Zhou P, Chance M. Conformation transition kinetics of regenerated Bombyx mori silk fibroin membrane monitored by time-resolved FTIR spectroscopy. Biophysical Chemistry. 2001;89(1):25–34.

31. Hu X, Kaplan D, Cebe P. Determining beta-sheet crystallinity in fibrous proteins by thermal analysis and infrared spectroscopy. Macromolecules. 2006;39(18):6161–70.

32. Hu X, Shmelev K, Sun L, Gil E-S, Park S-H, Cebe P, et al. Regulation of Silk Material Structure by Temperature-Controlled Water Vapor Annealing. Biomacromolecules. 2011 May 9;12(5):1686–96.

33. Mo C, Wu P, Chen X, Shao Z. Near-infrared characterization on the secondary structure of regenerated Bombyx mori silk fibroin. Applied spectroscopy. 2006;60(12):1438–41.

34. Wang Y, Rudym D, Walsh A, Abrahamsen L, Kim H, Kim H, et al. In vivo degradation of three-dimensional silk fibroin scaffolds. Biomaterials. 2008;29(24-25):3415–28.

35. Kim D, Viventi J, Amsden J, Xiao J, Vigeland L, Kim Y, et al. Dissolvable films of silk fibroin for ultrathin conformal bio-integrated electronics. Nature Materials. 2010.

36. König H, Kilbinger A. Learning from Nature: β-Sheet-Mimicking Copolymers Get Organized. Angewandte Chemie International Edition. 2007;46(44):8334–40.

37. Jin H, Kaplan D. Mechanism of silk processing in insects and spiders. Nature. 2003;424(6952):1057–61.

38. Nanoconfinement controls stiffness, strength and mechanical toughness of β-sheet crystals in silk. 2010;9(4):359–67.

39. Gupta M, Khokhar S, Phillips D, Sowards L, Drummy L, Kadakia M, et al. Patterned silk films cast from ionic liquid solubilized fibroin as scaffolds for cell growth. Langmuir. 2007;23(3):1315–9.

40. Jin H, Park J, Karageorgiou V, Kim U, Valluzzi R, Cebe P, et al. Water-Stable Silk Films with Reduced β-Sheet Content. Advanced Functional Materials. 2005;15(8):1241–7.

41. Lu Q, Hu X, Wang X, Kluge J, Lu S, Cebe P. Water-insoluble silk films with silk I structure. Acta Biomaterialia. 2010.

42. Agarwal N, Hoagland D, Farris R. Effect of moisture absorption on the thermal properties of Bombyx mori silk fibroin films. Journal of Applied Polymer Science. 1997;63(3):401–10.

43. Motta A, Fambri L, Migliaresi C. Regenerated silk fibroin films: thermal and dynamic mechanical analysis. Macromolecular Chemistry and Physics. 2002;203(10-11):1658–65.

44. Horan R, Antle K, Collette A, Wang Y, Huang J, Moreau J, et al. In vitro degradation of silk fibroin. Biomaterials. 2005;26(17):3385–93.

45. Jin H, Park J, Valluzzi R, Cebe P, Kaplan D. Biomaterial films of Bombyx mori silk fibroin with poly (ethylene oxide). Biomacromolecules. 2004;5(3):711–7.

46. Tretinnikov O, Tamada Y. Influence of casting temperature on the near-surface structure and wettability of cast silk fibroin films. Langmuir. 2001;17(23):7406–13.

47. Omenetto F, Kaplan D. A new route for silk. Nature Photonics.

2008;2(11):641–3.

48. Lawrence BD, Pan Z, Weber MD, Kaplan DL, Rosenblatt MI. Silk Film Culture System for in vitro Analysis and Biomaterial Design. JoVE. 2012;In press(62):e3646.

49. Hu X, Kaplan D, Cebe P. Effect of water on the thermal properties of silk fibroin. Thermochimica Acta. 2007;461(1-2):137–44.

50. Pyda M, Hu X, Cebe P. Heat Capacity of Silk Fibroin Based on the Vibrational Motion of Poly(amino acid)s in the Presence and Absence of Water. Macromolecules. American Chemical Society; 2008 Jul.;41(13):4786–93.

51. Hu X, Kaplan D, Cebe P. Dynamic Protein– Water Relationships during β-Sheet Formation. Macromolecules. 2008.

52. Lawrence BD, Wharram S, Kluge JA, Leisk GG, Omenetto FG, Rosenblatt MI, et al. Effect of Hydration on Silk Film Material Properties. Macromolecular Bioscience. 2010 Apr. 8;10(4):393–403.

53. Wang X, Kim H, Xu P, Matsumoto A, Kaplan D. Biomaterial coatings by stepwise deposition of silk fibroin. Langmuir. 2005;21(24):11335–41.

54. Chirila T, Barnard Z, Harkin D, Schwab I, Hirst L. Bombyx mori silk fibroin membranes as potential substrata for epithelial constructs used in the management of ocular surface disorders. Tissue Engineering Part A. 2008;14(7):1203–11.

55. Harris D. (D) Routes of delivery: Case studies::(7) Ocular delivery of peptide and protein drugs. Advanced Drug Delivery Reviews. 1992;8(2-3):331–9.

56. Cintron C, Covington H, Kublin C. Morphogenesis of rabbit corneal stroma. INVESTIGATIVE OPHTHALMOLOGY & VISUAL SCIENCE. 1983;24(5):543.

57. Abrams GA, Bentley E, Nealey PF, Murphy CJ. Electron microscopy of the canine corneal basement membranes. Cells Tissues Organs. 2002 Jan. 1;170(4):251–7.

58. Whitcher J, Srinivasan M, Upadhyay M. Corneal blindness: a global perspective. Bulletin of the World Health Organization. 2001;79:214–21.

59. Cutler T. Corneal epithelial disease. The Veterinary Clinics of North America. Equine …. 2004.

60. Yiu S, Thomas P, Nguyen P. Ocular surface reconstruction: recent advances and future outlook. Current Opinion in Ophthalmology. 2007;18(6):509.

61. Boulton M, Albon J. Stem cells in the eye. Int. J. Biochem. Cell Biol. 2004 Apr.;36(4):643–57.

62. Streilein J. Ocular immune privilege: therapeutic opportunities from an experiment of nature. Nature Reviews Immunology. 2003;3(11):879–89.

63. Pellegrini G, Traverso CE, Franzi AT, Zingirian M, Cancedda R, De Luca M. Long-term restoration of damaged corneal surfaces with autologous cultivated corneal epithelium. The Lancet. 1997 Apr.;349(9057):990–3.

64. Maharajan V, Shanmuganathan V, Currie A, Hopkinson A, Powell Richards A, Dua H. Amniotic membrane transplantation for ocular surface reconstruction: indications and outcomes. Clinical & Experimental Ophthalmology. 2007;35(2):140–7.

65. Han B, Schwab I, Madsen T, Isseroff R. A fibrin-based bioengineered ocular surface with human corneal epithelial stem cells. Cornea. 2002;21(5):505.

66. Griffith M, Hakim M, Shimmura S, Watsky M, Li F, Carlsson D, et al. Artificial human corneas: scaffolds for transplantation and host regeneration. Cornea. 2002;21:S54.

67. Lloyd A, Faragher R, Denyer S. Ocular biomaterials and implants. Biomaterials. 2001;22(8):769–85.

68. Benjamin W, Cappelli Q. Oxygen permeability (Dk) of thirty-seven rigid contact lens materials. Optometry & Vision Science. 2002;79(2):103.

69. Dua H, Gomes J, King A, Maharajan V. The amniotic membrane in ophthalmology* 1. SURVEY OF OPHTHALMOLOGY. 2004;49(1):51–77.

70. Liu J, Sheha H, Fu Y, Liang L, Tseng S. Update on amniotic membrane transplantation. Expert Review of Ophthalmology. 2010;5(5):645–61.

71. Tseng S, Espana E, Kawakita T, Pascuale M, Liu T, Cho T, et al. How does amniotic membrane work? The Ocular Surface. 2004;2(3):177–87.

72. Gomes J, Romano A, Santos M, Dua H. Amniotic membrane use in ophthalmology. Current Opinion in Ophthalmology. 2005;16(4):233.

73. Zakaria N, Koppen C, Van Tendeloo V, Berneman Z, Hopkinson A, Tassignon M-J. Standardized Limbal Epithelial Stem Cell Graft Generation and Transplantation. Tissue Engineering Part C: Methods. Mary Ann Liebert, Inc. 140 Huguenot Street, 3rd Floor New Rochelle, NY 10801 USA; 2010 Oct.;16(5):921–7.

74. Hopkinson A, McIntosh R, Tighe P, James D, Dua H. Amniotic membrane for ocular surface reconstruction: donor variations and the effect of handling on TGF-{beta} content. INVESTIGATIVE OPHTHALMOLOGY & VISUAL SCIENCE. 2006;47(10):4316.

75. Saw V, Minassian D, Dart J, Ramsay A, Henderson H, Warwick R, et al. Amniotic membrane transplantation for ocular disease: a prospective evaluation of the first 233 cases from the UK user group. British Medical Journal. 2007.

76. Higa K, Shimmura S, Kato N, Kawakita T, Miyashita H, Itabashi Y, et al. Proliferation and Differentiation of Transplantable Rabbit Epithelial Sheets Engineered with or without an Amniotic Membrane Carrier. INVESTIGATIVE OPHTHALMOLOGY & VISUAL SCIENCE. 2007 Feb. 1;48(2):597–604.

77. Gimeno F, Lavigne V, Gatto S, Croxatto J. Advances in corneal stem-cell transplantation in rabbits with severe ocular alkali burns. Journal of Cataract & …. 2007.

78. Bettinger CJ, Langer R, Borenstein JT. Engineering Substrate Topography at the Micro-and Nanoscale to Control Cell Function. Angewandte Chemie International Edition. Wiley Online Library; 2009;48(30):5406–15.

79. Karuri N, Liliensiek S, Teixeira A, Abrams G, Campbell S, Nealey P, et al. Biological length scale topography enhances cell-substratum adhesion of human corneal epithelial cells. Journal of cell science. 2004;117(Pt 15):3153.

80. Diehl K, Foley J, Nealey P, Murphy C. Nanoscale topography modulates corneal epithelial cell migration. Journal of Biomedical

Materials Research Part A. 2005;75(3):603–11.

81. Chen C, Mrksich M, Huang S, Whitesides G, Ingber D. Geometric control of cell life and death. Science. 1997;276(5317):1425.

82. Kilian K, Bugarija B, Lahn B. Geometric cues for directing the differentiation of mesenchymal stem cells. Proceedings of the …. 2010.

83. Dunn G, Brown A. Alignment of fibroblasts on grooved surfaces described by a simple geometric transformation. J Cell Sci. 1986;83(313):40.

84. Meyle J, Gültig K, Brich M, Hämmerle H. Contact guidance of fibroblasts on biomaterial surfaces. Journal of Materials …. 1994.

85. Wang N, Tytell JD, Ingber DE. Mechanotransduction at a distance: mechanically coupling the extracellular matrix with the nucleus. Nat Rev Mol Cell Biol. 2009 Jan.;10(1):75–82.

86. Biggs M, Richards R, Dalby M. Nanotopographical modification: a regulator of cellular function through focal adhesions. … : Nanotechnology. 2010.

87. Abrams G, Schaus S, Goodman S, Nealey P, Murphy C. Nanoscale topography of the corneal epithelial basement membrane and Descemet's membrane of the human. Cornea. 2000;19(1):57.

88. Boudreau N, Werb Z. Suppression of apoptosis by basement membrane requires three-dimensional tissue organization and withdrawal from the cell cycle. 1996.

89. Rørth P. Collective cell migration. Annual Review of Cell and Developmental. Annual Reviews; 2009;25:407–29.

90. Rajnicek A, Foubister L, McCaig C. Alignment of corneal and lens epithelial cells by co-operative effects of substratum topography and DC electric fields. Biomaterials. 2008;29(13):2082–95.

91. Karuri N, Liliensiek S, Teixeira A, Abrams G, Campbell S, Nealey P, et al. Biological length scale topography enhances cell-substratum adhesion of human corneal epithelial cells. Journal of cell science. 2004;117(Pt 15):3153.

92. Doane K, Babiarz J, Fitch J, Linsenmayer T, Birk D. Collagen fibril

assembly by corneal fibroblasts in three-dimensional collagen gel cultures: Small-diameter heterotypic fibrils are deposited in the absence of keratan sulfate proteoglycan* 1. Experimental Cell Research. 1992;202(1):113–24.

93. Vrana E, Builles N, Hindie M, Damour O, Aydinli A, Hasirci V. Contact guidance enhances the quality of a tissue engineered corneal stroma. Journal of Biomedical Materials Research Part A. 2008;84(2):454–63.

94. Wu J, Du Y, Watkins SC, Funderburgh JL, Wagner WR. The engineering of organized human corneal tissue through the spatial guidance of corneal stromal stem cells. Biomaterials. Elsevier Ltd; 2011 Nov. 10;:1–10.

95. Teixeira AI, Abrams GA, Bertics PJ, Murphy CJ, Nealey PF. Epithelial contact guidance on well-defined micro- and nanostructured substrates. Journal of cell science. 2003 May 15;116(Pt 10):1881–92.

96. Carlsson D, Li F, Shimmura S, Griffith M. Bioengineered corneas: how close are we? Current Opinion in Ophthalmology. 2003;14(4):192.

97. Flemming RG, Murphy CJ, Abrams GA, Goodman SL, Nealey PF. Effects of synthetic micro- and nano-structured surfaces on cell behavior. Biomaterials. 1999 Mar.;20(6):573–88.

98. Gil E, Park S, Marchant J, Omenetto F, Kaplan D. Response of human corneal fibroblasts on silk film surface patterns. Macromolecular Bioscience. 2010;10(6):664–73.

99. Madduri S, Papaloīzos M, Gander B. Trophically and topographically functionalized silk fibroin nerve conduits for guided peripheral nerve regeneration. Biomaterials. 2010 Mar.;31(8):2323–34.

100. Perry H, Gopinath A, Kaplan D, Dal Negro L, Omenetto F. Nano-and Micropatterning of Optically Transparent, Mechanically Robust, Biocompatible Silk Fibroin Films. Advanced Materials. 2008;20(16):3070–2.

101. Tsioris K, Raja WK, Pritchard EM, Panilaitis B, Kaplan DL, Omenetto FG. Fabrication of Silk Microneedles for Controlled-Release Drug Delivery. Advanced Functional Materials. 2011 Dec. 2;22(2):330–5.

102. Zhang Q, Zhao Y, Yan S, Yang Y, Zhao H, Li M, et al. Preparation of uniaxial multichannel silk fibroin scaffolds for guiding primary neurons. Acta Biomaterialia. 2012 Mar. 28.

103. Smith H. A review of submicron lithography. Superlattices and Microstructures. 1986.

104. Whitesides G, Massachusetts Institute of Technology Microsystems Technology Laboratories. Soft lithography. Annu. Rev. Mater. Sci. 1998.

105. Panilaitis B, Altman G, Chen J, Jin H, Karageorgiou V, Kaplan D. Macrophage responses to silk. Biomaterials. 2003;24(18):3079–85.

106. Arai T, Freddi G, Innocenti R, Tsukada M. Biodegradation of Bombyx mori silk fibroin fibers and films. Journal of Applied Polymer Science. 2004;91(4):2383–90.

107. Hofmann S, Wong Po Foo C, Rossetti F, Textor M, Vunjak-Novakovic G, Kaplan D, et al. Silk fibroin as an organic polymer for controlled drug delivery. Journal of Controlled Release. 2006;111(1-2):219–27.

108. Bettinger C, Cyr K, Matsumoto A, Langer R, Borenstein J, Kaplan D. Silk fibroin microfluidic devices. Advanced Materials. 2007;19(19):2847–50.

109. Lovett M, Cannizzaro C, Daheron L, Messmer B, Vunjak-Novakovic G, Kaplan D. Silk fibroin microtubes for blood vessel engineering. Biomaterials. 2007;28(35):5271–9.

110. Minoura N, Tsukada M, Nagura M. Physico-chemical properties of silk fibroin membrane as a biomaterial. Biomaterials. 1990;11(6):430–4.

111. Minoura N, Tsukada M, Nagura M. Fine structure and oxygen permeability of silk fibroin membrane treated with methanol. Polymer. 1990;31(2):265–9.

112. Rice W, Firdous S, Gupta S, Hunter M, Foo C, Wang Y, et al. Non-invasive characterization of structure and morphology of silk fibroin biomaterials using non-linear microscopy. Biomaterials. 2008;29(13):2015–24.

113. Arrondo J, Muga A, Castresana J, Goni F. Quantitative studies of the structure of proteins in solution by Fourier-transform infrared spectroscopy. Progress in biophysics and molecular biology. 1993;59(1):23.

114. Dong A, Huang P, Caughey W. Protein secondary structures in water from second-derivative amide I infrared spectra. Biochemistry.

1990;29(13):3303–8.

115. Zoumi A, Yeh A, Tromberg B. Imaging cells and extracellular matrix in vivo by using second-harmonic generation and two-photon excited fluorescence. Proceedings of the National Academy of Sciences of the United States of America. 2002;99(17):11014.

116. Demura M, Asakura T. Immobilization of glucose oxidase with Bombyx mori silk fibroin by only stretching treatment and its application to glucose sensor. Biotechnology and bioengineering. 1989;33(5):598–603.

117. Cebe P, Kaplan D. Mechanism of enzymatic degradation of beta-sheet crystals. Biomaterials. 2010.

118. Li M, Ogiso M, Minoura N. Enzymatic degradation behavior of porous silk fibroin sheets. Biomaterials. 2003;24(2):357–65.

119. Ma X, Cao C, Zhu H. The biocompatibility of silk fibroin films containing sulfonated silk fibroin. Journal of Biomedical Materials Research Part B: Applied Biomaterials. 2006;78(1):89–96.

120. Patel A, Thakar R, Chown M, Ayala P. Biophysical mechanisms of single-cell interactions with microtopographical cues. Biomedical …. 2010.

121. Karuri N, Porri T, Albrecht R, Murphy C, Nealey P. Nano-and microscale holes modulate cell-substrate adhesion, cytoskeletal organization, and-beta1 integrin localization in SV40 human corneal epithelial cells. IEEE transactions on nanobioscience. 2006;5(4):273.

122. Liliensiek S, Campbell S, Nealey P, Murphy C. The scale of substratum topographic features modulates proliferation of corneal epithelial cells and corneal fibroblasts. Journal of Biomedical Materials Research Part A. 2006;79(1):185–92.

123. Teixeira A, McKie G, Foley J, Bertics P, Nealey P, Murphy C. The effect of environmental factors on the response of human corneal epithelial cells to nanoscale substrate topography. Biomaterials. 2006;27(21):3945–54.

124. Lawrence B, Wharram S, Kluge J, Leisk G, Omenetto F, Rosenblatt M, et al. Effect of Hydration on Silk Film Material Properties. Macromolecular Bioscience. 2010;10(4):393–403.

125. Zhang Y. Natural silk fibroin as a support for enzyme immobilization. Biotechnology Advances. 1998;16(5-6):961–71.

126. Cebe P, Kaplan D. Mechanism of enzymatic degradation of beta-sheet crystals. Biomaterials. 2010.

127. Shaw J. Fractionation of the fibroin of Bombyx mori with trypsin. Biochemical Journal. 1964;93(1):45.

128. Bray LJ, George KA, Ainscough SL, Hutmacher DW, Chirila TV, Harkin DG. Human corneal epithelial equivalents constructed on Bombyx mori silk fibroin membranes. Biomaterials. 2011 Aug. 1;32(22):5086–91.

129. Jaalouk DE, Lammerding J. Mechanotransduction gone awry. Nat Rev Mol Cell Biol. Nature Publishing Group; 2009 Jan.;10(1):63–73.

130. Tsai R, Li L. Reconstruction of Damaged Corneas by Transplantation of Autologous Limbal Epithelial Cells — NEJM. New England Journal of Medicine. 2000.

131. Grueterich M, Espana E, Tseng S. Ex vivo expansion of limbal epithelial stem cells: amniotic membrane serving as a stem cell niche* 1. SURVEY OF OPHTHALMOLOGY. 2003;48(6):631–46.

132. Liu J, Sheha H, Fu Y, Giegengack M. Oral Mucosal Graft With Amniotic Membrane Transplantation for Total Limbal Stem Cell Deficiency. American journal of …. 2011.

133. Hayashida Y. Ocular Surface Reconstruction Using Autologous Rabbit Oral Mucosal Epithelial Sheets Fabricated Ex Vivo on a Temperature-Responsive Culture Surface. INVESTIGATIVE OPHTHALMOLOGY & VISUAL SCIENCE. 2005 May 1;46(5):1632–9.

134. Nishida K, Yamato M, Hayashida Y, Watanabe K, Maeda N, Watanabe H, et al. Functional bioengineered corneal epithelial sheet grafts from corneal stem cells expanded ex vivo on a temperature-responsive cell culture surface. Transplantation KW . 2004;77(3):379.

135. Pang K, Du L, Wu X. A rabbit anterior cornea replacement derived from acellular porcine cornea matrix, epithelial cells and keratocytes. Biomaterials. 2010 Oct.;31(28):7257–65.

136. Fu Y, Fan X, Chen P, Shao C, Lu W. Reconstruction of a tissue-engineered cornea with porcine corneal acellular matrix as the scaffold. Cells Tissues Organs. Karger Publishers; 2010;191(3):193–

202.

137. Acharya C, Ghosh S. Silk fibroin protein from mulberry and non-mulberry silkworms: cytotoxicity, biocompatability and kinetics of L929 murine fibroblast adhesions. Journal of Materials Science: Materials …. 2008.

138. Nazarov R, Jin H-J, Kaplan DL. Porous 3-D Scaffolds from Regenerated Silk Fibroin. Biomacromolecules. 2004 May;5(3):718–26.

139. Sofia S, McCarthy M, Gronowicz G, Kaplan D. Functionalized silk-based biomaterials for bone formation. Journal of biomedical materials research. 2001;54(1):139–48.

140. Hopkinson A, Shanmuganathan VA, Gray T, Yeung AM, Lowe J, James DK, et al. Optimization of Amniotic Membrane (AM) Denuding for Tissue Engineering. Tissue Engineering Part C: Methods. 2008 Dec.;14(4):371–81.

141. Jingbo Liu HSYFLLSCT. Update on amniotic membrane transplantation. Expert Review of Ophthalmology. NIH Public Access; 2010 Oct. 1;5(5):645–61.

142. Oyen M, Cook R. Mechanical failure of human fetal membrane tissues. Journal of Materials Science: Materials in …. 2004.

143. Spoerl E, Wollensak G, Reber F. Cross-Linking of Human Amniotic Membrane by Glutaraldehyde. Ophthalmic …. 2004.

144. Ma DH-K, Wang S-F, Su W-Y, Tsai RJ-F. Amniotic Membrane Graft for the Management of Scleral Melting and Corneal Perforation in Recalcitrant Infectious Scleral and Corneoscleral Ulcers. Cornea. 2002 Apr. 1;21(3):275.

145. Karageorgiou V, Meinel L. Bone morphogenetic protein-2 decorated silk fibroin films induce osteogenic differentiation of human bone marrow stromal cells - Karageorgiou - 2004 - Journal of Biomedical Materials Research Part A - Wiley Online Library. … Research Part A. 2004.

146. Meinel L, Fajardo R, Hofmann S, Langer R, Chen J, Snyder B, et al. Silk implants for the healing of critical size bone defects. Bone. 2005;37(5):688–98.

147. Talukdar S, Nguyen Q, Chen A, Sah R. Effect of initial cell seeding

density on 3D-engineered silk fibroin scaffolds for articular cartilage tissue engineering. Biomaterials. 2011.

148. Sahoo S, Lok Toh S, Hong Goh JC. PLGA nanofiber-coated silk microfibrous scaffold for connective tissue engineering. Journal of Biomedical Materials Research Part B: Applied Biomaterials. Wiley Online Library; 2010;95(1):19–28.

149. Koizumi N, Inatomi T, Sotozono C, Fullwood NJ, Quantock AJ, Kinoshita S. Growth factor mRNA and protein in preserved human amniotic membrane. Informa UK Ltd UK; 2000.

150. Fukuda K, Chikama T, Nakamura M, Nishida T. Differntial distribution of subchains of the basement membrane components type IV collagen and laminin among the amniotic membrane, cornea, and conjunctiva. Cornea. 1999 Jan.;18(1):67–72.

151. Pellegrini G, Dellambra E. p63 identifies keratinocyte stem cells. 2001.

152. Schermer A, Galvin S. Differentiation-related expression of a major 64K corneal keratin in vivo and in culture suggests limbal location of corneal epithelial stem cells. The Journal of cell biology. 1986.

153. Chen B, Mi S, Wright B, Connon CJ. Differentiation status of limbal epithelial cells cultured on intact and denuded amniotic membrane before and after air-lifting. Tissue Engineering Part A. Mary Ann Liebert, Inc. 140 Huguenot Street, 3rd Floor New Rochelle, NY 10801 USA; 2010;16(9):2721–9.

154. Sudha B, Sitalakshmi G, Iyer GK, Krishnakumar S. Putative stem cell markers in limbal epithelial cells cultured on intact & denuded human amniotic membrane. Indian Journal of Medical Research. 2010;128(2):149.

155. Higa K, Takeshima N, Moro F. Porous Silk Fibroin Film as a Transparent Carrier for Cultivated Corneal Epithelial Sheets. Journal of …. 2010.

156. Sandoval H, de Castro L, Vroman D, Solomon K. Refractive surgery survey 2004. Journal of Cataract & Refractive Surgery. 2005;31(1):221–33.

157. Taneri S, Zieske J, Azar D. DIAGNOSTIC AND SURGICAL TECHNIQUES. SURVEY OF OPHTHALMOLOGY. 2004;49(6).

158. Gomes J, Romano A, Santos M, Dua H. Amniotic membrane use in ophthalmology. Current Opinion in Ophthalmology. 2005;16(4):233.

159. Limb G, Daniels J, Cambrey A, Secker G, Shortt A, Lawrence J, et al. Current prospects for adult stem cell-based therapies in ocular repair and regeneration. Current Eye Research. 2006;31(5):381–90.

160. Grueterich M, Espana E. ScienceDirect.com - Survey of Ophthalmology - Ex vivo expansion of limbal epithelial stem cells: amniotic membrane serving as a stem cell niche. SURVEY OF OPHTHALMOLOGY. 2003.

161. Chen X, Li W, Yu T. Conformation transition of silk fibroin induced by blending chitosan. Journal of Polymer Science Part B: Polymer Physics. 1997;35(14):2293–6.

162. Kluge J, Rabotyagova O, Leisk G, Kaplan D. Spider silks and their applications. Trends in biotechnology. 2008;26(5):244–51.

163. Karuri N, Nealey P, Murphy C, Albrecht R. Structural organization of the cytoskeleton in SV40 human corneal epithelial cells cultured on nano-and microscale grooves. Scanning. 2008;30(5):405–13.

164. Gipson I, Spurr-Michaud S, Argueso P, Tisdale A, Ng T, Russo C. Mucin gene expression in immortalized human corneal-limbal and conjunctival epithelial cell lines. INVESTIGATIVE OPHTHALMOLOGY & VISUAL SCIENCE. 2003;44(6):2496.

165. Evans M, McFarland G, Taylor S, Walboomers X. The response of healing corneal epithelium to grooved polymer surfaces. Biomaterials. 2005;26(14):1703–11.

166. Araujo J, Téran F, Oliveira R, Nour E, Montenegro M, Campos J, et al. Comparison of hexamethyldisilazane and critical point drying treatments for SEM analysis of anaerobic biofilms and granular sludge. Journal of electron microscopy. 2003;52(4):429.

167. XIA Y, Whitesides G. ChemInform Abstract: Soft Lithography. ChemInform. 1998;29(25).

168. Pease R. Imprints offer Moore. Nature. 2002;417(6891):802–3.

169. Smith PK, Krohn R, Olson B, Hermanson G, Mallia A, Gartner F, et al. Measurement of protein using bicinchoninic acid. Analytical Biochemistry. 1985 Oct.;150(1):76–85.

170. Noordmans HJ, Smeulders AWM, van der Voort HTM. Fast volume render techniques for interactive analysis. The Visual Computer. 1997 Nov. 18;13(8):345–58.

171. Dunn G, Heath J. A new hypothesis of contact guidance in tissue cells* 1. Experimental Cell Research. 1976;101(1):1–14.

172. Wilson SE, Netto M, Ambrósio R Jr. Corneal cells: chatty in development, homeostasis,wound healing, and disease. American journal of ophthalmology. 2003 Sep.;136(3):530–6.

173. Tocce EJ, Smirnov VK, Kibalov DS, Liliensiek SJ, Murphy CJ, Nealey PF. The ability of corneal epithelial cells to recognize high aspect ratio nanostructures. Biomaterials. 2010 May;31(14):4064–72.

174. Ingber D. Tensegrity II. How structural networks influence cellular information processing networks. Journal of cell science. 2003;116(8):1397–408.

175. Ziegler W, Liddington R. The structure and regulation of vinculin. Trends in cell biology. 2006.

176. Gov N. Collective cell migration patterns: Follow the leader. Proceedings of the National Academy of Sciences. 2007;104(41):15970.

177. Nakaya Y, Sukowati EW, Wu Y, Sheng G. RhoA and microtubule dynamics control cell–basement membrane interaction in EMT during gastrulation. Nat Cell Biol. 2008 Jun. 15;10(7):765–75.

178. Teixeira A, Nealey P, Murphy C. Responses of human keratocytes to micro-and nanostructured substrates. Journal of Biomedical Materials Research Part A. 2004;71(3):369–76.

179. Curtis A, Wilkinson C. Topographical control of cells. Biomaterials. 1997 Dec.;18(24):1573–83.

180. Crabb R, Chau E, Evans M, Barocas V, Hubel A. Biomechanical and microstructural characteristics of a collagen film-based corneal stroma equivalent. Tissue Engineering. 2006;12(6):1565–75.

181. Dupps W Jr, Wilson S. Biomechanics and wound healing in the cornea. Experimental eye research. 2006;83(4):709–20.

182. Trepat X, Wasserman M, Angelini T, Millet E, Weitz D, Butler J, et al.

Physical forces during collective cell migration. Nature Physics. 2009;5(6):426–30.

183. Hytönen V. How force might activate talin's vinculin binding sites: SMD reveals a structural mechanism. PLoS Computational Biology. 2008.

184. Lehnert D, Wehrle-Haller B, David C. Cell behaviour on micropatterned substrata: limits of extracellular matrix geometry for spreading and adhesion. Journal of cell …. 2004.

185. Etienne-Manneville S, Hall A. Rho GTPases in cell biology. Nature. 2002.

186. Lu Q, Kaplan D, Cebe P. Microphase separation controlled β-sheet crystallization kinetics in fibrous proteins. Macromolecules. 2009.

187. Koizumi N, Fullwood N, Bairaktaris G, Inatomi T, Kinoshita S, Quantock A. Cultivation of corneal epithelial cells on intact and denuded human amniotic membrane. INVESTIGATIVE OPHTHALMOLOGY & VISUAL SCIENCE. 2000;41(9):2506.